ABSTRACT

Title of Dissertation:	DEVELOPMENT OF A GLOBAL LONG TERM SURFACE ALBEDO DATA RECORD FROM NOAA AVHRR FOR THE ESTIMATION OF 38 YEAR TRENDS (1982-2020)
	Jose Luis Villaescusa Nadal, Doctor of Philosophy 2020
Dissertation directed by:	Dr. Christopher Justice, Co-Chair and Professor, and Dr. Belen Franch, Co-chair and Adjunct Associate Professor. Department of Geographical Sciences.

Long-term consistent data records and their analyses are crucial in the prediction of global climate and the associated environmental changes happening around the globe. In particular, surface albedo is of critical importance, since it is a key forcing parameter controlling the Earth's radiative energy budget and the energy exchange between surface and atmosphere. Given its significance, the Global Climate Observing System (GCOS) set a list of requirements that would aid the scientific community in climate model predictions of climate change.

The requirements for a dataset length of 30+ years and a daily temporal resolution can only be satisfied using data from the Advanced Very High Resolution Radiometer

(AVHRR) aboard the North Oceanic and Atmospheric Administration (NOAA) satellites. The goal of this dissertation is to create a long-term surface albedo dataset from the Long Term Data Record (LTDR) product, spanning from 1982-2018, that can provide surface albedo estimates at 0.05^0 spatial resolution and a daily temporal resolution.

To do this, the original LTDR product goes through several pre-processing steps to tackle some of its weaknesses and limitations. First, the data from the different AVHRR sensors aboard all NOAA satellites that comprise the dataset are harmonized, using a novel spectral adjustment method. Second, an algorithm is derived, to discriminate cloud and snow surfaces, which were previously only reported as the same class. Third, the clear land surface albedo was retrieved by improving upon a model optimized for the MODerate resolution Imaging Spectrometer (MODIS). The snow albedo, on the other hand, was obtained through a random forest approach, using MODIS-derived albedo as a reference.

These steps allowed the computation of the Satellite AVHRR Land Surface Albedo (SALSA) product, which was cross-compared with the well-validated MCD43C3 product, based on MODIS data. This comparison revealed the main strengths and limitations of the product, but an overall acceptable behavior, with uncertainties below 0.03 in average.

The product was then used to estimate long-term surface albedo trends. The results revealed that the overall surface albedo has not significantly changed through the period 1982-2018, highlighting the importance of computing long-term trends using 30+ years of observations.

DEVELOPMENT OF A GLOBAL LONG TERM SURFACE ALBEDO DATA RECORD FROM NOAA AVHRR FOR THE ESTIMATION OF 38 YEAR TRENDS (1982-2020)

by

Jose Luis Villaescusa Nadal

Dissertation submitted to the Faculty of the Graduate School of the
University of Maryland, College Park, in partial fulfillment
of the requirements for the degree of
Doctor of Philosophy
2020

Advisory Committee:

Professor Christopher Justice, Chair
Professor Belén Franch, Co-Chair
Professor Jean-Claude Roger
Professor Eric Vermote
Professor Sergii Skakun

Acknowledgements

First, I want to thank my Co-Advisor Dr. Belén Franch. Thank you for taking me in and providing me with this timeless opportunity to work surrounded by the best researchers in our field. Thank you for believing in me, and having the patience to guide me through this journey of professional and personal growth. Your insights and perspective eased my path towards obtaining this PhD.

I also want to thank Dr. Eric Vermote, Dr. Jean-Claude Roger and Dr. Sergii Skakun, for providing effective guidance and support on my PhD research. You were always available, approachable and patient when I was going out of track. You always provided me with useful feedback to orientate not only my research, but also my professional goals and direction. I am grateful to my advisor Dr. Chris Justice, for constantly providing focus on the broader perspective, and for giving me that extra push which I many times needed.

My special thanks go to Andrés Santamaría. Thank you for always being there, both personally and professionally. Your kindness and humbleness constantly inspired me. Thank you for answering all the programming questions that I asked much more often than I am willing to admit. I will never forget the good times during conferences and our adventures in NASA Goddard.

To the friends I have made along the way that have made this journey worth traveling. To Daniel, Stefano, Anisha, Dina, Maytal, Jaime, Ioanna and many others, thank you for the good times and camaraderie.

Last but not least, to my family. To my mom, Pilar, my dad José Vicente and my sister Verónica. Thank you for always nurturing my passions and encouraging me to aim for the stars. Without your support and optimism, none of this work would have been possible.

Table of Contents

List of Tables

List of Figures

List of Abbreviations

AOT	Aerosol Optical Thickness
APU	Accuracy, Precision and Uncertainty
AVHRR	Advanced Very High Resolution Radiometer
AVIRIS	Airborne Visible and Infrared Imaging Spectrometer
BRDF	Bidirectional Reflectance Distribution Function
BSA	Black-sky albedo
CDR	Climate Data Record
CEOS	Committee on Earth Observation Satellites
ECV	Essential Climate Variable
ENSO	El Niño Southern Oscillation
GCM	General Circulation Model
GCM	Global Climate Model
GCOS	Global Climate Observing System
GEWEX	Global Energy and Water Exchanges Project
ISCCP	International Satellite Cloud Climatology Project
MAE	Mean Absolute Error
MBE	Mean Bias Error
MCD	Modis Terra+Aqua Combined product
MERRA-2	The Modern-Era Retrospective analysis for Research and Applications, Version 2
MODIS	Moderate Resolution Imaging Spectrometer
MODTRAN	MODerate resolution atmospheric TRANsmission code (MODTRAN)
NDVI	Normalized Difference Vegetation Index
NOAA	National Oceanic and Atmospheric Administration
POES	Polar Orbiting Environmental Satellites
POLDER	Polarization and Directionality of the Earth's Reflectances
RMSE	Root Mean Square Error
RSR	Relative Spectral Response
RTLSR	Ross Thick Lee-Sparse Reciprocal
SBAF	Spectral Band Adjustment Factor
SZA	Solar Zenith Angle
USGS	U.S. Geological Survey
VZA	View Zenith Angle
WSA	White-sky albedo

Chapter 1: Introduction

1.1. Background and motivation

The Earth is reaching the hottest temperatures ever recorded in our modern history, the effects of climate change are devastating communities in the form of hurricanes, drought, sea level rise or forest fires, and the impact on the planet and the millions of species living in it will persist for centuries to millennia, and will continue to cause further long-term changes in the climate system (Masson-Delmotte *et al.*, 2019). Faced with this doomsday scenario, we must make use of every tool at our disposal for improved detection, attribution and prediction of global climate and the associated environmental changes happening all around the globe. Such information could aid policymakers and government officials in mitigating the effects of climate change and protect the communities at risk in a timely manner. Long-term consistent data records and their analyses are crucial in this context (Schulz *et al.*, 2008; Hollmann *et al.*, 2013; Bates *et al.*, 2015), as they allow us to understand the possible effects that climate change will have at global, regional or local scales. Thanks to recent developments in Earth observation satellites and improvements in satellite data analysis, we are able to obtain consistent information in a timely fashion about some of these effects around the world (Flasse and Ceccato, 1996; Hollmann *et al.*, 2013).

In particular, the knowledge of surface albedo is of critical importance. Surface albedo is a property of the land and the overlying atmosphere that quantifies the fraction of sunlight reflected by the Earth's surface (Dickinson, 1983; Liang, Li and Wang, 2012). It is a key forcing parameter in the monitoring of land surface processes, controlling the Earth's radiative energy budget and the energy exchange between surface and

atmosphere. Therefore, it plays an important role in considerations within climate and weather prediction models. It varies spatiotemporally due to natural processes such as forest fires, snowfall, ice melt, vegetation growth and illumination conditions, and due to human processes such as deforestation, crop harvesting, crop burning or urbanization, making it a sensitive indicator of environmental vulnerability (CEOS, 2019).

Given its significance, the Global Climate Observing System (GCOS), listed this parameter as an Essential Climate Variable (ECV) (Hollmann *et al.*, 2013; Bojinski *et al.*, 2014), or in other words, as a variable that "critically contributes to the characterization of the Earth's climate" (*Essential Climate Variables*, 2017). As a result, a global long term Climate Data Record (CDR) of land surface albedo is required by climate, biogeochemical, hydrological, and weather forecast models at a range of spatial (from a few meters to 30 km) and temporal (from daily to monthly) scales (CEOS, 2019). The quality of this CDR is quite important, since the variance of the climatic predictions provided by different climate models around the world depends in great measure on the quality and consistency of the data used. For this reason, the GCOS set a list of requirements for different atmospheric and biophysical parameters typically used in climate variable datasets (GCOS-200, 2016). The following section explains in detail the reasoning behind the requirements for surface albedo.

1.2. Rationale for requirements and current products

Table 1 shows the GCOS requirements for surface albedo measurements using satellite data for different sets of characteristics. Firstly, the rationale behind the spatial and temporal resolution requirements have to do with the dataset's capacity to detect

changes in ice and snow melt, as well as changes over vegetation cover. Studies show, for example, that a time step of more than one day is perhaps too large to detect trends in the growing season's length during a decade, which range in some places between 2-3 days (Lebourgeois *et al.*, 2010; Planque, Carrer and Roujean, 2017). A higher frequency of observations would also be useful to guarantee the accuracy and stability of products used as inputs to General Circulation Models (GCMs), and to support a host of other downstream monitoring applications (CEOS, 2019).

Table 1: GCOS requirements of surface albedo (dimensionless) satellite observations

Spatial Resolution	200/500m
Temporal Resolution	Daily
Accuracy	Maximum of (5%; 0.0025)
Stability	Maximum of (1%; 0.001)
Length of Record	At least 30 years

Secondly, the accuracy is defined as the difference between a short-term average measured value of a variable and its true value, while the stability indicates to what extent this accuracy remains constant with time. While the accuracy value is important for understanding climate processes and changes, it is not a vital indicator regarding the estimation of long-term trends, as long as the stability of the dataset is high. In other words, if the accuracy is lower than a certain required threshold, but this value is consistent throughout the whole time series, the trend value would be the same in the dataset as it would be for the true value. The basis for choosing this stability threshold for surface albedo has to do with the uncertainty in climate model predictions of climate change. This value represents the stability that a surface albedo CDR should have in

order to narrow down possible simulations of climate change to a range of ±20% stability (Ohring and Wielicki, 2005).

Finally, the temporal span of these CDRs is also of crucial importance, since short time series of satellite data might hinder the ability of separating long-term trends from inter-annual and decadal variability in a reliable way (Trenberth *et al.*, 2006; Yang *et al.*, 2013a). Moreover, there is a strong emphasis in the literature on the importance of recovering and improving historical satellite data, dating back to the 1980s, for it is particularly valuable to improve surface forcing in climate models. The GCOS suggested a length of record of 30+ years for satellite observation of the climate system (GCOS-200, 2016).

Current surface albedo products available in the literature are encouraging but need improvement with regard to product accuracy, temporal resolution, or data consistency (Qu *et al.*, 2015). A list of common surface albedo products used in the literature is shown in Table 2. These products cover a wide range of satellite instruments and use very different retrieval algorithms. They have spatial resolutions ranging from 500 m to 55 km and temporal resolutions ranging from daily to yearly. However, albedo products with a temporal coverage of 30+ years of observations are not common, since only the Advanced Very High Resolution Radiometer (AVHRR), and Landsat sensors are able to provide (almost) continuous observations since the 1980s until the present. Any surface albedo dataset covering less than 30 years is still relatively short for climate change research purposes (Trenberth *et al.*, 2006; Yang *et al.*, 2013b). Among these, three products stand out that use AVHRR observations in combination with the Moderate Resolution Imaging Spectroradiometer (MODIS) or the Satellite Pour

l'Observation de la Terre (SPOT): the Quality Assurance for Essential Climate Variables (QA4ECV), the Global Land-Surface Satellite (GLASS), and the Copernicus Climate Change Service (C3S Albedo) products. These products, however, do not succeed in satisfying the daily temporal resolution GCOS requirement, for they use albedo computation algorithms that require at least 8 days of data. Nonetheless, the AVHRR satellite's characteristics provide a unique opportunity to create a daily surface albedo product dating back to 1982 that satisfies the GCOS requirements for temporal resolution and length of record. The product that this dissertation aims to create is shown at the bottom of Table 2, and is called the Satellite AVHRR Land Surface Albedo (SALSA) product.

Table 2: List of commonly used surface albedo products available in the literature sorted by increasing length of coverage. The symbol * means that a daily temporal filter is used in the product. The Satellite AVHRR Land Surface Albedo (SALSA) product is the prospective outcome of the studies performed in this dissertation.

Name	Platform / Sensor	Spatial Res.	Temporal Res.	Temporal Span	Length (years)	Spatial Coverage	Web
ETAL	EUMETSAT	1km	10 days	2015-now	5	Global	Link
Copernicus Albedo	PROBA-V	1km	10 days	2014-now	6	Global	Link
SURFALB	VIIRS	1km	9 days*	2011-now	9	Global	Link
VNP43	VIIRS	500m/30arcsec/ 0.05°	daily	2011-now	9	Global	Link
POLDER	ADEOS 1-3	6km	10 days	1996-2006	10	Global	Link
Globalbedo	Terra/Aqua/SPOT/ENVISAT	1km/0.05°	16 days	1998-2011	13	Global	Link
VEGETATION	SPOT	1km	10 days	1999-2014	15	Global	Link
CERES	TERRA/AQUA	20km/1°	Instantaneous/3hr/monthly	2000-2016	16	Global	Link
MCD43	Terra/Aqua	1km/0.05°	8 days	2000-now	18	Global	Link
MISR	Terra	0.275-1km	daily/monthly /yearly	2000-now	18	Global	Link
Meteosat	GOES/GMS	3km (nadir)	10 days	1981-2007	26	Euro, Africa, M. East, Asia	Link
CLARA	NOAA	25km	5 days/monthly	1982-2009	27	Global	Link
QA4ECV	NOAA/GEO/MODIS	0.05°/0.5°	8-day*	1982-2016	34	Global	Link
GLASS	Terra/Aqua/NOAA	1km/0.05°	8 days	1981-2017	36	Global	Link
C3S Albedo	NOAA/SPOT	1km/4km	10 days	1981-now	39	Global	Link
SALSA	NOAA	0.05°	daily	1982-now	38	Global	

1.3. AVHRR, MODIS and the LTDR product

The AVHRR is an instrument that has been aboard the National Oceanic and Atmospheric Administration (NOAA) family of polar orbiting platforms (POES) and European MetOP satellites for decades (Table 3). AVHRR data have been collected almost continuously since 1981, providing global daily measurements of the Earth's surface both in the optical and thermal spectra at ~1.1 km spatial resolution. It has since been used extensively for a wide range of applications, including fire detection, vegetation monitoring, crop yield estimation, and sea surface temperature analysis among others (McClain, Pichel and Walton, 1985; Gutman, 1991; Flasse and Ceccato, 1996; Unganai and Kogan, 1998).

Table 3: List of satellites that the AVHRR instrument has been aboard since its inception, along with the launch date and start-end dates.

Satellite name	AVHRR sensor	Launch date	Service start	Service end
TIROS-N	AVHRR/1	10/1978	10/1978	01/1980
NOAA-6	AVHRR/1	06/1979	06/1979	11/1986
NOAA-7	AVHRR/2	06/1981	08/1981	06/1986
NOAA-8	AVHRR/2	03/1983	05/1983	10/1985
NOAA-9	AVHRR/2	12/1984	02/1985	05/1994
NOAA-10	AVHRR/2	09/1986	11/1986	09/1991
NOAA-11	AVHRR/2	09/1988	11/1988	09/1994
NOAA-12	AVHRR/2	05/1991	05/1991	12/1994
NOAA-14	AVHRR/2	12/1994	12/1994	05/2007
NOAA-15	AVHRR/3	05/1998	05/1998	Present
NOAA-16	AVHRR/3	09/2000	09/2000	06/2014
NOAA-17	AVHRR/3	06/2002	06/2002	04/2013
NOAA-18	AVHRR/3	05/2005	08/2005	present
NOAA-19	AVHRR/3	02/2009	06/2009	present
Metop-A	AVHRR/3	10/2006	06/2007	present
Metop-B	AVHRR/3	09/2012	04/2013	present
Metop-C	AVHRR/3	11/2018	07/2019	present

The AVHRR sensor has three different versions that have been improved upon over the years. The design of the sensor bands present in all three versions is kept more or less stable, to ensure the continuity of the time series, and to ease the development of

long-term studies thanks to higher stability of the data. Over time, however, improvements in remote sensing algorithms and in the understanding of impacts of the Sun-Earth system have led to optimal band designs, which include a higher number of bands and a narrower window, even in combination of a panchromatic wide band. These retrieve the necessary information to perform atmospheric correction of the optical bands more accurately, or to correctly discriminate cloud and snow pixels and cirrus clouds. For this reason, maintaining a legacy design of the spectral bands poses some limitations on the sensor's potential to describe the Sun-Earth system with high accuracy. The first AVHRR version (AVHRR/1) observed the Earth's surface with a swath width of approximately 2500 km using four wide channels: two in the optical spectrum, and two in the thermal spectrum. The second version (AVHRR/2), for the first time aboard NOAA7, added a fifth channel in the thermal band. The latest version (AVHRR/3), starting from NOAA15 onwards added a sixth channel to better detect snow pixels. The spectral details and typical use of each band are shown in Table 4. The AVHRR sensor version aboard each satellite is shown in Table 3.

Table 4: Spectral resolution of the AVHRR/3 sensor and typical use of each band.

Channel Number	Resolution at Nadir	Wavelength (um)	Typical Use
1	1.09 km	0.58 - 0.68	Daytime cloud detection, surface mapping
2	1.09 km	0.725 - 1.00	Surface mapping, Land-water boundaries
3A	1.09 km	1.58 - 1.64	Snow and ice detection (Not present for AVHRR/2)
3B	1.09 km	3.55 - 3.93	Fire detection, night cloud mapping, sea surface temperature (Not present for AVHRR/1)
4	1.09 km	10.30 - 11.30	Night cloud mapping, sea surface temperature
5	1.09 km	11.50 - 12.50	Sea surface temperature

Many of the AVHRR sensor's limitations were successfully improved upon by the use of the MODIS sensor. Similar to AVHRR, the MODIS sensor has been acquiring global images on a daily basis at 250 m-1 km spatial resolution since its launch aboard NASA Terra in the year 2000. It was further included in the twin mission NASA Aqua, which has only a slight overpass difference with the AVHRR pm satellites. This sensor, as shown in Table 5, has a much larger number of bands distributed in both the optical and thermal spectrum, and a shorter bandwidth. This means that parameters, which are challenging to calculate using AVHRR data such as AOT or water vapor, can be completed using MODIS measurements with little uncertainty.

Given the importance of maintaining long-term satellite data records for the scientific community and improvement of climatic models, there have been several attempts in the literature to develop a consistent data record from AVHRR data. One of these attempts, currently funded by NASA, is the Long Term Data Record (LTDR) product (Vermote and Claverie, 2013; Franch *et al.*, 2016a). This product aims to develop a quality and consistent CDR of AVHRR data with the use of the Moderate Resolution Imaging Spectrometer (MODIS) instrument as a reference. This data record creates daily surface reflectance products at coarse spatial resolution (0.05°/5.5km), which makes it ideal for studying the long-term evolution of surface albedo in a global scale. The utility of this long time series has been demonstrated in the literature for a large number of applications such as agriculture (Franch *et al.*, 2016a), burned area mapping (Moreno Ruiz *et al.*, 2012), Leaf Area Index (LAI) and Fraction of Absorbed Photosynthetically Active Radiation (FAPAR) retrieval (Verger *et al.*, 2012; Claverie *et al.*, 2016), snow cover estimation (Wang *et al.*, 2017), global vegetation monitoring

(Julien and Sobrino, 2011), and surface albedo estimation products (Saunders, 1990; Hu *et al.*, 2000; Strugnell, Lucht and Schaaf, 2001; Trishchenko *et al.*, 2008a).

Table 5: Spectral Resolution of the MODIS sensor, and typical use of each band.

Band	Wavelength (nm)	Resolution (m)	Primary use
1	620–670	250	Land/cloud/aerosols boundaries
2	841–876	250	
3	459–479	500	Land/cloud/aerosols properties
4	545–565	500	
5	1230–1250	500	
6	1628–1652	500	
7	2105–2155	500	
8	405–420	1000	Ocean color/ phytoplankton/ biogeochemistry
9	438–448	1000	
10	483–493	1000	
11	526–536	1000	
12	546–556	1000	
13	662–672	1000	
14	673–683	1000	
15	743–753	1000	
16	862–877	1000	
17	890–920	1000	Atmospheric water vapor
18	931–941	1000	
19	915–965	1000	
20	3.660–3.840	1000	Surface/cloud temperature
21	3.929–3.989	1000	
22	3.929–3.989	1000	
23	4.020–4.080	1000	
24	4.433–4.498	1000	Atmospheric temperature
25	4.482–4.549	1000	
26	1.360–1.390	1000	Cirrus clouds Water vapor
27	6.535–6.895	1000	
28	7.175–7.475	1000	
29	8.400–8.700	1000	
30	9.580–9.880	1000	Ozone
31	10.780–11.280	1000	Surface/cloud temperature
32	11.770–12.270	1000	
33	13.185–13.485	1000	Cloud top altitude
34	13.485–13.785	1000	
35	13.785–14.085	1000	
36	14.085–14.385	1000	

The LTDR product performs geolocation, calibration, and atmospheric and surface anisotropy correction for all AVHRR sensors aboard the NOAA afternoon (pm) satellites. The reason for using only afternoon satellites has to do with the high

uncertainty of the atmospheric correction algorithm when applied to low sun elevation pixels present in morning (am) satellites. Afternoon satellites include NOAA7, NOAA9, NOAA11, NOAA14, NOAA16, NOAA18 and NOAA19. The use of these satellites alone inevitably leads to small gaps in the data, for example during the last months of 1994, in exchange for a higher accuracy in the atmospheric correction. Figure 1Figure 1 shows the local overpass time of all NOAA satellites containing the AVHRR sensor.

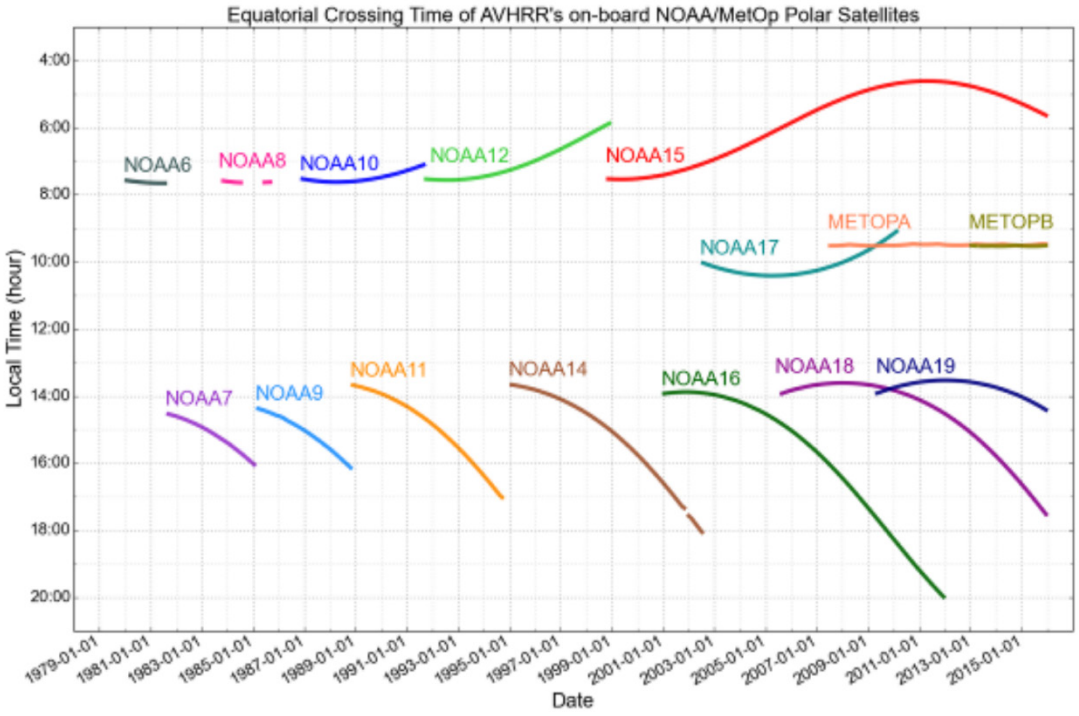

Figure 1: Local overpass time of all NOA satellites containing the AVHRR sensor. Figure obtained from (Clerbaux *et al.*, 2020).

The current LTDR product, however, has several issues that mitigate the retrieval of accurate surface albedo values. Firstly, there are errors regarding calibration. Analyzing the performance of the calibration algorithms is especially challenging for satellites before the arrival of MODIS Terra (2000), given the limited availability of comparable

measurements to ensure a consistent calibration approach throughout the time series. Secondly, there are issues regarding the atmospheric correction, which could be associated with the inability to accurately quantify the atmospheric water vapor concentration, and the lack of Aerosol Optical Thickness (AOT) determination for land pixels (Franch *et al.*, 2016a). Thirdly, the product currently has no spectral adjustment, so significant differences between the different satellites due only to the spectral design of the bands is expected, especially for pixels with large amounts of vegetation (Trishchenko, Cihlar and Li, 2002a; Villaescusa-Nadal, Franch, Roger, *et al.*, 2019). Fourthly, the surface anisotropic correction used is based on a model optimized for MODIS data, and little analysis has been done on the possible performance of this algorithm on AVHRR data (Vermote, Justice and Breon, 2009a). Finally, the cloud mask used in the current version is not able to distinguish between clouds and snow (snow cover is one of the most critical elements affecting the surface albedo change (Manabe and Wetherald, 1975; Lian and Cess, 1977)). The detection of snow using AVHRR data is challenging, especially considering the similar profile of clouds and snow on the limited bands available. A product capable of supporting climate models in retrieving high quality predictions of the Earth's energy balance through surface albedo measurements would require the product to be of the highest quality, granted the limitations inherent in the AVHRR's bands design.

1.4 Surface Albedo estimation from remote sensing data

1.4.1. Definition

Surface albedo (from the Latin word for white: albus) is a property of the land and the overlying atmosphere. It is defined as the ratio of upwelling flux of shortwave solar radiation to the downward flux, over the upward semi-hemispherical space (Dickinson, 1983), and therefore quantifies the 'whiteness' or fraction of sunlight reflected by the Earth's surface (dimensionless). Possible albedo values range from zero to one, though it is often expressed as a percentage (0-100%). In contrast to the surface reflectance that is defined for given angular conditions, the albedo integrates all angular conditions and thus describes an intrinsic property of the surface. In an ideal hypothetical case, all surfaces reflect in an isotropic manner, that is, they reflect equally on every direction, regardless of the illumination conditions. However, in reality, different surfaces reflect differently for different observation and incidence angles (Figure 2). In order to integrate all angular conditions, we must therefore have an approximation of the reflectance shape or Bidirectional Reflectance Distribution Function (BRDF) of each surface. The mathematical definition of the BRDF is as follows:

$$BRDF = f_r(\theta_i, \phi_i, \theta_r, \phi_r; \lambda) = \frac{dL_r(\theta_i, \phi_i, \theta_r, \phi_r; \lambda)}{dE_i(\theta_i, \phi_i, \theta_r, \phi_r; \lambda)} \quad (1)$$

Where the sub-indices i, r represent the incident (solar) and reflected (view) beams, and (θ, ϕ, λ) represent the zenith angle, azimuth angle and wavelength, respectively. The quantity $dE_i(\theta_i, \phi_i, \theta_r, \phi_r; \lambda)$ denotes the increment of the spectral radiance in an incoming beam per unit solid angle and unit area of the surface, while

$dL_r(\theta_i, \phi_i, \theta_r, \phi_r; \lambda)$ represents the corresponding reflected spectral radiance from the surface to the sensor viewing direction (Liang, Li and Wang, 2012). The BRDF has units of 1/sr.

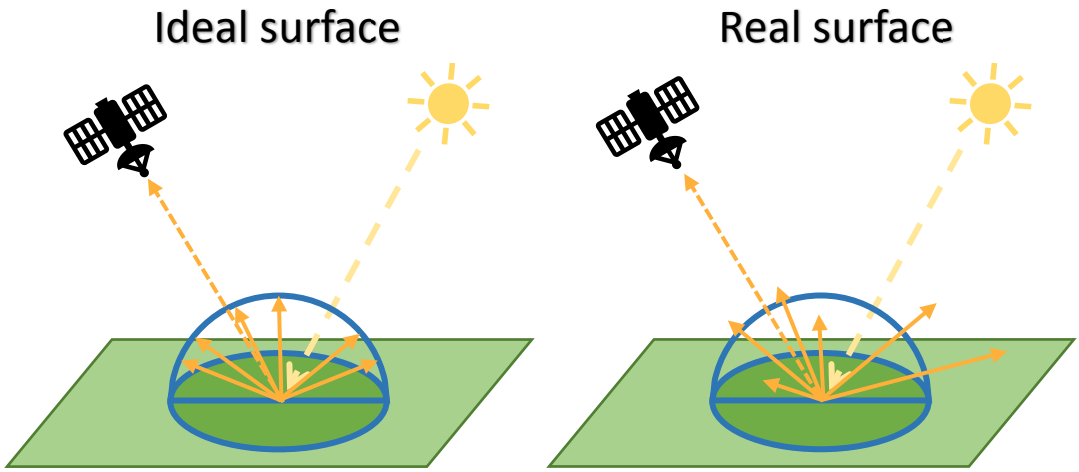

Figure 2: Graphic representation of the behavior of an ideal surface (left) vs a real surface (right) when illuminated by the sun.

Equivalent to the reflected beams, the incident light does not behave in an ideal nature. The downward radiation flux used in the surface albedo definition consists of two main components, the directional and diffuse radiation. When only an ideal directional radiation is considered, the term Black-Sky Albedo (BSA or directional-hemispherical reflectance) is employed. It is defined as the ratio of the radiant flux to the illumination radiant flux when the surface is illuminated with a parallel beam of light from a single direction:

$$\alpha_{BSA} = \frac{d\Phi_r(\theta_i, \phi_i; 2\pi)}{d\Phi_i(\theta_i, \phi_i)} = \int_0^{2\pi} \int_0^{\frac{\pi}{2}} f_r\,(\theta_i, \phi_i, \theta_r, \phi_r) sin\theta_r cos\theta_r d\theta_r d\phi_r \qquad (2)$$

When, in turn, an ideal diffuse radiation is used, the term White-Sky Albedo (WSA or bi-hemispherical reflectance) is employed (Schaaf *et al.*, 2002a). WSA is therefore defined as the radiant flux reflected from a unit surface area into the whole hemisphere to the isotropic incident radiant flux.

$$\alpha_{WSA} = \frac{d\Phi_r(2\pi; 2\pi)}{d\Phi_i(2\pi)} = \frac{1}{\pi}\int_0^{2\pi}\int_0^{\frac{\pi}{2}} \alpha_{BSA} * sin\theta_i cos\theta_i d\theta_i d\phi_i \quad (3)$$

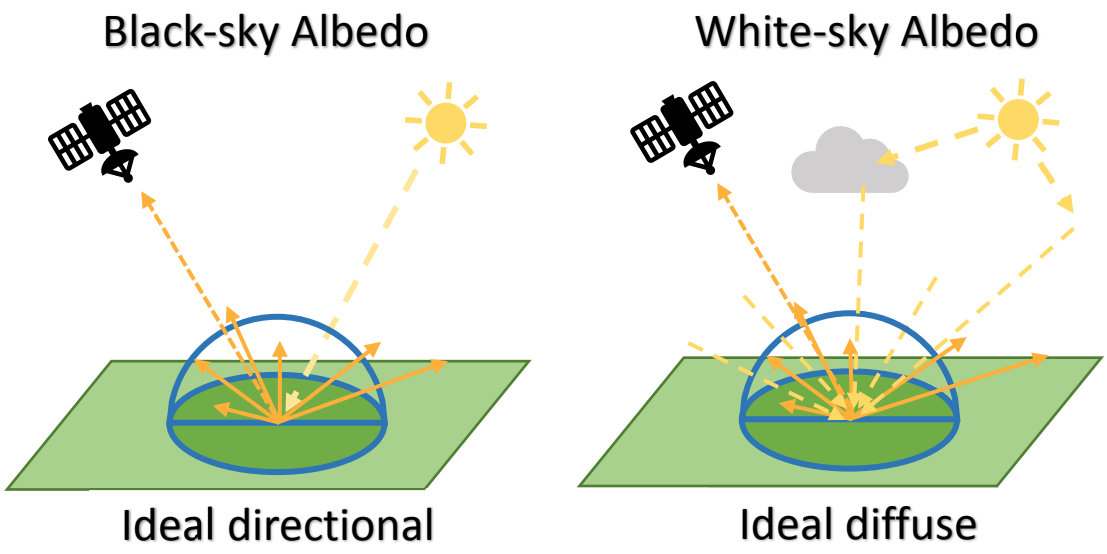

Figure 3: Graphic representation of the definitions of black-sky albedo (left) and white sky albedo (right).

The actual albedo, which is the value measured by ground instruments and used in climate models, is referred to as the blue-sky albedo or Hemispherical-Hemispherical Reflectance and it is estimated as the weighted average of both components using the diffuse skylight ratio (D):

$$\alpha_{blue} = (1 - D)\alpha_{BSA} + D\ \alpha_{WSA} \quad (4)$$

All previous expressions are definitions of spectral albedo (α_λ), that is, albedo defined for monochromatic rays of light only. However, surface albedo can be defined both for broad spectral regions (broadband albedo), or for spectral bands of finite width (narrowband albedo) (GCOS-200, 2016). The calculation of broadband albedo requires the integration of the spectral albedo over the corresponding wavelength range, weighted by the spectral radiant energy of the incident light, $F_d(\theta, \lambda)$ (Liang, Li and Wang, 2012):

$$\alpha_{bb} = \frac{\int_{\lambda_1}^{\lambda_2} \alpha_\lambda F_d(\theta, \lambda) d\lambda}{\int_{\lambda_1}^{\lambda_2} F_d(\theta, \lambda) d\lambda} \quad (5)$$

Narrowband albedos correspond therefore to specific spectral channels, and provide different information depending on the sensor used. Broadband albedos, on the other hand, since they are linked to a broad spectral region, are sensor independent and can be theoretically used to compare surface albedo values obtained from different sensors. The most commonly used broadband albedo in the literature is the shortwave albedo, which covers incoming solar radiation at bands from 0.3-3 μm, and is therefore a strong indicator of the surface's energy balance.

1.4.2. BRDF model

The determination of surface albedo requires an accurate description of the surface's BRDF shape, which in turn requires measurements of spectral radiance for evenly distributed illumination and observation angles. This measurement can be done in the laboratory or the field by means of a field goniometer (Figure 4), which allows one to

change the mounted spectroradiometer's observation angle freely, while taking measurements distributed along the day to capture different illumination conditions. However, when using measurements derived from satellite data, several complications arise. First, polar satellites often observe pixels at the same time every day, and would therefore have to use the evolution of the Sun's declination over the year to gather sufficient illumination angles samples. Second, the observation angles that a satellite can view a surface with are limited by the swath and orbit type. This means that only an incomplete picture of a certain surface's BRDF can be acquired.

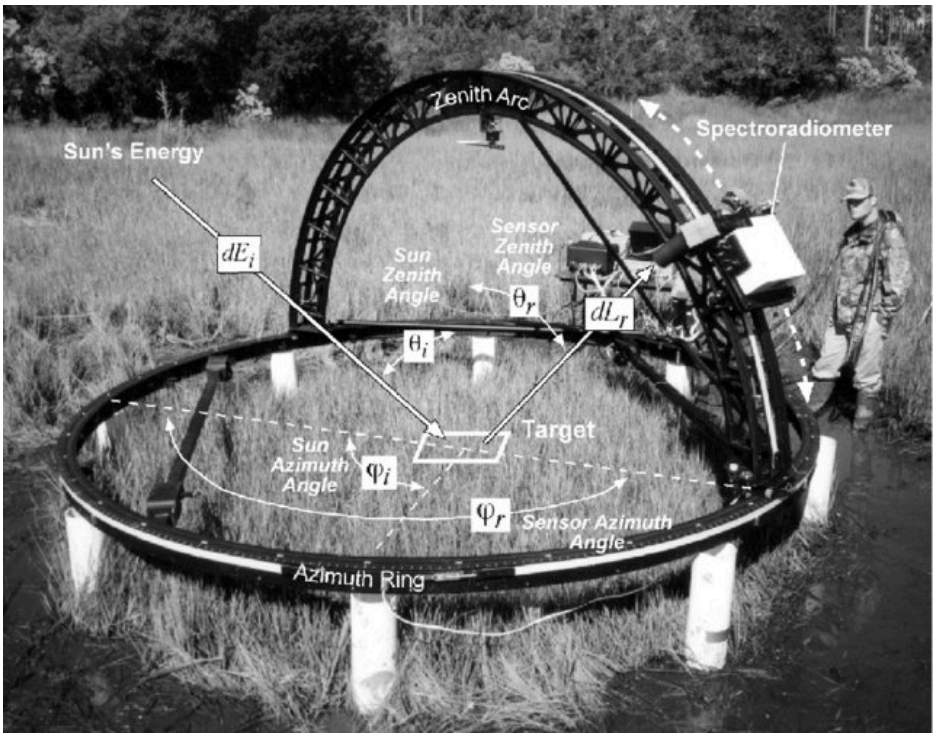

Figure 4: Picture of a working field goniometer used in (Schill *et al.*, 2004). The notation matches that from Equation 1.

Nonetheless, studies in the literature have shown specific and repetitive signatures of the BRDF shape on a biome basis (Hapke and Hoen, 1963; Deering and Eck, 1987). This was further demonstrated with the analysis of the Polarization and Directionality

of the Earth's Reflectances (POLDER) BRDF database measurements (Bacour and Bréon, 2005). This means that it is possible to obtain a good approximation of the BRDF shape given a small angular sampling of the surface. The most commonly used and successful model is the Ross Thick Li-Sparse Reciprocal (RTLSR) (Lucht, Schaaf and Strahler, 2000; Maignan, Bréon and Lacaze, 2004). This model expresses the bidirectional spectral reflectance $\rho(\theta_v, \theta_s, \phi, \lambda)$ as a combination of isotropic, geometric and volumetric components:

$$\rho(\theta_v, \theta_s, \phi, \lambda) = k_{iso}(\lambda) + k_{geo}(\lambda)F_{geo}(\theta_v, \theta_s, \phi) + k_{vol}(\lambda)F_{vol}(\theta_s, \theta_v, \phi) \quad (6)$$

In this Equation the sub-indices (s, v) represent the solar and view angles, ϕ is the relative azimuth angle $(\phi_v - \phi_s)$, $(k_{iso}, k_{vol}, k_{geo})$ are the weight coefficients of the isotropic, geometric and volumetric kernel functions, and (F_{geo}, F_{vol}) are the geometric and volumetric scattering components that provide the basic BRDF shapes for characterizing the heterogeneous scattering of the soil-vegetation system. They are expressed as:

$$F_{geo}(\theta_s, \theta_v, \phi) = \frac{m}{\pi}(t - \sin t - \cos t - \pi) + \frac{1 + \cos\xi}{2\cos\theta_s \cos\theta_v}$$

$$\cos t = \frac{2}{\sec\theta_s + \sec\theta_v}\sqrt{\Delta^2 + (\tan\theta_s \tan\theta_v \sin\phi)^2} \quad (7)$$

$$\Delta^2 = \tan^2\theta_s + \tan^2\theta_v - 2\tan\theta_s \tan\theta_v \cos\phi$$

$$m = \frac{1}{cos\theta_s} + \frac{1}{\cos\theta_v}$$

$$cos\xi = cos\theta_s * \cos\theta_v + sin\theta_s sin\theta_v cos\phi$$

$$F_{vol}(\theta_s, \theta_v, \phi) = \frac{4}{3\pi}\frac{1}{cos\theta_s + cos\theta_v}\left[\left(\frac{\pi}{2} - \xi\right)\cos\xi + sin\xi\right]\left(1 + \left(1 + \frac{\xi}{\xi_0}\right)^{-1}\right) - \frac{1}{3} \quad (8)$$

Figure 5 shows a visual representation of the physical interpretation of the isotropic, geometric and volumetric components. The isotropic component k_{iso} represents the bidirectional reflectance for $\theta_s = \theta_v = 0$, the geometric component considers the surface roughness and models the shape and position of the protrusions present in the surface, such as trees or buildings, while the volumetric component models the components inside said protrusions, made of randomly located scattering plane facets, such as leaves.

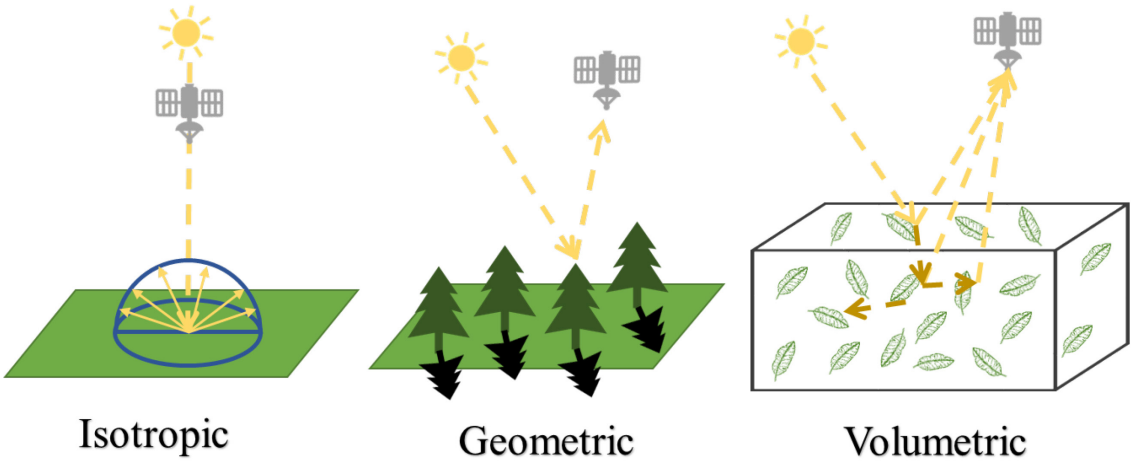

Figure 5: Visual representation of the physical interpretation of the isotropic, geometric and volumetric components that model the BRDF in the RTLSR model.

The estimation of the BRDF shape via Equation 6 thus relies on determining the values of the weight coefficients $k_{iso}, k_{vol}, k_{geo}$. This is typically done by finding the adequate values that minimize an objective function based on a given assumption. The most

common approach, used in the validated MODIS BRDF/Albedo product (Schaaf *et al.*, 2002a), is based on the assumption that over a certain composite period, in which the weight coefficients will be estimated, the variations due to directional effects are higher than the variations due to temporal effects. This leads to the following objective function:

$$\sum_{i=1}^{N}\left(k_{iso} + k_{vol}F_{vol}^{i} + k_{geo}F_{geo}^{i} - \rho_i\right)^2 \qquad (9)$$

The composite period is 16 days, since this is the orbit cycle of Aqua and Terra. The assumption used in this method, however, has certain limitations. First, it is violated for surfaces with fast changes in vegetation dynamics, such as crops, which will lead to uncertainties in the BRDF estimation. This means that it only holds true for a small composite period, before temporal changes become noteworthy. Second, if clouds or bad quality pixels are present, the composite period might be too short to retrieve the angular sampling necessary for an accurate estimation of the BRDF (typically 10-30 days).

For these reasons, (Vermote, Justice and Breon, 2009a) developed a method known as the VJB inversion. In order to estimate the weight coefficients, they use the assumption that the surface is subject to change significantly over the composite period, but the BRDF shape variations are limited. This can be expressed mathematically by first, rewriting Equation 6 as:

$$\rho(\theta_v, \theta_s, \phi, t) = k_{iso}(t)[1 + \boldsymbol{R}F_{geo}(\theta_v, \theta_s, \phi) + \boldsymbol{V}F_{vol}(\theta_v, \theta_s, \phi)] \qquad (10)$$

Where $V = k_{vol}/k_{iso}$ and $R = k_{geo}/k_{iso}$. Another way to express the assumption is to say that variations of $k_0(t)$ are small in successive observations. In other words, and manipulating Equation 10:

$$\frac{\rho(t_i)}{1 + \boldsymbol{V}F_{vol}^{i} + \boldsymbol{R}F_{geo}^{i}} \approx \frac{\rho(t_{i+1})}{1 + \boldsymbol{V}F_{vol}^{i+1} + \boldsymbol{R}F_{geo}^{i+1}} \tag{11}$$

The values of V and R are now the model's unknowns and can be derived using *N* observations from a certain pixel by minimizing the merit function:

$$M = \sum_{i=1}^{N-1} \frac{\left(\rho_{i+1}\left[1 + VF_{vol}^{i} + RF_{\text{geo}}^{i}\right] - \rho_i[1 + VF_{vol}^{i+1} + RF_{geo}^{i+1}]\right)^2}{day^{i+1} - day^{i} + 1} \tag{12}$$

The minimization is performed by taking partial derivatives and equating them to zero:

$$\frac{dM}{dV} = \frac{dM}{dR} = 0 \tag{13}$$

This leads to the system of Equations:

$$\begin{pmatrix} \sum_{i=1}^{N-1} \Delta^i \rho F_{\text{vol}} \Delta^i \rho F_{vol} & \sum_{i=1}^{N-1} \Delta^i \rho F_{vol} \Delta^i \rho F_{\text{geo}} \\ \sum_{i=1}^{N-1} \Delta^i \rho F_{vol} \Delta^i \rho F_{\text{geo}} & \sum_{i=1}^{N-1} \Delta^i \rho F_{geo} \Delta^i \rho F_{geo} \end{pmatrix} \otimes \begin{pmatrix} V \\ R \end{pmatrix} = \begin{pmatrix} -\sum_{i=1}^{N-1} \Delta^i \rho \Delta^i \rho F_{\text{vol}} \\ -\sum_{i=1}^{N-1} \Delta^i \rho \Delta^i \rho F_{\text{geo}} \end{pmatrix} \tag{14}$$

Where:

$$\Delta^i d = day_{i+1} - day_i + 1$$

$$\Delta^i \rho = (\rho_{i+1} - \rho_i)/\sqrt{\Delta^i d}$$

$$\Delta^i \rho F_{\text{geo,vol}} = (\rho_{i+1} F_{\text{geo,vol}}^{i} - \rho_{i+1} F_{\text{geo,vol}}^{i+1})/\sqrt{\Delta^i d} \tag{15}$$

Through the inversion of Equation 14, every pixel will now have its associated *V* and R parameter. To perform the instantaneous directional correction for every observation, *V* and *R* parameters are needed for every date, so the inversion of the *V* and *R*

parameters is done for five different NDVI populations, using a time composite of five years. A linear regression is performed for *V* and *R* as a function of the NDVI (Equation 16). This retrieves a slope and intercept for every pixel, which allow the computation of *V* and *R* parameters for a certain date given the surface's NDVI value.

$$V = V_0 + V_1 * NDVI$$
$$R = R_0 + R_1 * NDVI \quad (16)$$

These V and R can now be used to calculate the normalized surface reflectance (ρ^N) at θs = 45°, and nadir observation using:

$$\rho^N(45,0,0) = \rho(\theta_s, \theta_v, \phi) * \frac{1 + VF_{\text{vol}}(45,0,0) + RF_{\text{geo}}(45,0,0)}{1 + VF_{vol}(\theta_s, \theta_v, \phi) + RF_{\text{geo}}(\theta_s, \theta_v, \phi)} \quad (17)$$

The values of the weight coefficients $k_{iso}, k_{vol}, k_{geo}$ can then be derived by going back to the original Equation 10, given the values of *V* and *R*.

1.4.3. Factors affecting surface albedo

Typical surface albedo values of different natural surfaces present around the world are shown in Table 6. The lowest albedo values found for the planet correspond to surfaces with a high absorption value, such as water or vegetation. The denser the vegetation, the more energy it will absorb in the shortwave spectrum ($0.2\mu m - 3.0\mu m$) and the lower the albedo value, which explains the differences between the dense coniferous forest (0.05-0.15), deciduous forest (0.15-0.20), croplands (0.18-0.25), which tend to have gaps between the crops, or grasslands (0.16-0.26). Sparsely vegetated surfaces such as desert sand or bare soil present higher albedo values from around 0.05-0.4. This wide range has to do with the water amount present in each surface. Since water is

highly absorbent, soils with low albedo tend to be dark wet surfaces with high soil moisture (0.05-0.15), while dry soils or sand, such as those present in deserts, typically have a higher value (0.2-0.4). Finally, highly reflective surfaces include ice, clouds and snow. In the case of snow and ice, the range of possible values is associated with the impurities present, where higher soot concentration, or crystal size lead to an increase in the probability of photon absorption and subsequently to a reduction of surface albedo. This explains why older snow, which is more susceptible to soot contamination and whose grain size increases with time, has a significantly lower albedo value than fresh snow.

Surface albedo varies spatiotemporally due to both natural and anthropogenic processes happening in the Earth. The biggest natural change occurs when early snowmelt or receding snow in the northern latitudes leads to an increase visibility of the forest cover in those regions. (Loranty *et al.*, 2014a), for example, showed that a gradual increase in tree cover in northern high latitudes from 2006-2010 captured by MODIS data was accompanied by a gradual decrease in albedo (from ~0.75 to around 0.25) in April due to snow-masking effects of vegetation. This massive negative albedo change has profound implications in the Earth's radiative balance and is an important focus of many studies regarding global warming predictions.

Table 6: Typical surface albedo values of different land cover types

Land Cover Type	Surface Albedo
Water	0.06-0.1
Deciduous Forest	0.15-0.20
Coniferous Forest	0.05-0.15
Grassland	0.16-0.26
Cropland	0.18-0.25
Bare soil	0.05-0.4
Desert Sand	0.2-0.4
Ice	0.4-0.7
Clouds	0.35-0.8
Snow	0.4-0.9
Fresh Snow	0.8-0.9

A positive albedo change can also happen, for example due to naturally occurring forest fires. After a fire, the low albedo forest reveals a high albedo bare soil. The question then arises of whether the land cover change's radiative forcing decrease balances out the previous forests' radiative forcing through carbon sequestration. Rather counter-intuitively, studies using ground measurements and satellite data have shown an increase in radiative forcing during the first year after a fire, but provided an overall decrease when averaged over an 80-year fire cycle (Randerson *et al.*, 2006), implying that future increases in boreal fire may not accelerate climate warming.

Regarding human induced changes, deforestation has shown to have a net cooling effect of -1K globally: cooling due to the increase in albedo from the forest-grass land cover at the surface is higher than the warming due to evapotranspiration efficiency in the atmosphere (Davin and de Noblet-Ducoudré, 2010). Another major change happens with the surface change from forest to cropland. (Bounoua *et al.*, 2002) showed using both satellite data and climate models that the change of forest and grassland to cropland cools canopy temperatures up to 0.7^{0}C in summer and 1.1^{0}C in winter. As

Figure 6 shows, the overall effect of natural and anthropogenic land cover changes lead to a decrease in radiative forcing and thus, to the Earth's cooling. However, this cooling effect happens only at the surface level. The overall radiative forcing of the Earth depends on many other atmospheric parameters. This surface cooling is completely masked by the positive radiative forcing of the atmospheric greenhouse gases.

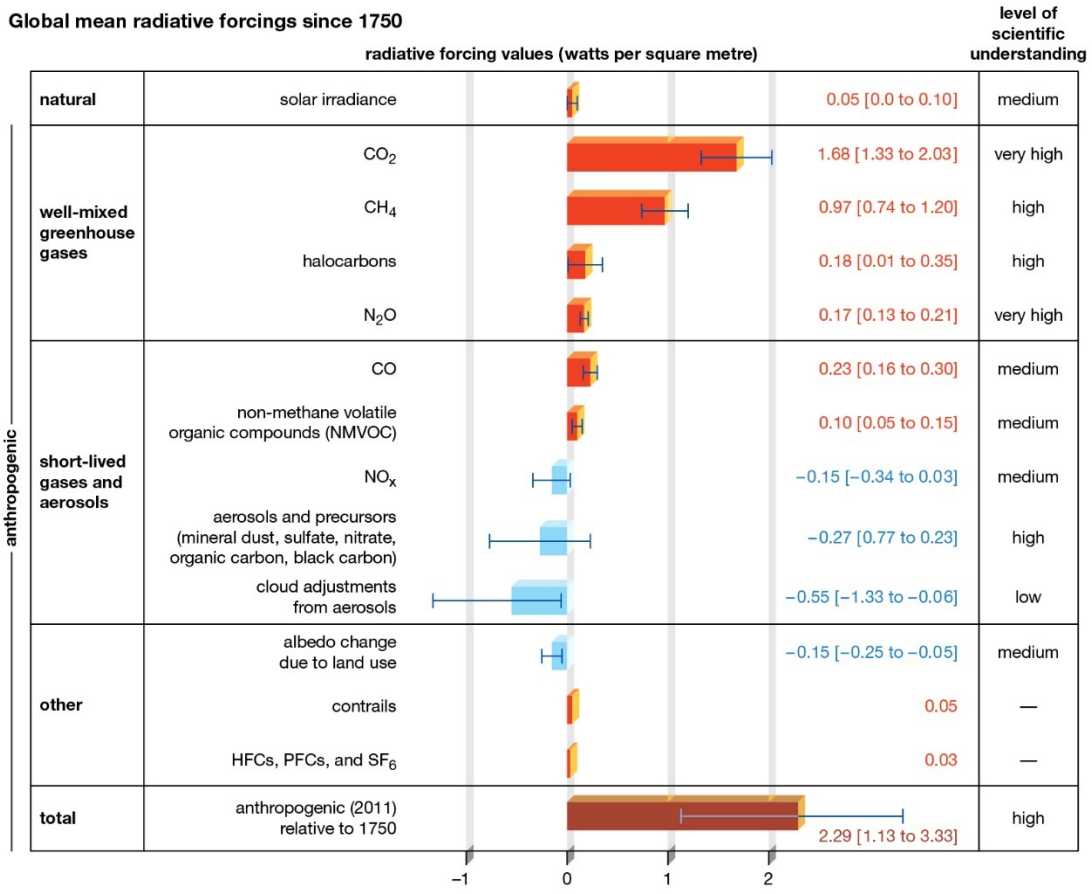

Figure 6: Global mean radiative forcing of the Earth since 1750. Source: IPCC report 2014.

The total warming happening on the Earth induces the appearance of albedo feedback loops, which can further heat or cool the planet. An increasing temperature would lead to changes in extent and duration of snow cover (Chapin *et al.*, 2005a; Déry and Brown, 2007a), aiding the northward expansion of vegetation (Pearson *et al.*, 2013a) and

decreasing the Earth's albedo. This, in turn, would increase the amount of energy absorbed by the Earth, thus increasing the temperature further. The decline in albedo ($\Delta\alpha$) between snow-covered and snow-free conditions represents the strength of the positive albedo feedback associated with these changes (Qu and Hall, 2007a; Loranty *et al.*, 2014a). This feedback is known to be very important for regional climate change and plays a crucial role in Arctic amplification.

1.4.4. Spatiotemporal global albedo

Due to the aforementioned factors, surface albedo presents seasonality on a global basis. Figure 7 shows the temporal evolution of global, northern and southern hemisphere white-sky and black-sky albedos using MODIS data from the MCD43C3 product. In the summer, the average albedo reaches its minimum value, due to the presence of vegetation, while in the winter it reaches its maximum values, due to the presence of snow. The WSA is slightly higher in the summer than the BSA, likely due to changes in the fraction of diffuse radiation (Zhang *et al.*, 2010). The average BSA and WSA values are 0.235 and 0.245, respectively. It is important to note that for the winter months in the northern hemisphere, there are areas without any data, where the solar zenith angle is very low even during daytime. The same happens to the Antarctica pixels in the southern hemisphere.

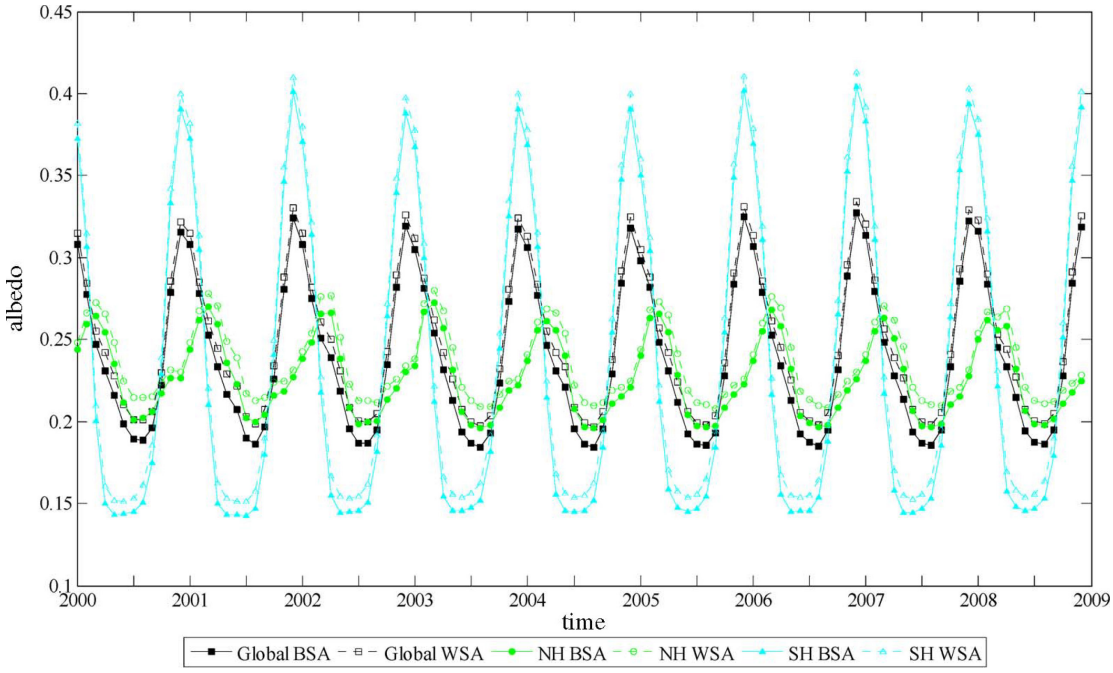

Figure 7: Temporal evolution of global, northern and southern hemisphere white-sky and black-sky albedos using MODIS data from the MCD43C3 product. Figure obtained from (Zhang *et al.*, 2010).

This pattern is observed not only using satellite data, but also when taking into account different data sources from reanalysis and Global Climate Models (GCMs) (Roesch, 2006; Zhang *et al.*, 2010; Liang, Li and Wang, 2012). However, there are still significant differences between the products, ranging from 0.05 in the summer (lowest) to 0.1 in the winter (highest), as shown in Figure 8.

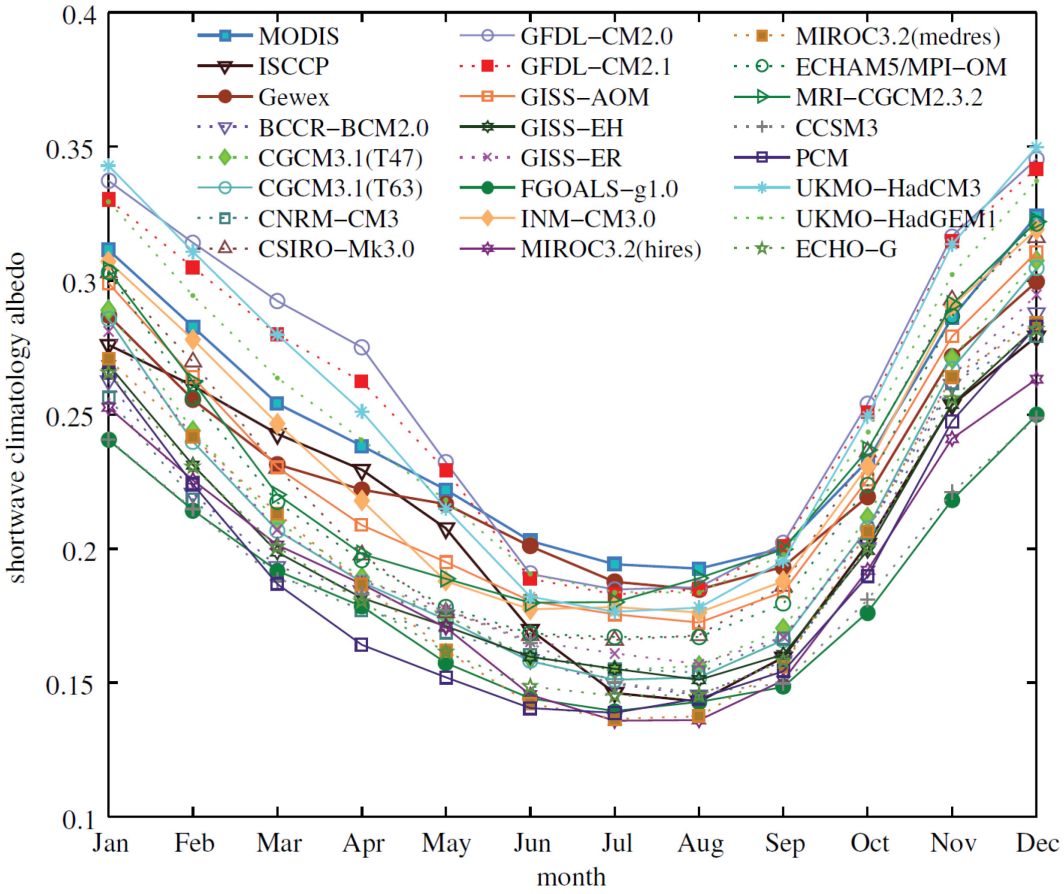

Figure 8: Comparison of different albedo products obtained from Global Circulation Models or reanalysis data with MODIS. Image obtained from (Liang, Li and Wang, 2012)

The overall evolution of surface albedo over the years can be studied by removing the seasonality component of the signal to obtain the trend component. Global trends in surface albedo have been analyzed using MODIS data. These show that the overall planet's surface albedo is remaining approximately constant, with positive trends (1%) in the northern hemisphere caused by receding snow and vegetation expansion(Chen *et al.*, 2015) being counterbalanced by negative trends (-1%) in the southern hemisphere likely caused by positive trends in soil moisture (Dorigo *et al.*, 2012; Liang, Li and Wang, 2012; Chrysoulakis, Mitraka and Gorelick, 2018). Figure 9 shows a map

of the global albedo trends derived from MCD43C3 from 2000-2015 from (Chrysoulakis, Mitraka and Gorelick, 2018).

However, these trends are from a period of 20 years, since current surface albedo products available in the literature rarely cover a longer time span. This means that the trend values presented might not accurately represent the long-term surface albedo change, which might be diminished or enlarged when analyzing 40 years of data.

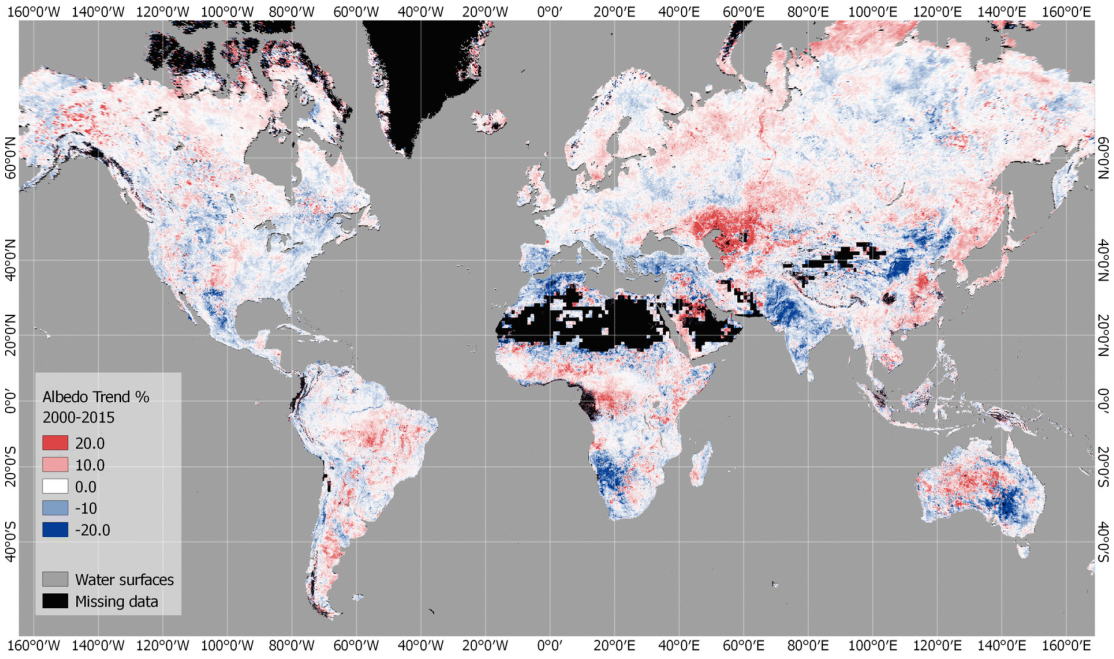

Figure 9: Surface albedo trend derived from MCD43C3 from 2000-2015 from (Chrysoulakis, Mitraka and Gorelick, 2018). Pixels with no data represent either missing data or non-significant albedo trends.

Ho

1.5. Research Questions

As shown above, there is significant value for the scientific community in producing a long-term surface albedo product that satisfies the daily temporal resolution and length of record stipulated by the GCOS requirements. However, the process towards obtaining such a product presents some challenges.

First, the LTDR product requires a spectral harmonization process, which allows for a near-seamless transition between the numerous NOAA satellites that comprise the time series. The first goal of this product is therefore to build upon the existing spectral adjustment methods to find one that minimizes the cross calibration errors among said satellites. In other words:

1. **What are the strategies and associated uncertainties related to the harmonization of the LTDR products for the different NOAA satellites?**

Second, in order to obtain a BRDF model for the LTDR data on a daily basis, the VJB method previously mentioned can be used. However, this method is optimized for MODIS data, and no studies have analyzed its applicability over AVHRR data. Moreover, the product currently provides no BRDF modelling over snow pixels, which has always been a challenge for AVHRR data. This leads to the second goal of this dissertation:

2. **What is the optimum way of modelling the BRDF shape for the LTDR product to obtain surface albedo? How accurately can we calculate this for snow covered pixels?**

It is important to note that, in order for snow albedo to be calculated, a reliable cloud and snow mask needs to be developed for the LTDR product, which currently only discriminates between land and clouds. Once these questions have been answered, and said methods have been found, they can finally be applied to the LTDR product to obtain the surface albedo. The final and main goal of this dissertation is therefore to use this product to create a long-term surface albedo dataset, which satisfies the GCOS requirements for temporal resolution and span of dataset. This would lead me to answer the research question:

3. **What are the global surface albedo trends since 1982? What is the impact of the data record length on the trends?**

1.6. Dissertation design

The overall design of this dissertation is presented in Figure 10. The first step consists in using the data from the LTDR product, along with simulated data to perform the spectral adjustment, and set all AVHRR sensors aboard the different NOAA satellites on the same radiometric scale. The corrected data are then used as an input, along with ancillary data from MODIS and The Modern-Era Retrospective analysis for Research and Applications, Version 2 (MERRA2), to create a mask capable of separating the clear, cloud and snow classes. I then calculate the surface albedo for both land and snow pixels. In the case of land pixels, I correct the BRDF effects by using a variation of the VJB model optimized for AVHRR, and calculate the surface albedo by integration using Equations 2-5. In the case of snow pixels, however, I create a model

that directly calculates the broadband albedo from the AVHRR reflectances and angular information.

The final surface albedo product, (SALSA) is therefore created by combining the broadband albedo from both land and snow pixels. This product is then cross-compared with the well-validated MCD43C3 product spatiotemporally, to analyze the performance and stability of the product. Finally, global trends are obtained and compared to previous trends reported for shorter periods, to observe the differences between the estimates.

Hence, the dissertation is divided into the following chapters:

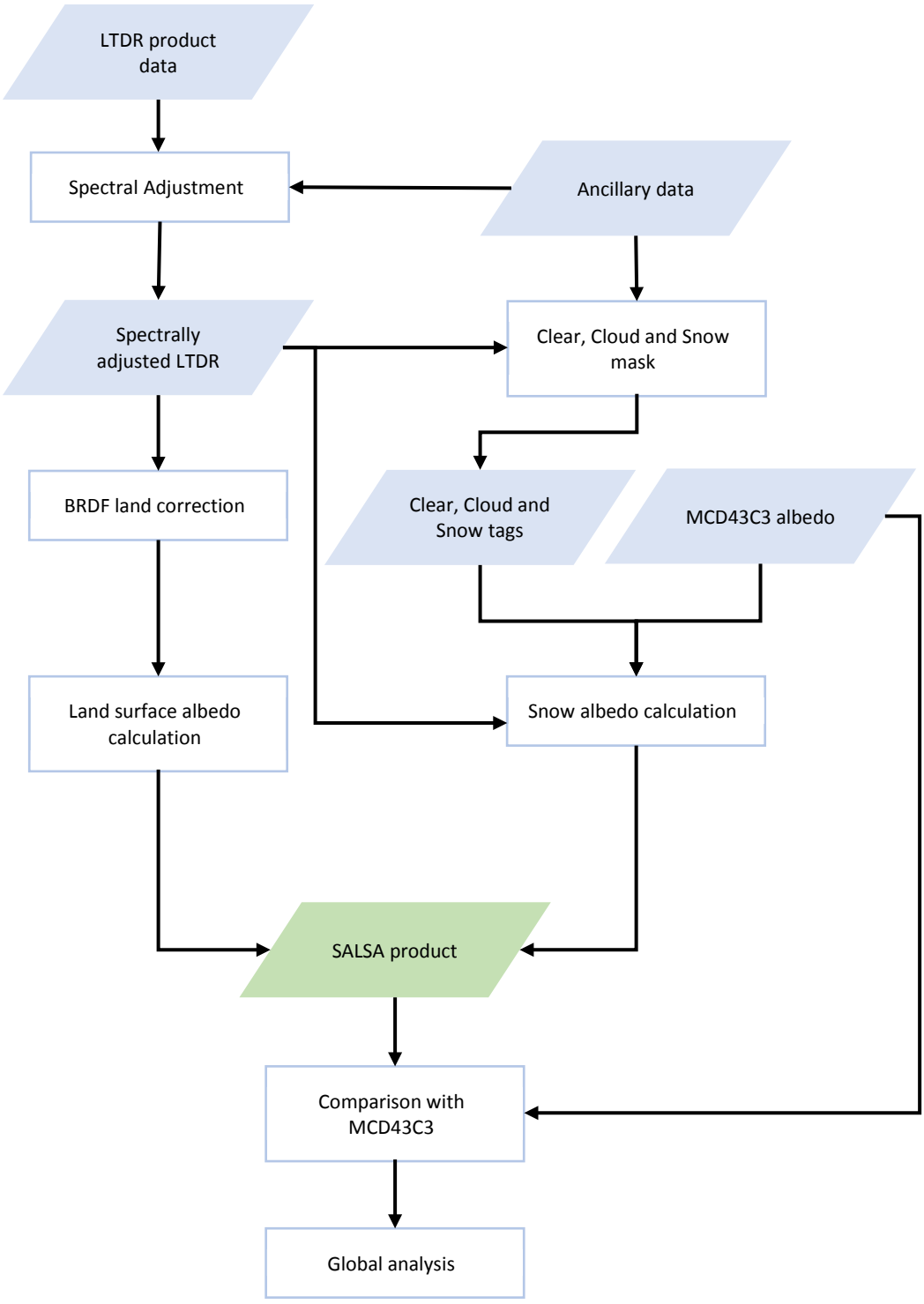

Figure 10: Flowchart of the steps followed in this dissertation.

Chapter 2: Spectral Adjustment

The material presented on this chapter has been previously published in (Villaescusa-Nadal, Franch, Roger, *et al.*, 2019).

2.1. Abstract

Differences in the Relative Spectral Response (RSR) functions of sensors lead to data inconsistencies, which should be harmonized before multi-sensor exploitation. In this chapter, we use spectral libraries to simulate satellite data and build models to correct them. We then explore and compare different models for coarse and medium spatial resolution optical sensors, including Moderate Resolution Imaging Spectroradiometer (MODIS), Advanced Very High Resolution Radiometer (AVHRR), Visible Infrared Imaging Radiometer Suite (VIIRS), Multispectral Instrument (MSI) aboard Sentinel-2 and Operational Land Imager (OLI) aboard Landsat 8. We found that optimal correction of different bands depends on the model used. For the green and near infrared (NIR) bands, a multilinear land cover dependent regression (MR1) improves the Accuracy by up to 80.9%. For the red band, a novel exponential dependence of the Spectral Band Adjustment Factor (SBAF) with the Normalized Difference Vegetation Index (NDVI) provides an Accuracy improvement of up to 72.8%. The best way to correct the NDVI value is to use the corrected NIR and red bands using these models. We apply the proposed methods to 445 BELMANIP2 sites using AVHRR data from the Long Term Data Record (LTDR) from 1982-2017. High NDVI pixels result in 30-year trends varying up to 0.06 when comparing uncorrected to spectrally adjusted NDVI. Further application of these methods to NASA's Harmonized Landsat and Sentinel 2 (HLS) product shows that for the red band and NDVI, our proposed method

provides improved Accuracy (54.6% and 62.5%) over the linear spectral adjustment currently used.

2.2. Introduction

To gain an understanding of land surface processes at a variety of scales, it is increasingly necessary to use data from multiple Earth observation sensors (Chander *et al.*, 2013). By combining similar spatial resolution sensors, we can achieve higher temporal resolutions, increasing our ability to monitor rapidly changing phenomena and increase the opportunity of obtaining cloud-free observations. Additionally, the inter-comparison between different sensors of basic parameters such as the surface reflectance is critical to build consistent databases. However, similar bands from different sensors have different spectral ranges and have a different band efficiency (or Relative Spectral Response). This leads to a significant offset in the values measured, even when observing the same target at the same time (Teillet *et al.*, 2007). Studies have shown differences in the Normalized Difference Vegetation Index (NDVI) value due solely to the Relative Spectral Response (RSR). They can result in discrepancies of 6.3% between QuickBird and SPOT5 (Franke, Heinzel and Menz, 2006) that cause differences in the red and NIR reflectances of 20% and 4%, respectively (Trishchenko, Cihlar and Li, 2002b). It is, therefore, important to place all these sensors on a common radiometric scale, when generating a time series of a certain physical parameter covering different sensor generations and sensor types.

One way to achieve a common radiometric scale is to use an already well-calibrated sensor to calibrate other sensors (i.e. cross-calibration) (Teillet *et al.*, 2001). Cross-calibration is key towards mission continuity, interoperability and data fusion

(Dinguirard and Slater, 1999; Chander *et al.*, 2013), and is critical when the sensor has no onboard reference available or when the vicarious calibrations are limited. This is the case for the NOAA satellites included in the LTDR product. The time-series consists of data from three different sensors onboard 13 different satellites. The RSR function of these sensors differ significantly, resulting in relative differences of around 15% in the red band, 3% in the NIR band and 6% in the NDVI value, when comparing, for example, NOAA9 with NOAA15 (Trishchenko, Cihlar and Li, 2002b). These differences could result in problems when estimating parameters derived from the whole time-series, as they could produce inconsistencies between the sensors and misleading trends in the data, as will be shown in this study. The RSR of different commonly used sensors, along with those in the LTDR product, are shown in Figure 11.

Regarding moderate to high spatial resolution, the Landsat series has been providing 16-day imagery since the 1970's. Due to such low temporal resolution of individual moderate spatial resolution satellites, there is a benefit in combining measurements from similar or analogous sensors aboard different satellites (Skakun *et al.*, 2018). With the launch of Sentinel 2 (Drusch *et al.*, 2012) the combination of Landsat 8 and Sentinel 2 data provides a significant improvement in temporal resolution (Li and Roy, 2017). The Harmonized Landsat/Sentinel-2 (HLS) Project, for example, provides a surface reflectance product combining both satellite's measurements at 30-meter spatial resolution (Claverie *et al.*, 2018). In this case, it's important to consider the directional and atmospheric effects resulting from the difference in overpass time and observation angle of each satellite, along with the spectral correction (Skakun *et al.*, 2018).

The purpose of radiometric adjustment is to correct differences due to discrepancies in the RSR function between analogous bands. These differences can only be compared when the spectral responses of the sensors for a given band have enough spectral overlap (X. Fan and Liu, 2017). Several different ways to correct spectral differences have been reported in the literature and can be generally classified into three main types: band averaging, radiative transfer and statistical regression. The latter is the most commonly used in the literature and consists in using hyperspectral data convolutions (Steven *et al.*, 2003; Kim *et al.*, 2010), remotely sensed observations (Thenkabail*, 2004; Martínez-Beltrán *et al.*, 2009), or radiative transfer calculation (van Leeuwen *et al.*, 2006) to obtain regression coefficients that establish a relationship between analogous bands.

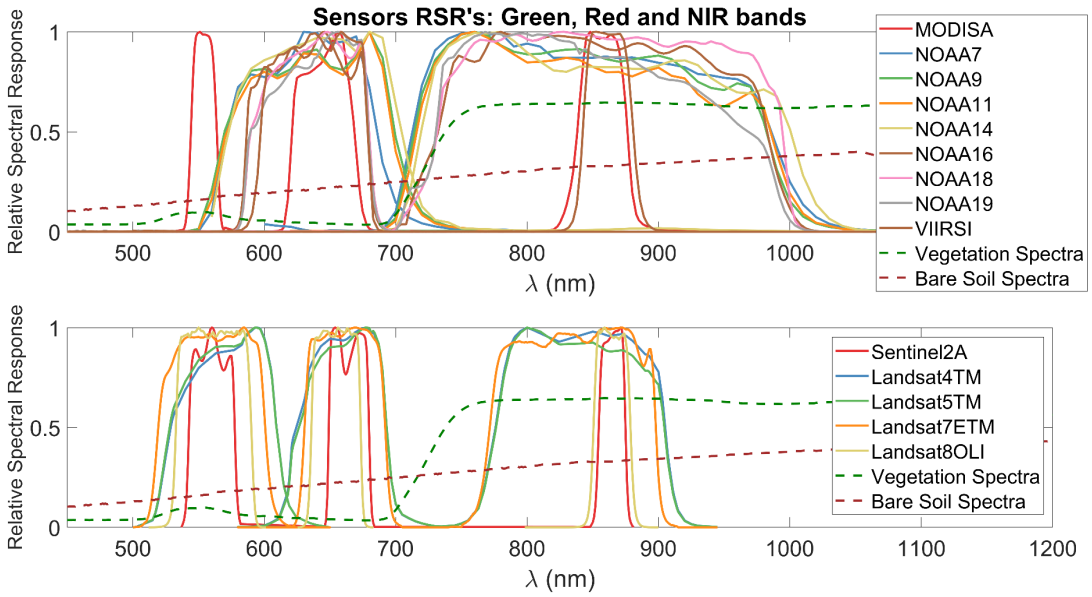

Figure 11: Relative Spectral Response of different sensors commonly used in remote sensing. The dashed lines show a typical vegetation and bare soil spectra.

The most commonly used relationship is the linear regression (Steven *et al.*, 2003; van Leeuwen *et al.*, 2006). It involves using a simple relationship between the reference (ref) and target (tar) sensors to obtain correction parameters, which can later be used to correct any target sensor's observation. This method is used in the HLS product (Claverie, Masek and Ju, 2016), using Landsat-8 as a reference. The main reason behind its popularity is its simplicity and practical use, however it overestimates low NDVI values and underestimates high NDVI values, suggesting that its optimal use is for intermediate NDVI values (Xingwang Fan and Liu, 2017). Previous studies have shown that the reflectance relationships between the red and NIR bands have strong land cover dependencies (Miura, Huete and Yoshioka, 2006), which are not considered when using the linear regression. They can, however, be corrected as a function of the quadratic NDVI (Trishchenko, Cihlar and Li, 2002b; Miura, Huete and Yoshioka, 2006; Fan and Liu, 2016). Differences in the Spectral Band Adjustment Factor (SBAF), defined as the ratio between the target and reference reflectance, can increase up to 30% and 40% in the red and NIR bands, respectively (Trishchenko, Cihlar and Li, 2002b). Fan and Liu (X. Fan and Liu, 2017) determined that the SBAF between Landsat TM and Earth Observing One (EO-1) Advanced Land Imager (ALI) are inherently dependent on NDVI and exhibit nonlinear dependencies. To correct discrepancies between similar NDVI values of soils and sparsely vegetated land cover for varying RSRs,(D'Odorico *et al.*, 2013) added to the regression model the red and NIR bands, providing further information on the land cover type by means of a multilinear regression. The quadratic approach does not seem to correct these non-linearity problems when the spectral differences are big, and the bands are wide for extreme

NDVI values, so we propose an exponential correction function, which models the saturation of high NDVI values for pixels with a high Leaf Area Index (LAI) accurately.

These studies, however, do not hypothesize that different bands should be corrected using different models. The sensitivity analysis performed in (Miura, Huete and Yoshioka, 2006) leads to our hypothesis that the land cover dependencies of bands which overlap with the green peak or red-edge regions in different ways, should be modelled differently. The aim of this chapter is to test said hypothesis by comparing the performance of different spectral adjustment methods on the red, NIR and NDVI, and analyze the impact of the spectral differences on surface reflectance time-series trends calculated from the LTDR product. Section 2.2 describes the materials used for the study. Section 2.3 presents the methodology. Section 2.4 presents the results. Section 2.5 presents a discussion of the results and section 2.6 presents the conclusion.

2.3. Materials

2.3.1. Sensors used

Table 7 shows the optical sensors and spectral bands considered in this study. Same sensors on different missions have different spectral responses. The RSR functions are available at https://cloudsway2.larc.nasa.gov/ and are shown in Figure 11.

Table 7: Passive optical sensors considered and their official band number.

Mission/s	Sensor	Green band	Red band	NIR band
NOAA8, 10	AVHRR/1	-	1	2
NOAA7, 9, 11, 12, 13, 14	AVHRR/2	-	1	2
NOAA15,16,17,18,19	AVHRR/3	-	1	2
Landsat 4, 5	TM	2	3	4
Landsat 7	ETM+	2	3	4
Landsat 8	OLI	3	4	5
Aqua/Terra	MODIS	4	1	2
Sentinel 2A/B	MSI	3	4	8A
Suomi NPP	VIIRS	-	I1	I2

1) MODIS

The Moderate Resolution Imaging Spectroradiometer (MODIS) is an instrument aboard the Terra and Aqua missions, which provides daily measurements at coarse spatial resolution (1km-250m). It acquires data in 36 spectral bands, with a very similar RSR for both satellites. It was designed to produce large-scale global measurements. MODIS is widely used in the remote sensing community due to the quality of its calibration (Justice *et al.*, 2002; Xiong *et al.*, 2010) and validation (Liang *et al.*, 2002; Wan, 2008), so we selected it as a reference sensor. The choice of Aqua over Terra is arbitrary given their almost identical Relative Spectral Response function. In this study, we only consider the red, NIR and green bands, with band numbers 1, 2 and 4, respectively.

2) VIIRS

The Visible Infrared Imaging Radiometer Suite (VIIRS) is an instrument aboard the Suomi National Polar-orbiting Partnership (Suomi-NPP) satellite. It provides daily observations at coarse spatial resolution, similar to MODIS; its purpose is to continue the heritage of the NOAA AVHRR and MODIS products, enabling characterization of the land surface at regional to global scales. We use the I1 and I2 bands, due to the presence of analogous bands in the MODIS or AVHRR sensors.

3) Landsat and Sentinel 2

The Landsat program has been providing information about the Earth at moderate spatial resolution (70-30m) since the 1970's, increasing our understanding of local environmental changes. The most recent satellite (Landsat 8) was launched in 2013, providing measurements every 16 days. The Sentinel 2A satellite, launched by ESA in 2015, has similar characteristics. The Harmonized Landsat/Sentinel2 product provides a combination of measurements approximately every 5 days, correcting for geometric, anisotropic, atmospheric and spectral differences (Claverie *et al.*, 2018).

We downloaded HLS data for seven SURFRAD sites in the US (US Department of Commerce, no date) and 6 sites in Australia (HLS tiles 54HVH, 55HBU, 55HCV, 55HDB, 56HKH, and 56JMQ) where Landsat 8 and Sentinel 2 sensors have coincident observations (131 scenes). The data were corrected for geometric sampling and geographic registration, but in this study were not corrected for directional effects.

The Equator crossing times of the Landsat 8 OLI and Sentinel-2 MSI sensors are close, 10:00AM (L8) and 10:30AM (S2), and the viewing angles from nadir are $\pm 7.5^0$ and $\pm$

10.3^0 respectively (Roy *et al.*, 2017). This means that the illumination conditions for coincident dates are very similar, and the differences in surface reflectance due to the surface anisotropy can be considered negligible for low observation angles. The spectral differences between the L8 OLI and S2 MSI sensors are significant for the green and red bands, but negligible for the NIR bands, with band numbers specified in Table 7. For these reasons, the use of this product for data on the same site and day allows a reasonable comparison between the two sensors whose difference can be attributed mainly to the spectral differences.

4) AVHRR

For this study, we first downloaded the RSR functions for all AVHRR sensors (AVHRR/2 and AVHRR/3) aboard the different NOAA missions. Secondly, we downloaded data from the LTDR product, which is not corrected for spectral effects (Franch *et al.*, 2016a) for the whole AVHRR time series on 445 BELMANIP2 sites. BELMANIP2 sites are an update of BELMANIP1 (Baret *et al.*, 2006a) and were selected because they represent the variability of vegetation types and climatological conditions around the world. The spatial distribution of these sites is shown in Figure 12.

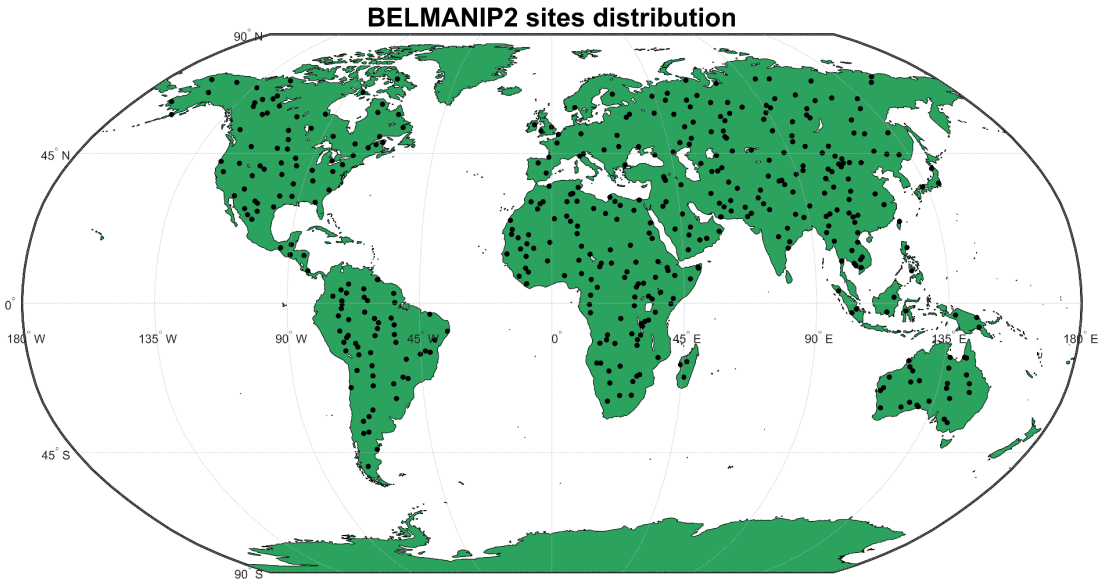

Figure 12: Distribution of the BELMANIP2 (black dots) sites around the world

2.3.2. Spectral Libraries

We downloaded 615 surface reflectance spectral profiles from ground measurements and atmospherically corrected Airborne Visible and Infrared Imaging Spectrometer (AVIRIS) measurements (Kokaly *et al.*, 2003) included in the US Geological Survey (USGS) (Kokaly *et al.*, 2017) spectral libraries. These profiles covered a wide range of land covers, including snow, ice, rocks, soils, vegetation and manmade materials such as asphalt or brick. Overall, they were distributed along the NDVI range from 0-0.93.

2.4. Methodology

2.4.1. Algorithm description

Field measurements are only representative of very specific types of surfaces. When working with coarse resolution data, the measured signal of a given pixel is most often a combination of signals from different surfaces (mixed pixels). Therefore, to make the

field measurements more representative of the remotely sensed signal while also increasing the sample size, we simulated random combinations of these spectra. We did this by linearly combining the reflectance spectra of the 615 field measurements. Up to three different field measurements were combined each time to reproduce a coarse resolution remote sensing pixel. Each one of them is assigned a random weight, which represents the percentage cover of that land type in a certain pixel. The number of possible combinations using 3 different surfaces added up to ~16 million, but we selected a random sample of 500,000 spectra. The NDVI range of the original samples and that of the combined satellite representative samples is shown in Figure 12.

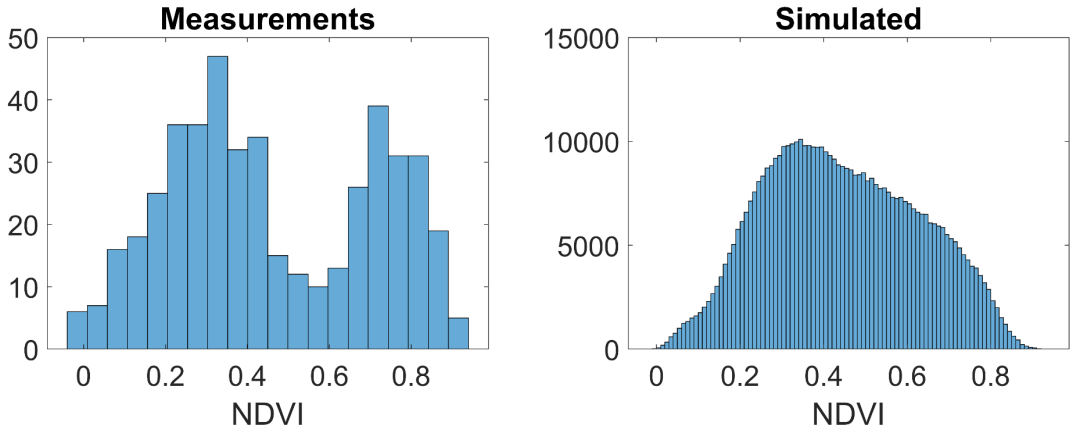

Figure 13: NDVI distribution of the surface reflectance spectra used in this study: a) before mixing spectral reflectance values and b) after mixing spectral reflectance values.

Having selected the reference hyperspectral data, we applied the spectral adjustment to simulate what the different sensors would measure if only the spectral differences between them were considered. This is done by weighing measured reflectances by their RSR and obtaining the simulated reflectances of each band (Equation 18).

$$\bar{\rho}_\lambda = \frac{\int \rho_\lambda RSR_\lambda d\lambda}{\int RSR_\lambda d\lambda} \tag{18}$$

Where ρ_λ is the spectral library's reflectance, the RSR is the Relative Spectral Response function of the sensor and $\bar{\rho}_\lambda$ the simulated reflectance of the sensor. we calculated the ratio of simulated reflectances from two different sensors: a reference sensor $\bar{\rho}_{\lambda,ref}$ and a target sensor $\overline{\rho}_{\lambda,tar}$, also known as the Spectral Band Adjustment Factor (SBAF) using Equation 19.

$$SBAF = \frac{\bar{\rho}_{\lambda,ref}}{\bar{\rho}_{\lambda,tar}} \tag{19}$$

We then proceeded to build the models described in detail in the next section and retrieve the corresponding regression coefficients, using NOAA14 as a reference. These coefficients were applied to the surface reflectance data to allow the comparison of the different methods over different sensor combinations. This comparison is assessed in terms of the Accuracy, Precision and Uncertainty (APU) metrics (Vermote and Kotchenova, 2008a). The Accuracy represents the mean bias of the estimates, against reference data. It is also known as the Mean Bias Error (MBE). The Precision represents the repeatability of the estimate, and it computes the standard deviation of the estimates around the reference values corrected for the bias (Accuracy). Finally, the Uncertainty, or Root Mean Square Error (RMSE), is the deviation of the estimate from the reference.

The surface reflectance bands analyzed are the green, red and NIR, along with the corrected NDVI. The two schemes generally used in the literature for NDVI correction are the distributed and lumped schemes. The former initially corrects the spectral bands and then calculates the NDVI from them (Equation 20), while the latter computes an

intercalibration Equation from the NDVI (NDVI-to-NDVI) (Chen, 1999; Xingwang Fan and Liu, 2017).

$$NDVI_{corrected} = \frac{\rho_{NIR,corrected} - \rho_{red,corrected}}{\rho_{NIR,corrected} + \rho_{red,corrected}} \quad (20)$$

In the case that our hypothesis is valid and different methods are used to correct different bands, we can calculate the NDVI using the distributed scheme through the NIR band corrected using one model, and the red band corrected using a different model.

2.4.2. Spectral methods description

The empirical regression models and SBAF methods that have been tested in this work are the following.

1) Linear Model

$$\bar{\rho}_{\lambda,ref} = a + b \cdot \bar{\rho}_{\lambda,tar} \quad (21)$$

2) Multilinear Regression Model 1 (MR1)

$$\bar{\rho}_{(red,nir),ref} = \beta_1 \bar{\rho}_{red,tar} + \beta_2 \bar{\rho}_{nir,tar} + \beta_3 NDVI + \beta_4 NDVI^2 + \epsilon \quad (22)$$

3) Multilinear Regression Model 2 (MR2)

To characterize the land cover dependencies without the use of the NDVI, which becomes saturated at high LAI values (dense vegetation canopies), we propose a second version of the multilinear regression model which considers products and second order polynomials of the spectral bands:

$$\bar{\rho}_{(g,red,nir),ref} = \beta_1\bar{\rho}_{(g,red),tar} + \beta_2\bar{\rho}_{nir,tar} + \beta_3\left(\bar{\rho}_{(g,red),tar} * \bar{\rho}_{nir,tar}\right) + \beta_4\left(\bar{\rho}_{(g,red),tar}\right)^2 + \beta_5\left(\bar{\rho}_{nir,tar}\right)^2 + \epsilon \quad (23)$$

4) SBAF Quadratic NDVI

$$SBAF = \frac{\bar{\rho}_{\lambda,ref}}{\bar{\rho}_{\lambda,tar}} = a + b \cdot NDVI + c \cdot NDVI^2 \quad (24)$$

5) SBAF Exponential NDVI

An exponential fit is proposed (Equation 9), which is steeper in the high and gentler in the low NDVI values, to account for the NDVI saturation for high LAI values (Haboudane *et al.*, 2004).

$$SBAF = \frac{\bar{\rho}_{\lambda,ref}}{\bar{\rho}_{\lambda,tar}} = a \cdot e^{b \cdot NDVI} + c \cdot e^{d \cdot NDVI} \quad (25)$$

2.4.3. Propagation of Uncertainties

When these adjustment Equations are used with real data to correct for spectral effects, uncertainties from the surface reflectance measurements are propagated to the

corrected reflectance. This means that, even if we found theoretically that a certain model performed better in terms of uncertainty than another model, this might not be the case operationally. For this reason, we simulate surface reflectance data with a 5% uncertainty and analyze the propagated uncertainties for the different models considered. Equation 26 shows the propagated uncertainty (σ_f) of a function f(x,y). (σ_x,σ_y) are the uncertainties of x and y, and $\sigma_{x,y}$ is the covariance between x and y.

$$\sigma_f^2 = \left|\frac{\partial f}{\partial x}\right|^2 \sigma_x^2 + \left|\frac{\partial f}{\partial y}\right|^2 \sigma_y^2 + 2\left(\frac{\partial f}{\partial x}\right)\left(\frac{\partial f}{\partial y}\right)\sigma_{x,y} \quad (26)$$

2.4.4. HLS product

To select low observation angles for Landsat 8, we use the image metadata and extract the images that compose a specific HLS image. We then identify the pixels from the tile with a close to nadir observation (viewing angle < 2°) using the trajectory overpass and tile geolocation. We do the same with Sentinel 2 images and select those pixels, which overlap for both sensors. Overall, we obtained $1.7x10^7$ coincident pixels. From these, we masked pixels with high aerosol values to minimize atmospheric effects.

2.4.5. AVHRR time-series

In this section, we computed the NDVI value from the different sensor's surface reflectance, which combines AVHRR/2 and AVHRR/3 measurements from the NOAA 7, 9, 11, 14, 16 and 18 satellites to produce a 36-year NDVI time series. We then corrected the time-series using the different spectral adjustment parameters explained in detail in the following section and performed a Mann-Kendall correlation coefficient test (Mann, 1945; Kendall and Gibbons, 1990) to analyze the significance of the trends

for each method. We used the Sen's slope method (Sen, 1968) to compute said trends and compared their value for the different methods proposed. The slope's confidence intervals were obtained by using the 95 and 5 percentiles of the individual slopes (Toutenburg, 1975).

2.5. Results

2.5.1. Model comparisons with simulated data

To justify the use of the SBAF exponential model as a correction to the SBAF quadratic model, Figure 14 shows the SBAF dependence with the NDVI between simulated MODIS/Aqua data as a reference sensor and AVHRR/2 (NOAA14) as a target sensor. The blue line represents the quadratic fit, and the red line the exponential fit. The former shows some problems for low (<0.2) and high (>0.7) NDVI values, which are correctly modelled by the latter, evidenced by a decrease of RMSE and MAE of ~3%. shows the absolute values ($x10^{-3}$) and percentage improvements in the APU values for the green, red and NIR bands of 4 different sensors (L8, NOAA14, VIIRS and S2) using the spectral adjustment regression methods considered in this paper. The retrieved coefficients for every sensor combination are available at http://ltdri.org/salsa/. MODIS/Aqua is used as the reference sensor. The improvements are calculated with respect to the spectrally uncorrected surface reflectance data, and the method that shows the highest increase for each case is highlighted. In the green band, the highest improvement in the Accuracy is given by the SBAF exponential method, and the highest improvement in the Precision and Uncertainty is given by the MR1. In the case of S2, for example, the APU values increase up to 36.8%, 26.6% and 33.5%,

respectively. In the Precision and the Uncertainty, the difference between the two methods is around 7% and 6%, respectively. In the red band, the highest improvement in all three metrics is given by the SBAF exponential method. The improvements for the AVHRR/2 aboard NOAA14 are of 72.8% in the Accuracy, 44.2% in the Precision and 62.3% in the Uncertainty.

The values are similar to the SBAF quadratic correction method for most sensor combinations. The worst performance in every case is achieved using the linear method, which provides only a minor correction with respect to the spectrally uncorrected values. In the case of the green L8 band, for example, it only corrects 3.5% of the Accuracy, as compared to the 38.9% provided by the SBAF exponential method. Table 9 is analogous to but for the NDVI. In the NIR band, the MR1 approach provided the best improvements in APU for every sensor combination except for NOAA14, where the MR2 provided a slightly better improvement (~0.3% better in the Accuracy and Precision, and ~0.2% better in the Uncertainty). The overall improvements in APU for NOAA-14 increase up to 80.9%, 57% and 77.85% respectively. For the NDVI value, we add an extra model, the MR1-Exp, to present what the optimum NDVI correction would be: correcting the red and NIR bands with the model that performs best for each band and calculating the NDVI from them. The methods selected were the MR1 for the NIR band and the SBAF-Exp for the red band (MR1-Exp). The best improvement for the NDVI value in terms of the APU is provided by this approach, correcting the Accuracy by 24.7%, 83.7%, 41.7% and 26.7% for L8, NOAA14, VIIRS and S2 sensors respectively.

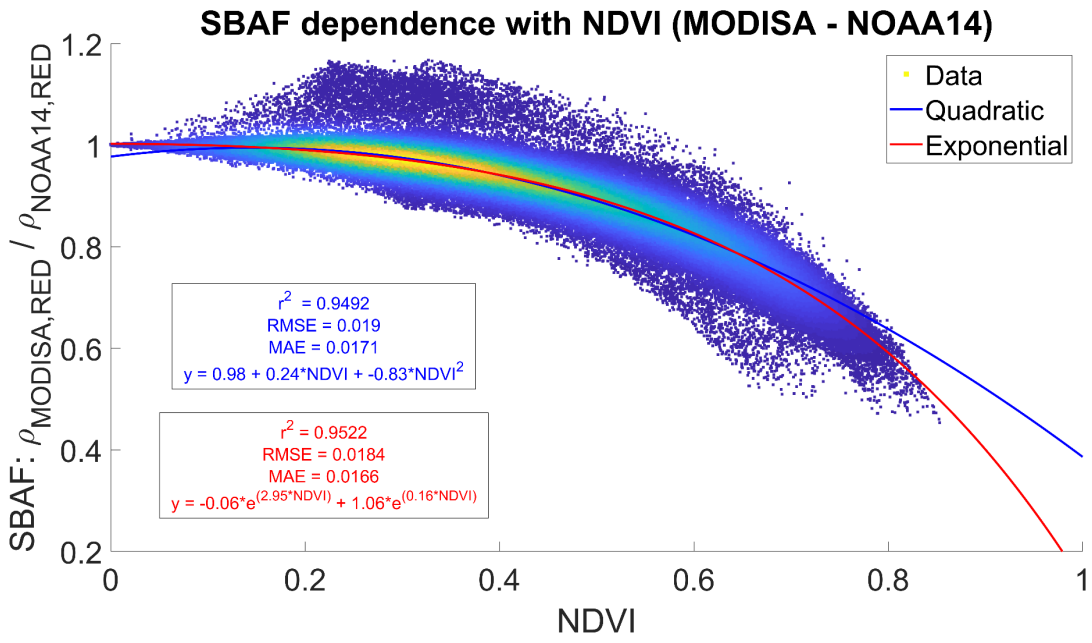

Figure 14: SBAF dependence between MODIS Aqua (reference) and NOAA14 (target) based on the simulated data. The quadratic fit is shown in blue and the exponential fit in red.

Table 8: Accuracy (A), Precision (P) and Uncertainty (U) values and percentage improvement of the spectral adjustment regression methods considered with respect to the uncorrected simulated data. The method with the best improvement for each target sensor is highlighted in green. Absolute values of A, P and U are expressed in 10-3 reflectance for easier comparison.

			Target Sensor			
		Method	L8 OLI	AVHRR/2 (NOAA14)	VIIRS	S2 MSI
GREEN	A	Uncorrected	3.44			2.45
		Linear	3.32 (3.49%)			2.13 (12.88%)
		Multilinear 1	2.27 (34.14%)			1.56 (36.32%)
		Multilinear 2	2.82 (18.07%)			1.89 (22.75%)
		SBAF Quadratic	2.12 (38.49%)			1.58 (35.38%)
		SBAF Exp	**2.10 (38.93%)**			**1.55 (36.84%)**
	P	Uncorrected	4.50			2.98
		Linear	4.36 (3.23%)			2.82 (5.33%)
		Multilinear 1	**3.17 (29.63%)**			**2.18 (26.57%)**
		Multilinear 2	4.02 (10.67%)			2.61 (12.27%)
		SBAF Quadratic	3.27 (27.28%)			2.46 (17.48%)
		SBAF Exp	3.26 (27.65%)			2.40 (19.24%)
	U	Uncorrected	4.50			3.31
		Linear	4.36 (3.65%)			2.82 (14.78%)
		Multilinear 1	**3.17 (29.61%)**			**2.20 (33.46%)**
		Multilinear 2	4.02 (10.46%)			2.63 (20.52%)
		SBAF Quadratic	3.27 (27.51%)			2.46 (25.55%)
		SBAF Exp	3.26 (27.89%)			2.41 (27.17%)
RED	A	Uncorrected	2.70	10.13	2.50	5.92
		Linear	2.31 (14.33%)	6.42 (36.57%)	0.9 (19.34%)	5.07 (14.4%)
		Multilinear 1	2.07 (23.48%)	2.85 (71.84%)	1.77 (29.38%)	4.53 (23.45%)
		Multilinear 2	2.02 (25.21%)	2.78 (72.55%)	1.73 (30.79%)	4.44 (24.94%)
		SBAF Quadratic	1.97 (26.92%)	2.84 (71.97%)	**1.66 (33.57%)**	4.37 (26.24%)
		SBAF Exp	**1.97 (26.99%)**	**2.75 (72.82%)**	1.67 (33.34%)	**4.36 (26.37%)**
	P	Uncorrected	3.70	8.71	3.47	8.33
		Linear	3.34 (9.63%)	8.29 (4.82%)	1.30 (11.27%)	7.53 (9.52%)
		Multilinear 1	3.21 (13.36%)	4.99 (42.73%)	2.96 (14.74%)	7.22 (13.27%)
		Multilinear 2	3.25 (12.05%)	4.96 (42.97%)	3.03 (12.64%)	7.29 (12.47%)
		SBAF Quadratic	3.14 (15.15%)	4.94 (43.31%)	**2.83 (18.42%)**	7.09 (14.86%)
		SBAF Exp	**3.14 (15.17%)**	**4.86 (44.19%)**	2.84 (18.29%)	**7.09 (14.91%)**
	U	Uncorrected	3.91	12.88	3.84	8.67
		Linear	3.34 (14.55%)	8.29 (35.65%)	1.30 (19.91%)	7.53 (13.1%)
		Multilinear 1	3.24 (17.31%)	5.00 (61.18%)	3.02 (21.34%)	7.25 (16.4%)
		Multilinear 2	3.30 (15.61%)	4.98 (61.34%)	3.12 (18.88%)	7.35 (15.2%)
		SBAF Quadratic	3.14 (19.72%)	4.94 (61.66%)	**2.84 (26.05%)**	7.09 (18.23%)
		SBAF Exp	**3.14 (19.74%)**	**4.86 (62.27%)**	2.85 (25.94%)	**7.09 (18.27%)**
NIR	A	Uncorrected	2.09	13.13	1.15	2.17
		Linear	0.87 (58.47%)	4.55 (65.34%)	0.52 (54.75%)	0.91 (57.76%)
		Multilinear 1	**0.84 (59.79%)**	2.56 (80.53%)	**0.50 (56.67%)**	**0.89 (58.81%)**
		Multilinear 2	0.85 (59.42%)	**2.51 (80.85%)**	0.51 (56.01%)	0.90 (58.55%)
		SBAF Quadratic	0.99 (52.56%)	2.71 (79.35%)	0.60 (48.17%)	1.05 (51.73%)
		SBAF Exp	0.98 (53.03%)	2.71 (79.33%)	0.59 (48.44%)	1.03 (52.30%)
	P	Uncorrected	1.18	7.87	0.70	1.26
		Linear	1.18 (0.35%)	5.95 (24.45%)	0.70 (0.00%)	1.25 (0.45%)
		Multilinear 1	**1.15 (3.03%)**	3.41 (56.71%)	**0.68 (3.26%)**	**1.22 (2.66%)**
		Multilinear 2	1.15 (2.60%)	**3.38 (57.02%)**	0.69 (2.40%)	1.23 (2.42%)
		SBAF Quadratic	1.30 (-9.58%)	3.58 (54.46%)	0.78 (-10.85%)	1.37 (-9.14%)
		SBAF Exp	1.29 (-9.11%)	3.59 (54.43%)	0.78 (-10.65%)	1.37 (-8.54%)
	U	Uncorrected	2.39	15.27	1.34	2.48
		Linear	1.18 (50.53%)	5.95 (61.07%)	0.7 (47.42%)	1.25 (49.59%)
		Multilinear 1	**1.16 (51.56%)**	3.41 (77.68%)	**0.69 (48.77%)**	**1.23 (50.45%)**
		Multilinear 2	1.16 (51.38%)	**3.38 (77.85%)**	0.69 (48.34%)	1.23 (50.37%)
		SBAF Quadratic	1.31 (45.26%)	3.59 (76.48%)	0.79 (41.36%)	1.38 (44.38%)
		SBAF Exp	1.30 (45.49%)	3.59 (76.46%)	0.78 (41.48%)	1.37 (44.68%)

Table 9: Analogous results but for the NDVI.

			Target Sensor			
		Method	**L8 OLI**	**AVHRR/2 (NOAA14)**	**VIIRS**	**S2 MSI**
NDVI	**A**	Raw	5.66	41.01	6.83	13.33
		Linear	5.30 (6.35%)	20.92 (48.99%)	4.97 (27.30%)	11.94 (10.40%)
		Multilinear 1	4.50 (20.54%)	7.01 (82.90%)	4.29 (37.14%)	10.18 (23.67%)
		Multilinear 2	4.38 (22.61%)	6.70 (83.67%)	4.08 (40.21%)	9.97 (25.19%)
		SBAF Quadratic	4.28 (24.50%)	6.88 (83.22%)	4.01 (41.30%)	9.77 (26.70%)
		SBAF exp	4.28 (24.43%)	6.78 (83.47%)	4.01 (41.24%)	9.77 (26.69%)
		MR1-Exp	**4.27 (24.69%)**	**6.67 (83.74%)**	**3.98 (41.70%)**	**9.77 (26.71%)**
	P	Raw	7.57	25.39	7.51	17.96
		Linear	7.14 (5.79%)	25.51 (-0.48%)	6.56 (12.6%)	16.59 (7.64%)
		Multilinear 1	6.54 (13.61%)	10.36 (59.18%)	6.07 (19.07%)	15.24 (15.13%)
		Multilinear 2	6.53 (13.85%)	10.14 (60.05%)	6.00 (20.02%)	15.24 (15.15%)
		SBAF Quadratic	6.44 (15.04%)	10.17 (59.95%)	5.78 (22.98%)	15.03 (16.31%)
		SBAF exp	6.43 (15.05%)	10.08 (60.28%)	5.78 (22.97%)	15.03 (16.31%)
		MR1-Exp	**6.43 (15.16%)**	**10.02 (60.53%)**	**5.78 (23.02%)**	**15.03 (16.32%)**
	U	Raw	7.58	47.77	8.83	18.05
		Linear	7.14 (5.78%)	25.79 (46.01%)	6.56 (25.72%)	16.6 (8.07%)
		Multilinear 1	6.59 (13.04%)	10.38 (78.27%)	6.19 (29.92%)	15.30 (15.27%)
		Multilinear 2	6.58 (13.11%)	10.16 (78.73%)	6.16 (30.26%)	15.32 (15.13%)
		SBAF Quadratic	6.45 (14.88%)	10.17 (78.71%)	5.83 (34.01%)	15.04 (16.68%)
		SBAF exp	6.45 (14.89%)	10.08 (78.89%)	5.83 (34.00%)	15.04 (16.67%)
		MR1-Exp	**6.44 (15.05%)**	**10.02 (79.02%)**	**5.83 (34.00%)**	**15.04 (16.71%)**

2.5.2 Propagation of Uncertainties

Figure 15 shows the propagated relative and absolute uncertainties (solid line-left axis and dashed line-right axis, respectively) for the adjustment functions used in this study, as a function of the NDVI. The red and blue lines represent the uncertainty for the red and NIR bands. There are different red-NIR combinations that would yield the same NDVI values, so every curve represents the average uncertainty of every NDVI value, hence the non-linear shapes. The last graph compares the propagated relative and absolute uncertainty for the distributed (red) and lumped (blue) methods. The data was modelled using MODIS Aqua as a reference and Landsat 8 as a target sensor, as an example. These results show that the absolute values are almost identical between every method and band, but that the relative uncertainties vary up to ~1% for the red band and stay constant for the NIR band. Other sensor combinations with a higher NDVI

dependency exhibited even higher differences in the relative values. In the NDVI comparison, the absolute uncertainty of the distributed method is slightly lower than the lumped method, but the relative uncertainty is very similar, becoming very high for low NDVI values.

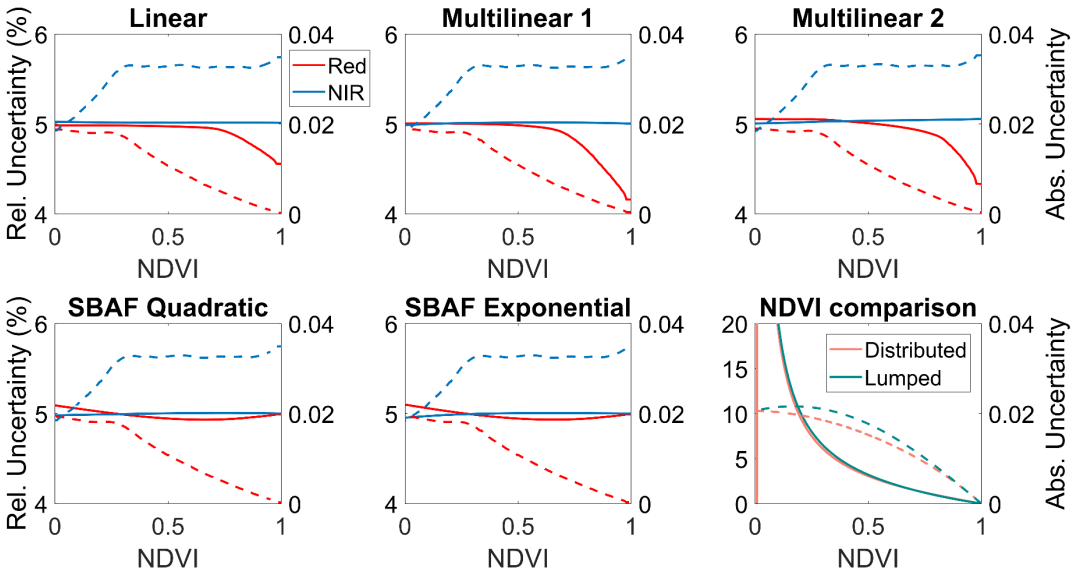

Figure 15: The first five graphs show the propagated relative (solid line - left axis) and absolute (dashed line - right axis) uncertainties for the different models applied as a function of the NDVI. The red and blue lines represent the values for the red and NIR bands, respectively. The bottom right graph compares the propagated relative and absolute errors for the distributed (red) and lumped (blue) methods. These results were modelled using MODIS Aqua as a reference and Landsat 8 as a target sensor, as an example.

2.5.3. HLS data

We calculated the average uncertainty for the Landsat8 and Sentinel2A sensors, obtaining a percentage difference of ~1.5%, ~3.0% and 0.03% for the green, red and NIR bands, respectively.

Figure 16 shows the Accuracy (orange), Precision (green) and Uncertainty (blue) comparison (right axis) when no spectral adjustment, a linear spectral adjustment (used in the official HLS product) and the best modelled adjustment (following last section's

conclusions) are applied using Sentinel 2A as a reference. The purple line represents the specified Uncertainty based on the theoretical error budget of the Collection 5 MODIS (Vermote and Kotchenova, 2008a). The distribution of each band can also be seen through the histogram plotted on the left axis.

For the green band, the MR1 model overestimates the effect of the spectral adjustment, increasing the Accuracy value from 0.001 to 0.0026. The red band, however, shows a significant improvement in the average Accuracy of 54.6% with respect to using no spectral correction, with a similar average Uncertainty and Precision values. In the case of the NIR band, because the spectral responses of both sensors are almost identical, there is no discernible difference between the different methods and the APU values remain the same. Finally, the NDVI's Accuracy is also improved by 62.5%, driven by the red band's improvement, maintaining a similar Precision but increasing the Uncertainty from 0.0267 to 0.0254 (~5%). The linear correction, on the other hand, improves the green band's average Accuracy by 15%, but decreases its average Accuracy by 25% in the red band and by 41% in the NDVI value.

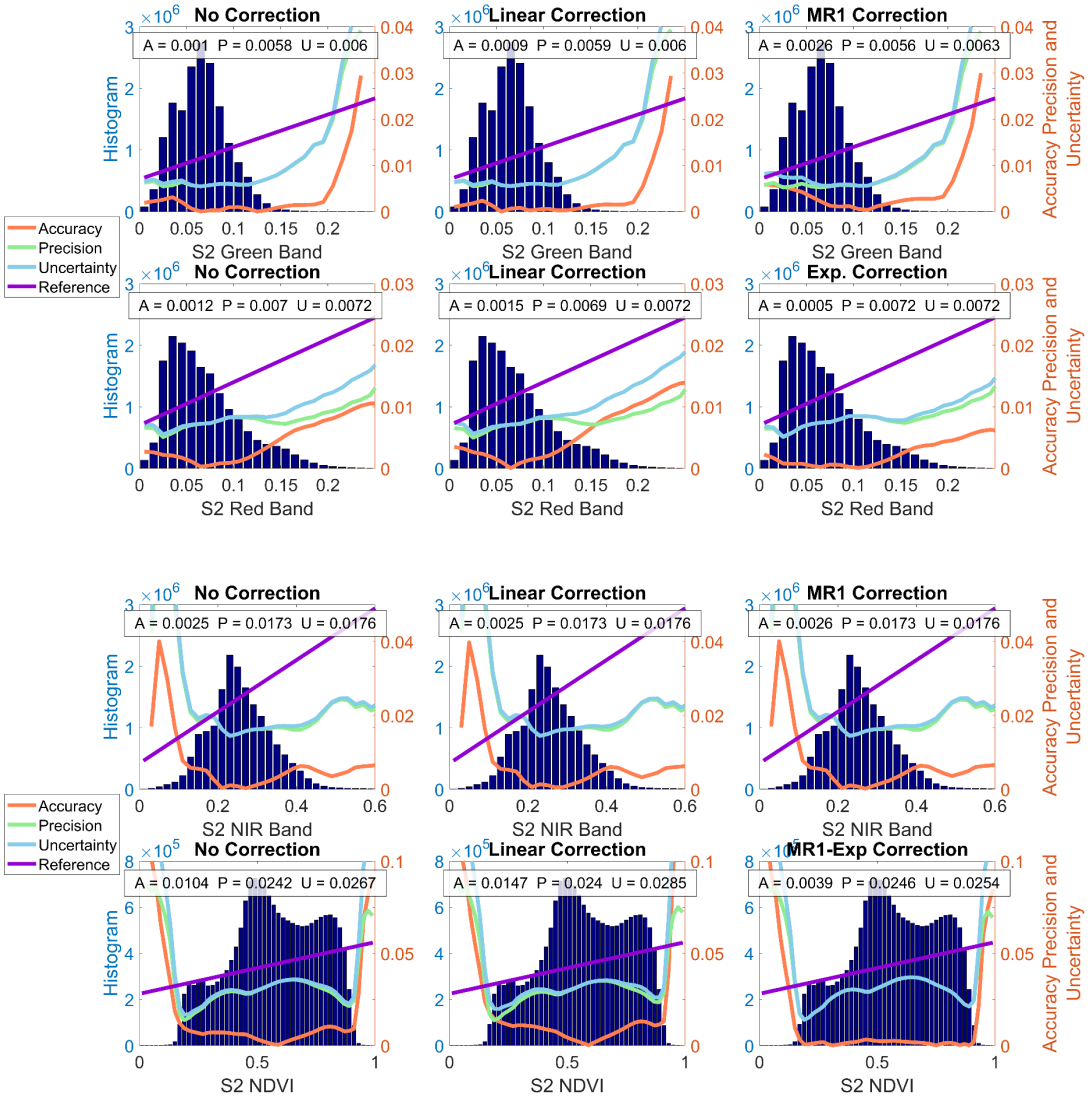

Figure 16: The left axis shows the histogram of the green, red, NIR bands and NDVI values. The right axis shows the Accuracy (orange) Precision (green) and Uncertainty (blue) (APU). The purple line represents the specified Uncertainty based on the theoretical error budget of the Collection 5 MODIS (Vermote and Kotchenova, 2008b).

2.5.4. AVHRR time-series

Figure 17 shows the difference between the NDVI trends computed using no spectral adjustment and using the MR1-Exp correction method as a function of the NDVI. The full 445 BELMANIP Site pixels containing different land surface types are considered. The results show how the difference is almost zero for NDVI<0.2 but increases linearly

with the NDVI, reaching discrepancies of ~0.05 for high NDVI values. The error bars for the difference have been propagated from the individual bars following Equation 26.

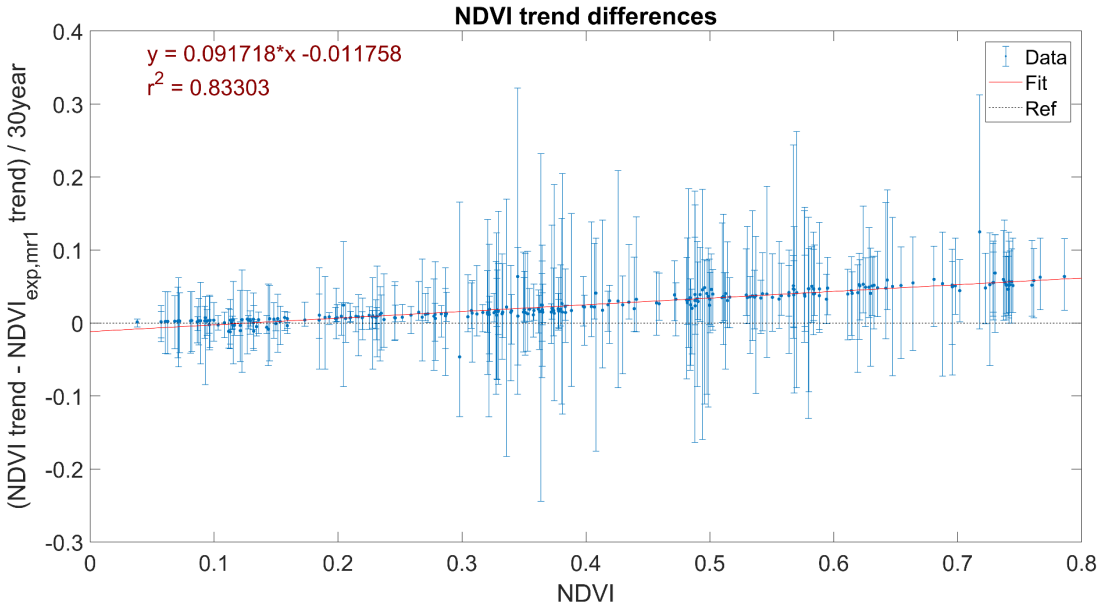

Figure 17: NDVI trends differences between using no spectral adjustment correction and using the MR1-Exp correction as a function of the NDVI for 445 BELMANIP2 Site pixels. The red solid and black dotted lines represent the least squares fit and the reference, respectively.

2.6. Discussion

2.6.1 Model comparisons with simulated data

The reasoning behind these land cover dependencies is investigated in the sensitivity analysis performed in (Miura, Huete and Yoshioka, 2006), which showed that the green peak region at 550nm, along with the red-NIR transitional region (680-780 nm) are the key factors in producing nonlinear patterns; spectral bands which are wide enough to cover these spectral regions will exhibit nonlinear land cover dependencies. The red band is the only band that could have a wide enough RSR to cover both regions.

The results in Table 8 and Table 9 confirmed our hypothesis that the models that provide the best cross-calibration performance differ between different bands, depending on how much and how many of these critical regions they cover. These results provide evidence that the green band's spectral bandpass differences also exhibit land cover dependencies as is shown in the literature for the red and NIR bands (Trishchenko, Cihlar and Li, 2002b; Miura, Huete and Yoshioka, 2006; Fan and Liu, 2016). In the green band, the MR1 method was shown to be the best method in terms of Precision and Uncertainty, but not so much in the Accuracy. The poor performance of the MR2 method in this band is due to two different factors. First, the combination of the green-NIR bands to characterize land cover dependencies is not as strong as the red-NIR combination, despite the high correlation between the red-green bands. Second, the MR2 method is more likely to perform better when the LAI values are high and the NDVI saturates. In the case of the green band, the RSR functions are rarely wide enough to allow this to happen. For the NIR band, however, when the NDVI dependencies are very high due to a large bandwidth, as is the case of NOAA14 compared to MODIS/Aqua, the MR2 characterized the land cover dependencies better by using the interaction terms between the red and NIR bands instead of the NDVI. This is evidenced with the better performance of the MR2 in Accuracy, Precision and Uncertainty.

In the red band, the SBAF exponential approach provides the best improvement of APU values, suggesting that not only is it preferred to the SBAF quadratic method when the RSR differences are high, but also when they are of similar value. When these differences are small, the simplicity and linearity of the three parameters provided by

the SBAF quadratic method is recommended. When correcting the NDVI values, we found that, just like Fan and Liu 2017 (Xingwang Fan and Liu, 2017), the distributed scheme yielded better results. Among the distributed scheme, we found that the best way to correct the NDVI value is to use the MR1 corrected NIR band and the SBAF exponential corrected red band, as opposed to using NIR and red bands corrected using the same model.

2.6.2. Propagation of Uncertainties

The small discrepancy in the relative and absolute errors between the different models indicates that the choice of the correction Equation does not introduce significant errors in the spectral adjustment. We can safely select the best method in terms of the theoretical performance through the APU values. Independently of the magnitude of the uncertainty differences, the adjustment significantly increases the accuracy of the data. This bias cannot be accounted for with the uncertainty propagation.

When analyzing the NDVI computation, the small differences between the lumped and distributed methods point to a similar conclusion; there is not a preferable way to compute the NDVI in terms of uncertainty propagation. Given that the distributed method provides a better improvement in APU values with respect to the modelled data, it is still chosen as the preferable option.

2.6.3. HLS product

The discrepancies between the data and the model observed in the green band are likely due to the small spectral adjustment discrepancies (~1.5%) and the presence of other sources of error of the same order. Comparing the spectral differences between two

satellites with similar RSR functions is always a difficult task, given the small contribution it has on the disagreement between the data compared to other sources of error. In this case, we selected view zenith angles close to nadir observation to minimize the effects due to the surface's anisotropy, but because we were working with surface reflectance, errors due to sensor calibration, atmospheric correction, and pixel misregistration could appear. From these errors, the sensor calibration has a performance of better than 3% (Zhang *et al.*, 2018), and atmospheric correction after sensor calibration propagation has uncertainties of ~7% and ~4% in the green and red bands, respectively. These values are higher than the spectral adjustment differences (~1.5% and ~3%) (Vermote *et al.*, 2016; Claverie *et al.*, 2018). For this reason, the discrepancies between the data and the model observed in the green band for this study are expected. The unbiased NIR band indicates that errors due to misregistration are negligible, because L8 and S2 NIR RSRs are almost identical. In the case of the red band and NDVI, the results in Figure 16 show that the use of a model that accounts for land cover dependencies like the SBAF exponential, increases the Accuracy of the product by 54.6% and 62.5%, respectively.

2.6.4. AVHRR time-series

The results in Figure 17 show that the trends of NDVI values pixels are sensitive to the spectral adjustment method used and could even change from being positive to negative outside of the error margin when the NDVI value is high. For low NDVI values, however, the difference is negligible. This is expected, given that the differences between the reference and target sensor increase with the NDVI. Overall, the trends are

overestimated, especially for NDVI values higher than 0.4, when land cover dependencies start becoming evident**.** In the case of the red and NIR bands, not shown in this paper, the trends were underestimated for the red band and overestimated for the NIR band, especially when the NDVI value is high. These results highlight the importance of an accurate spectral adjustment when computing long-term trends of the NDVI and surface reflectance data.

2.7. Conclusions

Obtaining spectral coefficients, which can be applied to global data, requires a large spatial and temporal distribution of measurements that only satellite data can provide. As long as other sources of error are comparable to the spectral adjustment differences, this becomes a difficult task. Until then we must rely on models that can simulate satellite data, and our approach of linearly combining field measurements addresses this. The regression parameters retrieved are operationally convenient and provide a significant correction of the spectral effects for coarse to moderate resolution satellite sensors. These results benefit existing cross-correlation methods by allowing a smoother transition between different sensor generations and facilitating the use of a time series using data from multiple satellites, present for example in the LTDR product.

The methodology from this study was replicated for the thermal bands, using simulations from the MODerate resolution atmospheric TRANsmission code (MODTRAN) to create the reflectance spectra. Coefficients for all of the sensors used in the LTDR product and this dissertation can be found in Appendix A, Tables A1-A5.

Chapter 3: Clear, Cloud and Snow mask

The material presented on this chapter has been submitted to the Transactions on Geoscience and Remote Sensing and is currently under review with revisions.

3.1. Abstract

The Long Term Data Record (LTDR) has the goal of developing a quality and consistent Advanced Very High Resolution Radiometer (AVHRR) surface reflectance and surface albedo products dating back to 1982 at 0.05° spatial resolution, using the Moderate Resolution Imaging Spectroradiometer (MODIS) instrument as a reference. Distinguishing between cloud and snow is of critical importance when analyzing global albedo trends globally, for they influence the Earth's energy balance through positive and negative feedbacks. However, this task is specially challenging when working with AVHRR given its limited spectral bands. Therefore, the current version of the LTDR does not distinguish between snow and clouds. To this end, we propose the MODIS-based AVHRR Class Separation Algorithm (MACSSA), whose goal is to identify clear land and snow pixels using AVHRR data. We make use of a combination of optical and thermal information from MODIS data (spectrally adjusted to look alike AVHRR data), reanalysis data from MERRA2 and MODIS monthly climatology. These are used as inputs for two different Support Vector Machine (SVM) models, which are then applied to AVHRR data from the LTDR product to retrieve the MACSSA predicted tags. These are compared first against reference tags retrieved from the MYD10C1 product over pixels with less than 2 minutes overpass time difference between MODIS Aqua and NOAA16-19, distributed all around the world, and second against the Climate Change Initiative Cloud (Cloud_cci AVHRR PM) project. We found the

product to be very accurate in identifying clear land pixels, with a Probability of Detection of clear pixels (POD_{clear}) of 97%. The discrimination of snow and clouds shows a POD_{snow} of 88%, which is encouraging given the spectral limitations of the AVHRR sensor.

3.2. Introduction

Surface albedo retrieval methods generally differ between snow and snow-free pixels, so a reliable knowledge of the surface type is vital. This means that a cloud mask with the ability to accurately discriminate between snow and clouds is required, because, despite them having similar albedo values, the implications they have on the Earth's energy budget are profoundly different (Thackeray and Fletcher, 2016).

Misclassification of clouds can lead to significant errors in the retrieval of biophysical or atmospheric parameters (Kaufman *et al.*, 2005; Gomez-Chova *et al.*, 2007). Cloud detection algorithms normally make use of the optical and thermal bands available in satellite sensors; clouds tend to be brighter and colder than the underlying surface. However, the capacity to detect clouds and, more importantly, to discriminate between clouds and snow, depends heavily on the sensor's design and characteristics. Sensors with bands in the 0.66μm and 1.6μm window, for example, are able to calculate the NDSI, which identifies snow pixels with a high degree of accuracy (Zhu and Woodcock, 2012). Sensors without thermal bands, such as Multispectral Instrument (MSI) aboard Sentinel-2, have to rely on angular techniques such as cloud parallax (Skakun *et al.*, 2017; Frantz *et al.*, 2018). Other methods include multi-temporal cloud screening (Mateo-García *et al.*, 2018) or the use of feature identification such as color, texture and shape (Zhang *et al.*, 2019). In the case of the AVHRR sensor, the absence

of critical bands limits the information available to tackle this issue. There are two AVHRR generations present in the LTDR product, formed by the sensors AVHRR/2 and AVHRR/3. Table 10 shows the bands available in each one. The AVHRR/2 has two optical channels (0.63 and 0.86 μm) and three thermal channels (3.7, 11, and 12 μm), while the AVHRR/3, launched on satellites from 1998 onward, and has an extra band (1.6μm), however, only one of the 3.7μm or 1.6μm is available at any given time.

Table 10: MODIS and AVHRR analogous bands and their bandwidth in µm. Band 3A is only available on AVHRR/3, aboard for the first time in NOAA15, but only either band 3A or band 3B are activated at a given time.

MODIS Terra/Aqua		AVHRR/2		AVHRR/3	
Band	λ (µm)	Band	λ (µm)	Band	λ (µm)
B1	0.62-0.67	B1	0.58-0.68	B1	0.58-0.68
B2	0.84-0.88	B2	0.725-1.00	B2	0.725-1.00
B6	1.63-1.65	-	-	B3A	1.58-1.64
T20	3.66-3.84	T3B	3.55-3.93	T3B	3.55-3.93
T31	10.78-11.28	T4	10.30-11.30	T4	10.30-11.30
T32	11.77-12.27	T5	11.50-12.50	T5	11.50-12.50

In the optical spectrum, bands in the red (0.6 µm) and NIR (0.8 µm) are very useful to discriminate clear land from cloud and snow, since they appear much brighter than the underlying background. The use of the red band is preferred, since the NIR band can give high values for dense vegetation (Khlopenkov and Trishchenko, 2007). The NDVI is also useful in this regard, especially with the idea of using climatology information from MODIS. It is strongly related to the vegetation biomass (Goswami *et al.*, 2015),

and therefore presents a clear seasonality, which can be exploited. For snow and cloud discrimination, however, the use of the red and NIR bands alone is insufficient, for they have similar values in both bands. Nonetheless, when combined with other variables, they are useful towards separating the classes defining thresholds along a hyperspace. Identification of clear land can be hampered for high SZA (>86°), so studies have made use of the BRDF corrected red band to tackle this issue (Dybbroe, Karlsson and Thoss, 2005c; Khlopenkov and Trishchenko, 2007; Musial *et al.*, 2014). The band in the SWIR (1.6 μm) carries information about the microphysical state of the cloud and presents significant contrast between cloud and snow (Musial *et al.*, 2014). It is also useful for the detection of low water clouds over snow-covered surfaces. In the absence of this band, the reflectance components of the 3.7 μm band can be used as an alternative (Heidinger, Frey and Pavolonis, 2004).

In the thermal bands, the temperature difference between 3.7 μm and 12 μm and between 10.8 μm and 12 μm is used for the detection of thin cirrus clouds or the estimation of water vapor concentration (Roger and Vermote, 1998). The difference between 10.8 μm and the skin temperature (Ts) can be used to detect cirrus and optically thick clouds (Dybbroe, Karlsson and Thoss, 2005a). This is because the 10.8 band is slightly affected by the absorption of atmospheric gasses (Musial *et al.*, 2014), so it can be assumed that there are clouds if the difference between surface and brightness temperature is large. Finally, in the 3.7 μm band, clouds have a higher brightness temperature than snow, and allow for a slight discrimination between the classes (Zhu and Shi, 2018).

Recent attempts in the literature have relied on ancillary data from climate models to complete the limited information available in the AVHRR sensor with a reliable degree of success (Dybbroe, Karlsson and Thoss, 2005b; Khlopenkov and Trishchenko, 2007; Musial *et al.*, 2014), but present lower accuracy when using AVHRR data without the 1.6μm band (Dybbroe, Karlsson and Thoss, 2005c; Musial *et al.*, 2014), or are optimized for a certain location and are not recommended for global application (Khlopenkov and Trishchenko, 2007). Musial et al. (Musial *et al.*, 2014), for example, compared their Probabilistic Cloud Mask (PCM) cloud and snow detection algorithm using AVHRR with the MOD10A1 product (Hall *et al.*, 2002) and obtained a probability of detection of snow of ~ 60% when using the 1.6μm channel and of ~40% when using the 3.7μm instead. Since the LTDR product uses afternoon satellites, which have very limited or no access to the 1.6μm channel, the computation of a reliable mask without the use of said band is of great necessity, especially in the context of producing an accurate surface albedo product.

In the current version of the LTDR product, a global cloud/clear mask distinguishes the two classes by using monthly climatological information from MODIS band 1 data. This simple approach provides a higher accuracy than using the previously used Clouds from AVHRR (CLAVR) algorithm (Stowe, Davis and McClain, 1995; Franch *et al.*, 2016b), but lower than other cloud masks available for AVHRR data (Dybbroe, Karlsson and Thoss, 2005c; Khlopenkov and Trishchenko, 2007; Musial *et al.*, 2014), when comparing the results with MODIS data. Moreover, it does not provide a method to discriminate between cloud and snow. The main goal of this study is, therefore, to improve the current cloud mask by building on the current approach, and to create a

reliable cloud/snow mask that yields high accuracy for AVHRR data and does not require the use of the 1.6μm band. We firstly created a model using MODIS Terra data, which is spectrally adjusted to look as if it was acquired by AVHRR. We call this data MODIS AVHRR-like data. Then, we used this information and derived thresholds to apply them to AVHRR data on pixels within 2 minutes of the MODIS overpass. This way we ensure that the cloud masking reported by MODIS can be applied to the AVHRR data as truth without significant amounts of error.

The following chapter is divided as follows. Section 3.2 describes the introduction and rationale of features used in the literature. Section 3.3 presents the materials and workflow and explains the methodology used. Section 3.4 shows the main results of this paper, which are discussed in Section 3.5. Finally, we present our conclusions in section 3.6.

3.2. Materials and methods

3.2.1. Data acquisition

Table 11 shows a summary of the data used in this study. We downloaded all surface reflectance AVHRR bands from the LTDR product from 1982-2020 along with angular and overpass time information. We then obtained MODIS Terra/Aqua data from 2000/2002 to 2020. In this case, we downloaded only those bands that are analogous to AVHRR bands, as shown in Table 10 along with angular, overpass time and water vapor information from the products MOD/MYD09. Both MODIS and AVHRR data are available for download through https://ladsweb.modaps.eosdis.nasa.gov/. We downloaded the Skin Temperature (T_s) and the Water Vapor (WV) from Modern-Era

Retrospective Analysis for Research and Applications, Version 2 (MERRA2) data, since the LTDR product has no water vapor information for data before NOAA16. The MERRA2 reanalysis provides hourly data at 0.5° lat x 0.625° lon resolution globally. To match the spatial and temporal resolutions to the satellite information used, we interpolated to CMG resolution and MODIS/AVHRR overpass times. Finally, to create reference tags for snow and cloud, which we use to validate the model, we downloaded the daily cloud, clear and snow percentage information at CMG spatial resolution from the MOD10C1 product, available at https://nsidc.org/data/MOD10C1/versions/6, as well as daily cloud masks at CMG spatial resolution from the Cloud_cci AVHRR PMv3 dataset (Stengel *et al.*, 2017, 2020).

Table 11: Satellite and reanalysis data used in this study.

Name	Sensor	Spatial Resolution (°)	Frequency	Coverage	Time span
LTDR	AVHRR	0.05	Daily	Global	1982-2020
MYD09	MODIS Aqua	0.05	Daily	Global	2002-2020
MOD09	MODIS Terra	0.05	Daily	Global	2000-2020
MYD10C1	MODIS Aqua	0.05	Daily	Global	2002-2020
MOD10C1	MODIS Terra	0.05	Daily	Global	2000-2020
Cloud_cci AVHRR PM	AVHRR	0.05	Daily	Global	1982-2016
MERRA-2	Reanalysis	0.5° lat x 0.625° lon	Hourly	Global	1982-2020

3.2.2. Data location

We downloaded all of the data specifically in two subsets. The first subset is for the creation of thresholds that will aid in the cloud and snow identification using MODIS

data. We downloaded multispectral information from BELMANIP2 (Baret *et al.*, 2006b) pixels and expanded the database to include some snow pixels in Antarctica, Greenland and in snow-prone mountains. The specific bands downloaded are shown in section 2.4. The total number of pixels is 494, and the total number of dates is 6889, adding up to a total of ~3.4 million points. Figure 18 shows the overall spatial distribution of the data points.

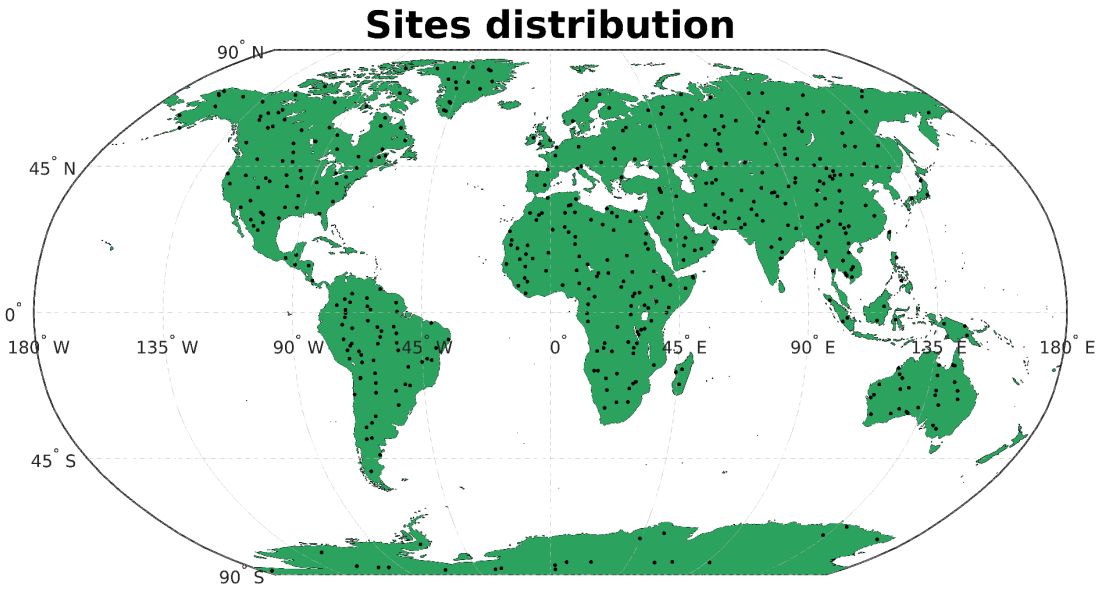

Figure 18: Distribution of the data points used for data training and threshold selection.

The second subset is for the application of the derived thresholds on AVHRR data. We selected pixels with an overpass difference of < 2 minutes between AVHRR (NOAA16-NOAA19) and MODIS Aqua for 169 equally distributed days between 2002 and 2015. This minimizes the possibility that cloud positions have changed due to the overpass time difference between the satellites. This subset contains ~13 million data points, distributed around the globe as shown in Figure 19.

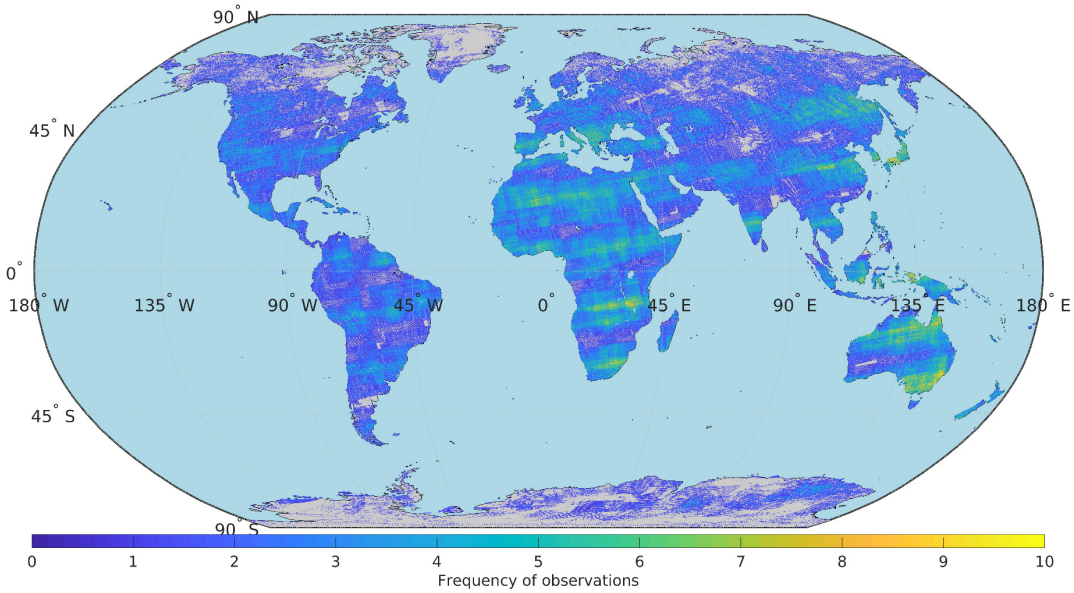

Figure 19: Frequency of the pixels used in the study with a < 2 minutes difference in time overpass between MODIS Aqua and NOAA, at CMG spatial resolution (0.05°), for 169 days distributed along the year from 2002-2015. No data is represented in gray.

3.2.3. Data preparation

Figure 20 shows a summary of the methodology employed in this paper. Once we have downloaded all of the data required, we proceed to prepare the data for analysis. The ultimate goal is to create thresholds that can classify clear, cloud and snow using MODIS data, and apply this model to AVHRR data. Since different sensors have different bandwidths and different Relative Spectral Response (RSR) functions, there are uncertainties associated with this process. In order to decrease these uncertainties, and to calculate thresholds that work for all sensors present in the record, we spectrally adjusted the MODIS data to AVHRR data (Note: We use the band notation following AVHRR sensor nomenclature, but we are using MODIS data here). In the optical bands, we followed the model derived in Villaescusa-Nadal et al. (Villaescusa-Nadal, Franch, Roger, *et al.*, 2019): we used a SBAF exponential model, dependent on the NDVI for the red band (Equation 27), and a multilinear model also dependent on the

NDVI for the Near Infrared (NIR) band (Equation 28). For the thermal bands, we used a linear model to adjust band 3B (Equation 29), and a SBAF exponential model, dependent on the temperature difference T4-T5 to adjust T4 and T5 (Equation 30).

$$\rho_{B1,ref} = \rho_{B1,tar} * \left(a \cdot e^{b \cdot NDVI} + c \cdot e^{d \cdot NDVI}\right) \quad (27)$$

$$\rho_{B2,ref} = a * \rho_{B1,tar} + b * \rho_{B2,tar} + c * NDVI + d * NDVI^2 \quad (28)$$

$$\rho_{3B,ref} = a + b * \rho_{B3B,tar} \quad (29)$$

$$\rho_{T4(T5),ref} = \rho_{T4(T5),tar} * \left(a \cdot e^{b \cdot (T4-T5)} + c \cdot e^{d \cdot (T4-T5)}\right) \quad (30)$$

Here, ρ_λ is the reference or target surface reflectance. The idea is to select a reference sensor (among all AVHRRs), which sets the common radiometric scale for all the target sensors. We used the parameters to obtain what they would have measured had they been designed with the same RSR function as the reference sensor. The choice of the reference sensor in this case is AVHRR/2 aboard NOAA14. However, this choice simply modifies the spectral adjustment parameters used. Table 12 shows the spectral adjustment parameters used in this study. Coefficients for all of the sensors used in the LTDR product and this paper can be found in Appendix A, Tables A1-A5.

Table 12: Spectral adjustment coefficients used to adjust MODIS Terra bands to NOAA-14's AVHRR/2 bands.

Band	Model Type	Parameter			
		a	b	c	d
1	SBAF exponential	0.98	5.78E-02	5.00E-03	5.4038
2	Multilinear	5.49E-02	0.94	1.20E-02	-1.35E-02
20	Linear	1.01	-1.03		
31	SBAF exponential	4.26E-04	-4.12	0.99	5.62E-04
32	SBAF exponential	1.04E-03	-2.56	0.99	-4.25E-04

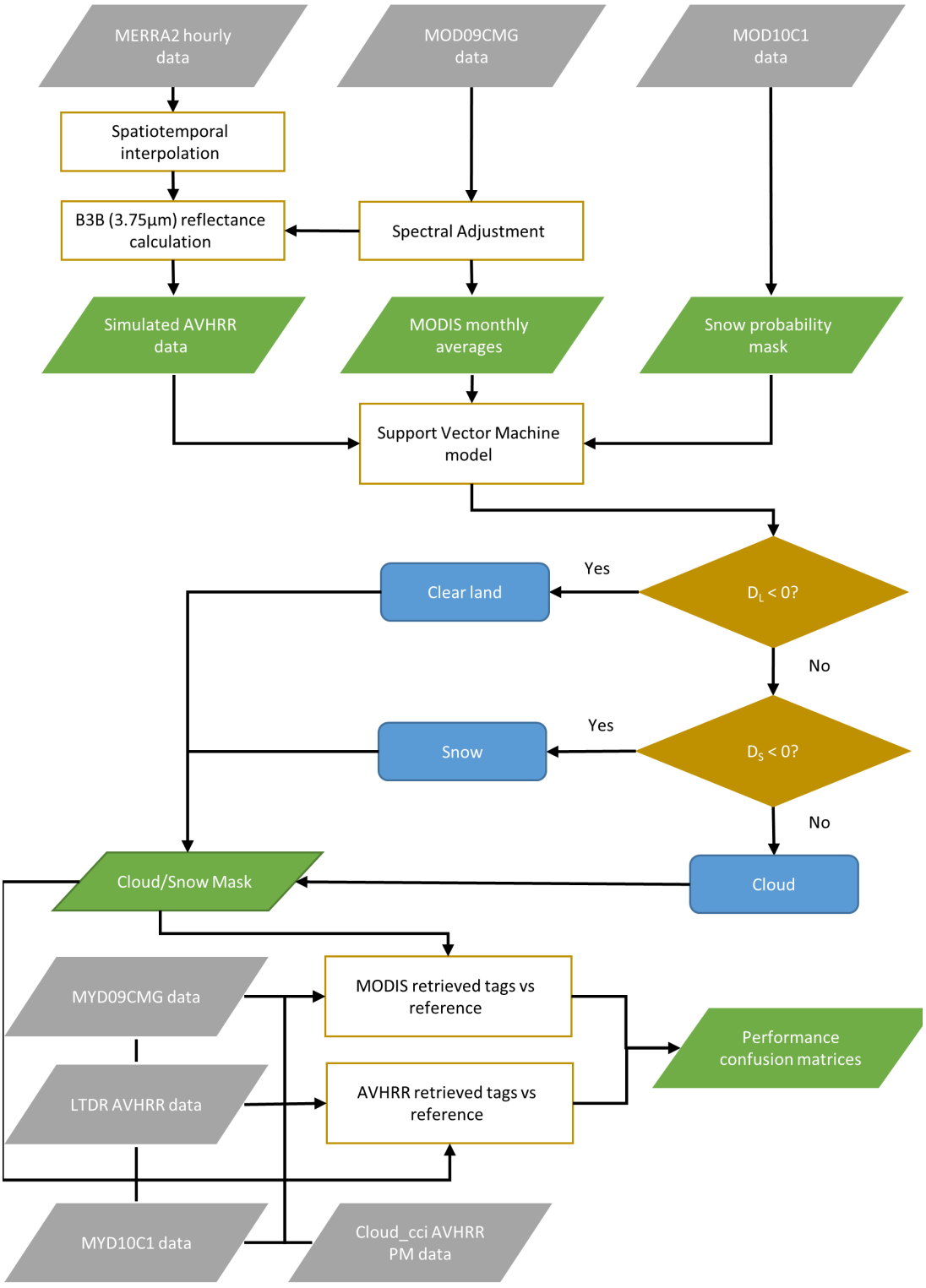

Figure 20: General workflow of the methodology employed in this paper. D_L and D_S are the distance to clear land pixels and distance to clear snow pixels, respectively, as defined in section 3.3.4.

The next step in the data preparation involves calculating the monthly MODIS average for all bands available. The goal of this step is to use a pixel's seasonality information to improve cloud detection. Typically, the reflectance of a pixel will vary throughout the year. If a clear land pixel is usually within a certain range of values (defined by the standard deviation) in the summer, when we measure a reflectance within those values in the same month, we can assume it will likely be clear too. If however, we measure a reflectance beyond that range, we can assume it is likely that the pixel is cloud or snow contaminated. The larger the difference between the measured value and the climatological average, the more likely it is that the pixel is cloud or snow contaminated. To obtain these climatological averages we calculated the average of every month for clear pixels, using MODIS Terra from 2000-2015, along with the standard deviation.

To determine the true land cover of a pixel to be used as a reference, we used the MOD10C1 product. This information can be combined with the spectral information to increase the probability of accurate detection. We also used this product to create a historical snow mask. It is often the case that clouds and snow can be misclassified. If for example we detected snow in equatorial latitudes, we can be almost completely sure that a cloud has been incorrectly tagged as snow. We can therefore count the cases of snow on different pixels for the whole time series (2000-2020) and assign to each one a probability of detecting snow. Figure 21 shows the snow probability map used in this paper. Pixels with zero counts are assigned a probability of snow cover of 0%, while pixels covered by snow all-year round are assigned a probability of 100%. MYD10C1 does not detect clouds in Antarctica, and considers it to be covered by snow

permanently, so the probability across the continent is homogenous. This value provides no indication about the cloud cover, but it allows us to minimize errors when detecting snow and clear land.

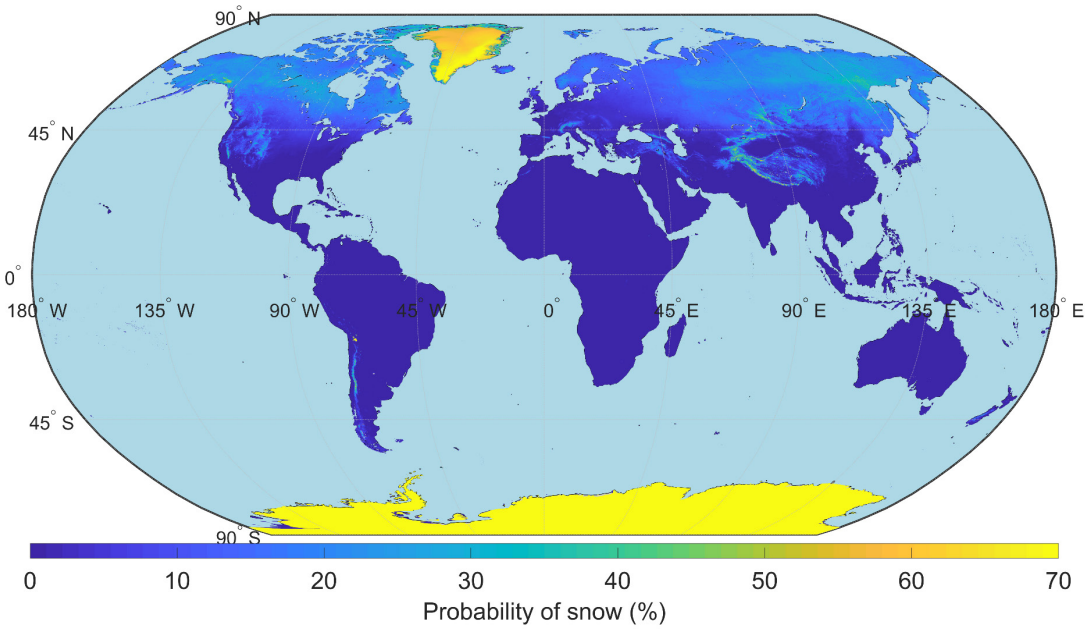

Figure 21: Probability of snow cover for every land pixel, obtained using MOD10C1 snow information. The probability per pixel is assigned considering the snow information from the products full time series. Antarctica has 100% probability of snow, but the color bar reaches a maximum of 70% for visualization purposes.

The final step towards data preparation is the calculation of the band T3B reflectance. The radiance obtained in this wavelength is a combination of both reflected and emitted components. Since the reflectance component is useful towards discriminating clouds and snow and for cloud detection (Dybbroe, Karlsson and Thoss, 2005b, 2005c; Khlopenkov and Trishchenko, 2007; Musial *et al.*, 2014), it is of interest for this study to obtain it. To do so, we used the algorithm derived by Roger and Vermote (1998), which estimates the reflectance by subtracting the thermal contribution from the total signal and dividing the remaining signal component by the atmospheric transmission

and solar irradiance (Roger and Vermote, 1998). This method requires the use of the water vapor, which in the case of MODIS data is available in the product. For AVHRR data, however, the only water vapor available is from 2000-onwards (which is derived from MODIS). For this reason, we used the MERRA-2 reanalysis water vapor, interpolated to AVHRR spatial and temporal resolution for dates before 2000. This method, along with similar methods employed in the literature for the retrieval of the reflectance, presents high uncertainties (> 10%) for low sun geometry. To avoid this, we removed from the dataset every pixel with a SZA > 75°. This also deals with issues discerning cloud at said angles of observation, but limits the amount of data available, especially over polar latitudes.

3.2.4. Model and feature selection

Once all the data is processed and harmonized, we can proceed to the creation of the models using the MODIS 'AVHRR-like' data. These models aim to separate clear land, cloud and snow classes, through the derivation of thresholds on selected features. The initial selection of these features is based on physical reasoning, similar to that presented in the introduction. Using this argumentation, we can narrow down all the inputs available in our study to those relevant to the discrimination of a certain class. After we have our initial selection, the final selection is done based on empirical results obtained after running several models with different band combinations: Bands that provide significant improvements are added, while those that provide no improvement or just a slight, non-significant improvement are not added or not included at all. The final features used are those that maximize the probability of detection and minimize

the false alarm rate. Ideally, the number of inputs is small and the accuracy is high, in order to maintain a reliable and robust model that can later be applied to the actual AVHRR data.

Two models are presented in this study. The first one is used to discriminate between clear land and cloud/snow pixels, while the second one is only applied to cloud/snow classified pixels and is used to separate both classes. The features used for each model are shown in Table 13 and Table 14. In the clear model, we make use of the MODIS climatology for the red band and for the NDVI, and of the variables T5 and T4-Ts. For the snow model, the climatological variables computed from MODIS did not prove to be valuable for the class separation, possibly due to the lower seasonality present on snow pixels, compared to vegetation pixels. For this reason, we used the information from the optical bands B1 and B2, along with the reflectance component of the B3B, and then used T4, T3-T5, T4-Ts and WV. In the case of the optical bands, this precise combination of bands matches the results obtained in (Trishchenko *et al.*, 2008b), which used B1, B2 and the reflectance B3B to simulate the B3A band (1.6 μm). In the case of the thermal bands, T4, T3-T5 and T4-Ts are commonly used in cloud/snow discrimination, while the combination of T4-T5 is typically used to detect cirrus clouds instead of the WV. In our case, we found that the use of the water vapor concentration provided a slightly better accuracy in the model, which is not surprising considering the dependence of T4-T5 on the water vapor concentration (Musial *et al.*, 2014).

Table 13: Variables used as inputs in the creation of the clear land Support Vector Machine model, along with their average and standard deviation.

Clear Land Model	x_1	x_2	x_3	x_4
Name	B1 clim.	NDVI clim.	T5	T4-Ts
Mean	0.22	0.17	276.20	-17.85
Std	0.26	0.22	24.80	20.13

Table 14: Same as table 4 but for the snow model.

Snow Model	x_1	x_2	x_3	x_4	x_5	x_6	x_7
Snow	B1	B2	B3B	T4	T3-T5	T4-Ts	WV
Mean	0.55	0.60	0.094	262.27	27.43	-29.49	1.07
Std	0.28	0.24	0.069	19.86	12.39	20.87	1.06

With these features, we created an n-dimensional hyperspace (where n is the number of variables in the model). In this hyperspace, we have two different clusters, grouped using what we consider in this study, the true information of the pixel from MOD10C1 data. In the first model, the two clusters are clear land and cloud/snow, whereas in the second model, they are cloud and snow. The idea is to find an n-dimensional plane that can separate these two clusters, so that the average distance of pixels within that class to the hyperplane is maximized. To do this, we make use of Support Vector Machines (SVM), a supervised machine-learning model that has been used widely in the literature for classification in remote sensing applications (Tzotsos and Argialas, 2008; Zhu and Woodcock, 2012; Taravat *et al.*, 2015).

We used this method as the main model for this study above other machine learning algorithms such as Neural Networks or Regression Trees for three reasons: Firstly, we wanted to use a more transparent method that allows us to understand the exact process happening in the training algorithm. Secondly, we wanted to use a model that allows users apply it to their data in an intuitively way. In this case, the output of the model is the Equation of a hyperplane, which users can apply to their own data. Finally, this approach allows us to compute the distance of each pixel to the hyperplane. If the distance is positive, the pixel belongs to one class, while if the distance is negative, it belongs to a different class. The higher or lower the distance value, the more likely the pixel is to belong to one class or another. In cloud detection, the decision of tagging something as cloudy or clear, for example, even when tagging it manually, is not a universal principle. This also might depend on the application, where perhaps a very restrictive cloud mask needs to be applied. Therefore, a continuous approach, as opposed to a branched approach, allows us to make arguments about the percentage cloud cover on a certain pixel or the thickness of the clouds present. Pixels with a distance to the hyperplane close to zero are more likely to be mixed pixels or thin clouds.

The process to obtain the distance to the hyperplane obtained using the SVM model is as follows: First, the variables are normalized by using the mean and standard deviation of the distributions. Then they are input to the SVM model, which yields the hyperplane's coefficients that provide optimal separation of the two classes. Equation 31 shows the Equation of a plane in three dimensions with variables (x_1, x_2, x_3).

$$\beta_1 x_1 + \beta_2 x_2 + \beta_3 x_3 + \beta_0 = 0 \tag{31}$$

If we define a random point with coordinates (x_0, y_0, z_0), we can then calculate the distance of a pixel to this plane as:

$$D = \frac{\beta_1 x_0 + \beta_2 y_0 + \beta_3 z_0 + \beta_0}{\sqrt{\left({\beta_1}^2 + {\beta_2}^2 + {\beta_3}^2\right)}} \tag{32}$$

Each pixel will therefore have two distance values associated with it, namely D_L for the distance to the clear land cluster and D_S for the distance to the snow cluster. If $D_L < 0$, the pixel is considered to be clear land. If $D_L > 0$, and $D_S < 0$, the pixel is considered to be clear snow. Finally, if both $D_L > 0$ and $D_S > 0$, then the pixel is tagged as cloudy. We applied these models first to MODIS Aqua data, to ensure that they perform as accurately for Aqua data as they do for Terra data. This also serves as a reference of what the maximum correction we can achieve with this model on AVHRR data is, compared to the correction we actually get. Secondly, we applied them to the AVHRR data we aim to correct and we compared the results of our classifications with the reference tags from MYD10C1. Finally, to compare our results to other cloud products obtained using AVHRR; we compare the MACSSA algorithm to the Cloud_cci AVHRR PM data. These data contain only cloud information, so for this comparison, we transform the resulting tags to two classes: cloud and no cloud. To obtain the latter we simply merge the snow and clear classes into one. We then also compare the

Cloud_cci AVHRR PM mask to the MODIS Aqua mask to analyze which of the two AVHRR models provides a better agreement with MODIS data.

In order to compare and analyze these results, a confusion matrix is often used. A confusion matrix shows the absolute values of the pixels correctly tagged in the diagonal, and the absolute values of incorrectly tagged pixels in the off diagonal. Table 15 shows a sample confusion matrix of $N = N_A+N_B+N_C+N_D$ total pixels, with MODIS tags on the rows (truth) and AVHRR tags on the columns (predictions). The rest of the rows and columns are used to indicate the percentage of hits and misses; the green shaded cells are typically known as the Probability of Detection (POD) of a certain class, while the yellow shaded cells are known as the False Alarm Rate (FAR) of a class. The Overall Accuracy (OA), which can be calculated as shown in the bottom-right of the table, indicates the effective hit rate of the model; the percentage of total pixels correctly tagged from the total amount.

Table 15: Sample confusion matrix to illustrate the errors involved with the models. Hits and misses are typically presented as a percentage.

Sample matrix	AVHRR clear	AVHRR cloud/snow	Hits	Misses
MODIS clear	N_A	N_B	$N_A/(N_A+N_B)$	$N_B/(N_A+N_B)$
MODIS cloud/snow	N_C	N_D	$N_D/(N_C+N_D)$	$N_C/(N_C+N_D)$
Hits	$N_A/(N_A+N_C)$	$N_D/(N_B+N_D)$	$OA = (N_A+N_D)/N$	
Misses	$N_C/(N_A+N_C)$	$N_B/(N_B+N_D)$		

3.3. Results

Table 16 shows the hyperplane parameters obtained from each model. Using these β values and the variable names from Table 13 and Table 14, one can express the Equation of the plane following Equation 5.

Table 16: Parameters of the hyperplane obtained for each model, as explained in Equation 5.

Model	β_0	β_1	β_2	β_3	β_4	β_5	β_6	β_7
Clear Land	1.04	3.29	0.76	-2.78	-2.17			
Snow	6.66	-0.44	-0.70	3.35	-1.19	-0.83	-3.09	0.58

Figure 23 shows a histogram of the distance D_L when the clear land model is applied to MODIS (top row) and when it is applied to AVHRR data (middle). The green and red bars represent those tagged as clear and cloud/snow by MYD10C1, respectively, while the black dotted line centered at $D_L = 0$, represents the threshold that separates the two classes. Therefore, any overlap between the two distributions represents the misclassifications and therefore, shows the quality of performance of the model. In the bottom row, we plot the confusion matrices of the resultant tags from the MACSSA algorithm compared to the reference tags from MYD10C1. These results show that when applying the model derived from MODIS Terra data to MODIS Aqua data, the accuracy of the classification is very high, as confirmed by the 99.3% overall accuracy, the 99.5% probability of distribution of clear pixels and the 1% false alarm rate. When applied on AVHRR, the accuracy is lower, yielding a 96.7% OA, a 97.1% POD_{clear} and a 4.4% FAR_{clear}. Figure 22 shows the confusion matrix of the mask currently used in the LTDR product, with a lower OA (95.04%), a lower POD_{clear} (93.2%) and a higher FAR_{clear} of 4.7%. This shows that the proposed model yields a significant improvement especially in the POD_{clear} from the current model used in this product. Transforming

the results from the SPARC algorithm (Khlopenkov and Trishchenko, 2007) into similar classes, we observe that they report an OA of around 94%, when comparing with a multispectral maximum likelihood classifier (MLC), but a POD_{clear} of around 80%. These results are similar to the comparison of the PCM algorithm (Musial *et al.*, 2014) with a CASLIPSO/CALIOP LIDAR mask (Karlsson and Dybbroe, 2010), which yield around 80% OA and 85% POD_{clear}, but a high FAR_{clear} of almost 40% using NOAA 18.

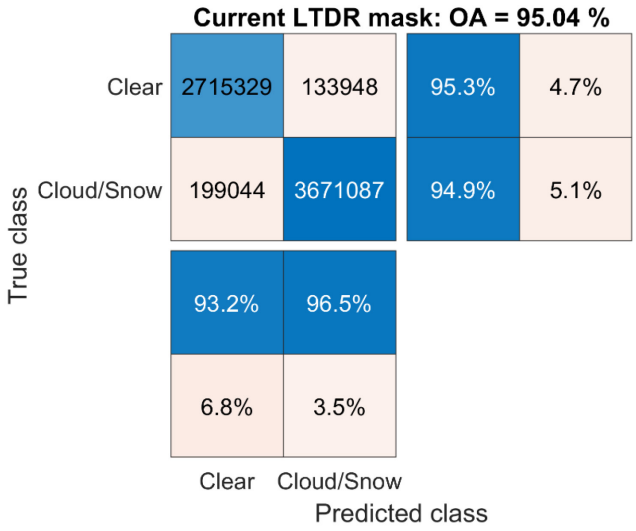

Figure 22: Confusion matrix of the current LTDR AVHRR approach using only Band 1 climatology.

Figure 24 shows an analogous figure to Figure 23 but for D_S (snow and cloud discrimination). The blue bars represent snow, while the red bars represent clouds. Here, the difference between the model applied to MODIS Aqua data, and to AVHRR data is similar; the PODsnow is 90% for the former, and 86% for the latter. The FARsnow are, however, quite similar, with only around 2% difference (8.2% vs 9.9%). The current model used for this product has no snow detection, so we cannot compare our results with it. In the case of the PCM algorithm, they retrieve, without the use of

band 3A, a PODsnow of around 45%, with a FARsnow of around 10%. The SPARC algorithm shows a much better performance with a PODsnow of around 98%, but a FARsnow of 13%, when comparing their model to a maximum likelihood classification using AVHRR, and using band 3A.

When including cloud edges, which are reported in the MODIS cloud mask, into the algorithm, the results yield around 2% less in OA and PODclear, and around 2% higher FARclear. They mostly translate into more pixels having a D_L close to zero that increase the misclassification. In the case of the snow detection, however, the effect of the cloud edges lowers the PODsnow to around 73%. For this reason, we did not consider the cloud edges in this model. Potentially, they should be masked as such, and disregarded for the final data depending on the user's potential use and application.

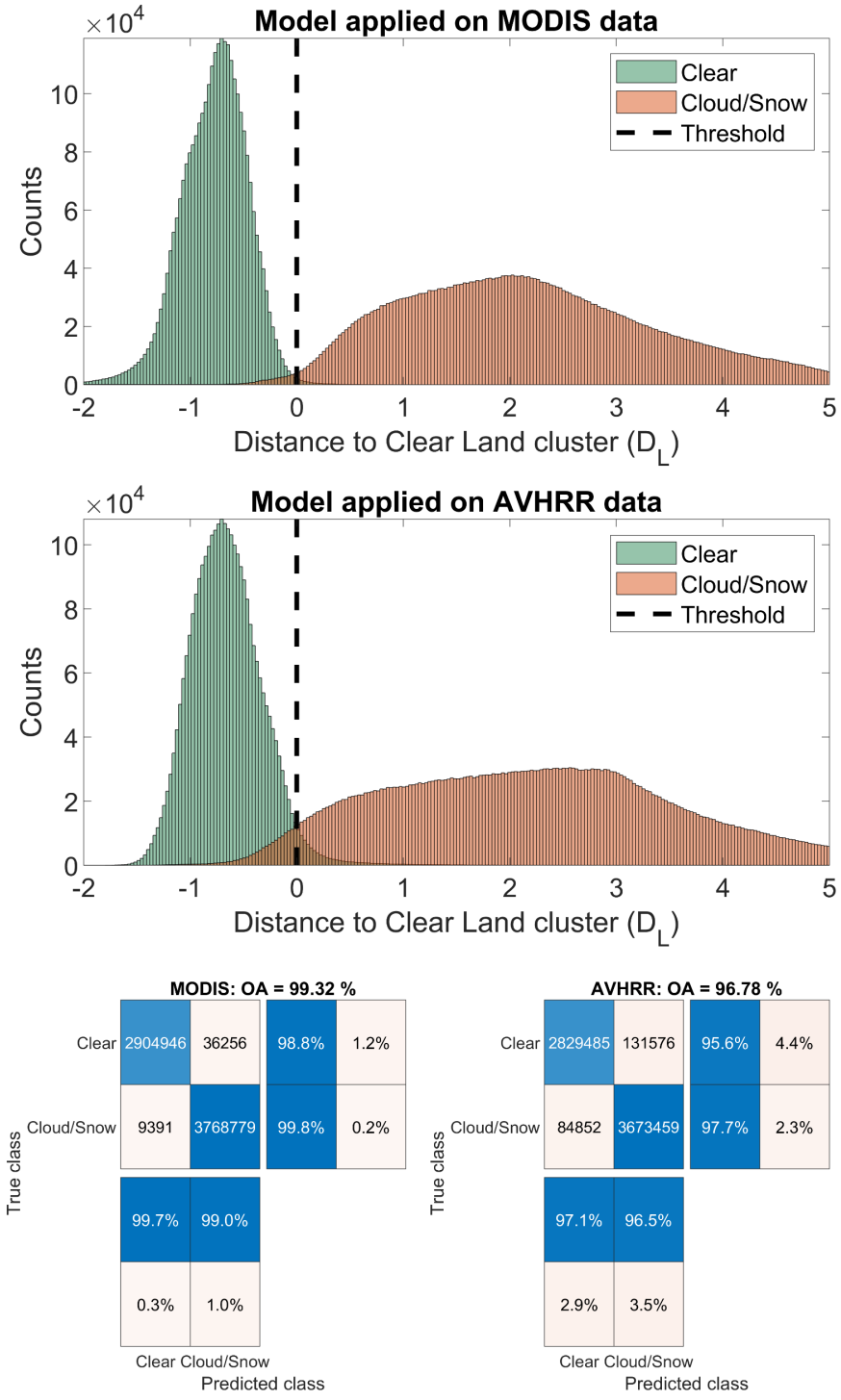

Figure 23: In the top, we show a histogram of the distance to the clear land cluster of MODIS pixels. Green and red bars are those tagged as clear and cloud/snow by MYD10C1, respectively. The black dotted line represents the line that separates clear and cloud/snow according to our model. In the middle, we show the same, but using AVHRR data. In the bottom, we show their confusion matrices. Clear pixels represent land pixels that are not cloudy nor snowy.

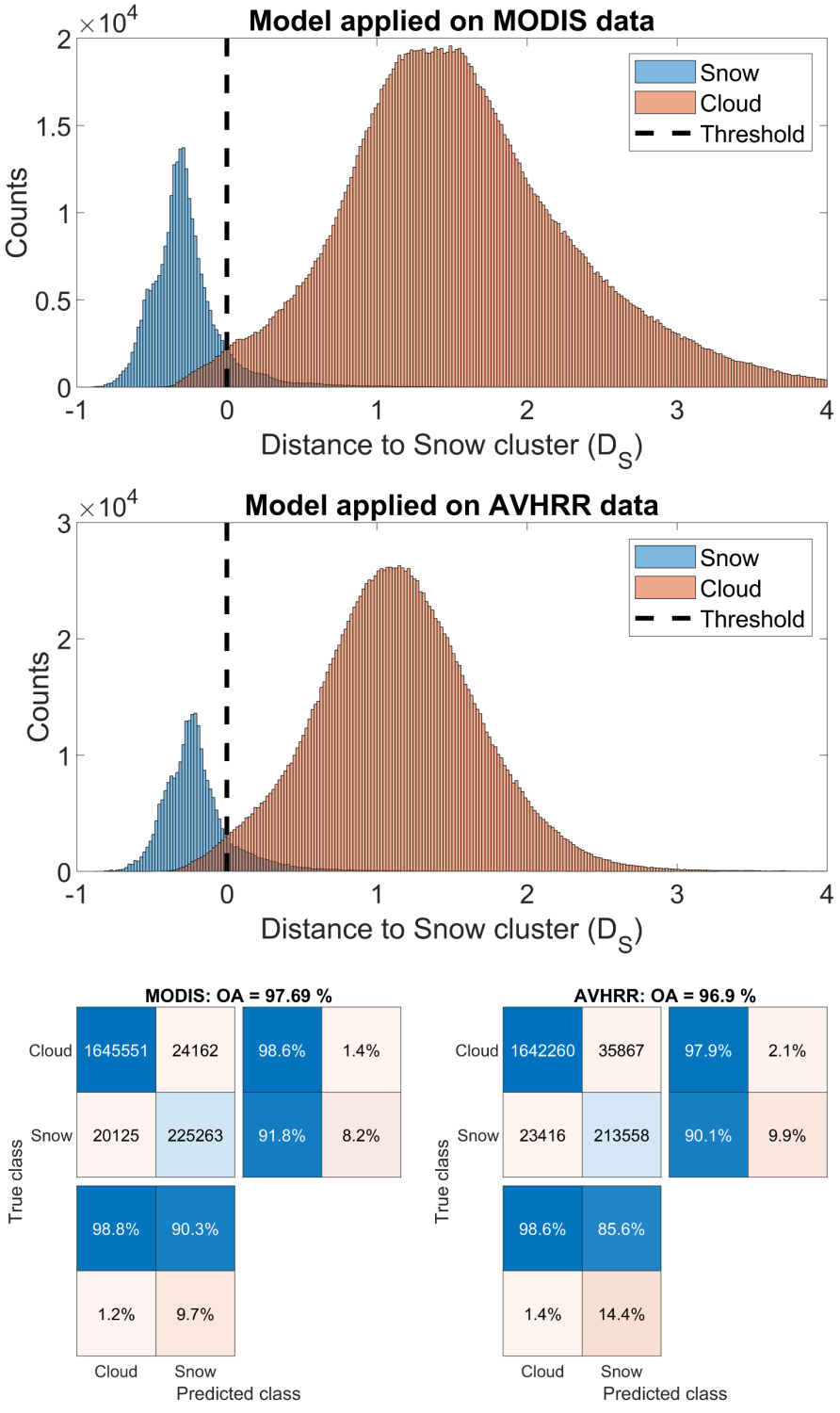

Figure 24: Analogous to Figure 23 but for the snow cluster. In this case, the blue bars represent snow, while the red bars represent clouds.

Figure 25 shows the final confusion matrices for the three classes using MODIS Aqua (left) and AVHRR (right) data. These results show that this model can accurately discriminate between the three classes using AVHRR data with a 96% OA, and probabilities of detection of 97%, 96% and 88% for clear land, cloud and snow pixels. The detection of clear and cloud pixels is of high quality, while the snow detection, as anticipated, presents confusion when discerning cloud and snow (FAR_{snow} = 12.7%). The application of the model in MODIS Aqua data shows exceptional results overall (OA = 98.8%), with the mentioned errors in cloud and snow discrimination. This is not surprising considering that the model was derived using MODIS Terra data, and MODIS Aqua data are almost identical.

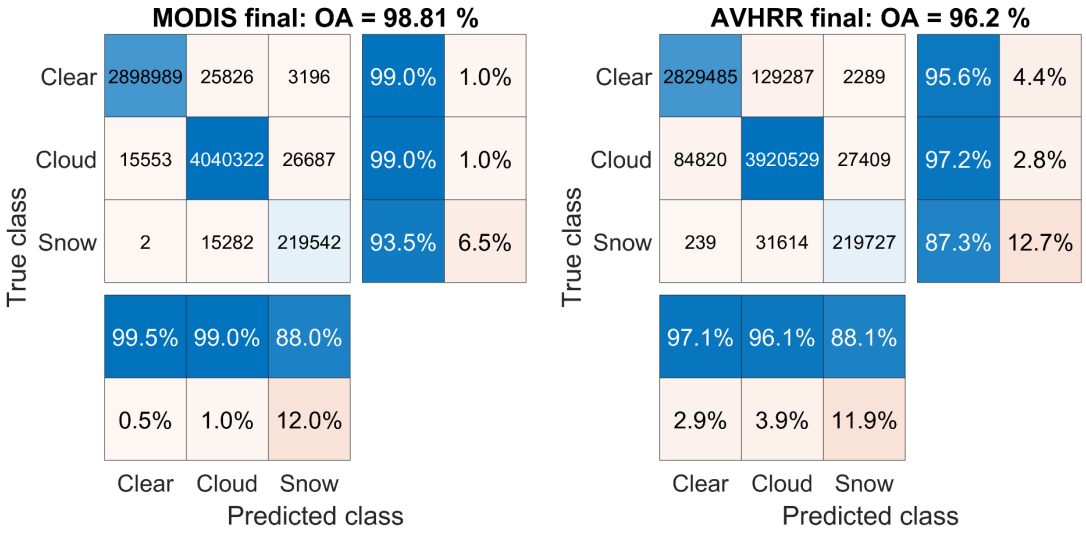

Figure 25: Total confusion matrices of the models applied on MODIS Aqua (left) and AVHRR (right). Clear pixels mean clear land pixels. The Overall Accuracy is shown in the title.

Figure 26 shows the confusion matrices of the combinations between MACSSA, MODIS Aqua and Cloud_cci AVHRR for the Cloud and No Cloud classes. The results show that the agreement between MACSSA and MODIS Aqua (OA = 94.6%) is

slightly better than the agreement between Cloud_cci AVHRR and MODIS Aqua (OA = 93.6%), with around 2% lower $FAR_{Nocloud}$ and a slightly higher overall accuracy. While the performances of both models compared to MODIS Aqua are similar, the actual difference between both AVHRR products is noteworthy. The overall agreement between them is of ~93%, with significant differences in the No Cloud class detection.

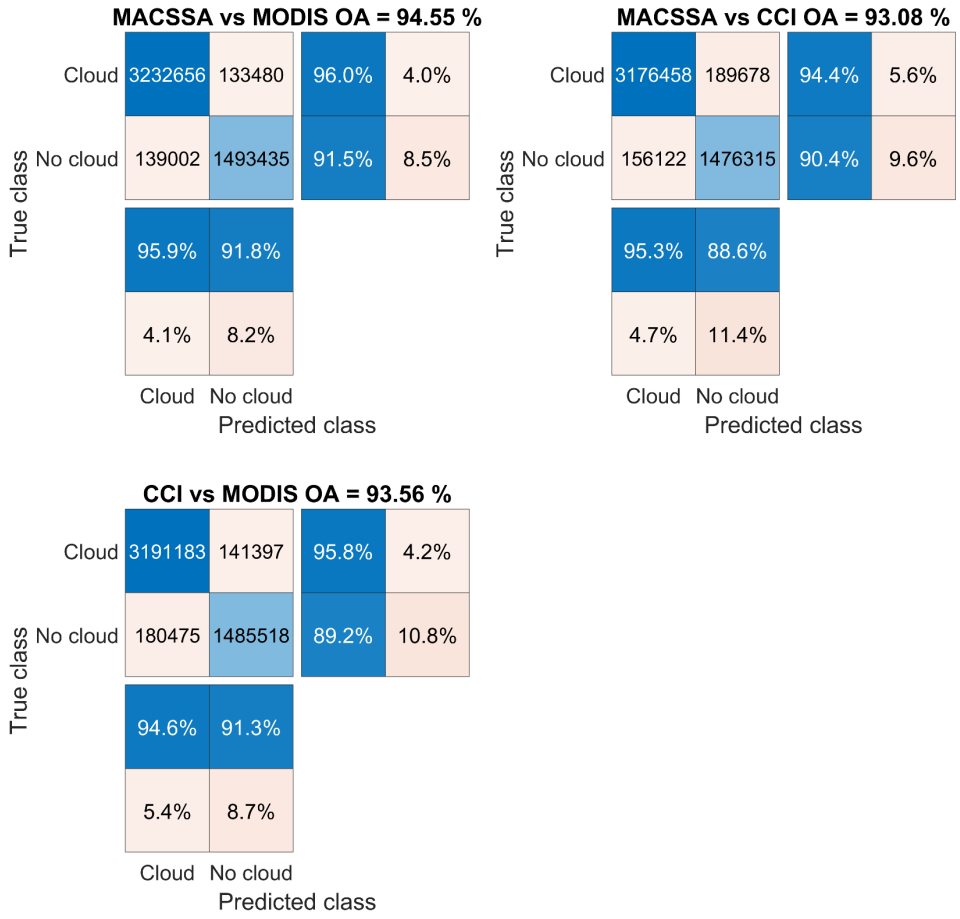

Figure 26: Confusion matrices of the MACSSA model compared to the MODIS Aqua (top left), for cloud vs no cloud, the MACSSA vs the Cloud_cci AVHRR (top right), and the Cloud_cci AVHRR vs MODIS Aqua (bottom left).

Following the analysis of the overall performance of the model compared to our reference, we proceed to analyze the behavior of the algorithm both spatially and temporally.

First, we applied this model on global images obtained from the LTDR product to grasp the spatial behavior of the algorithm. Figure 27 shows tags obtained using the model described in this paper for a N16 image acquired on February 15 of 2004 (top) and the magnitude Ts-T4 for the same date (bottom). We chose to show Ts-T4 along with the tags, so that we can visually verify the correct behavior of the algorithm when tagging clouds (higher difference means higher chance of cloud detection). Land pixels with no data or faulty information are shown in gray. Clouds are not shown in the water, because the MACSSA algorithm is intended over land pixels only. These results show that, firstly, the snow is detected in places where snow is expected, such as northern latitudes and Antarctica, or in mountain ridges such as the Rocky Mountains, the Himalayas or the Alps. Secondly, the detection of clear land pixels is, as predicted, of good quality, and the patterns of clouds in both images are identifiably similar. Even though it cannot be easily noticed from a global image, the product presents some issues when detecting coastlines, where they are misclassified as cloud, instead of clear land.

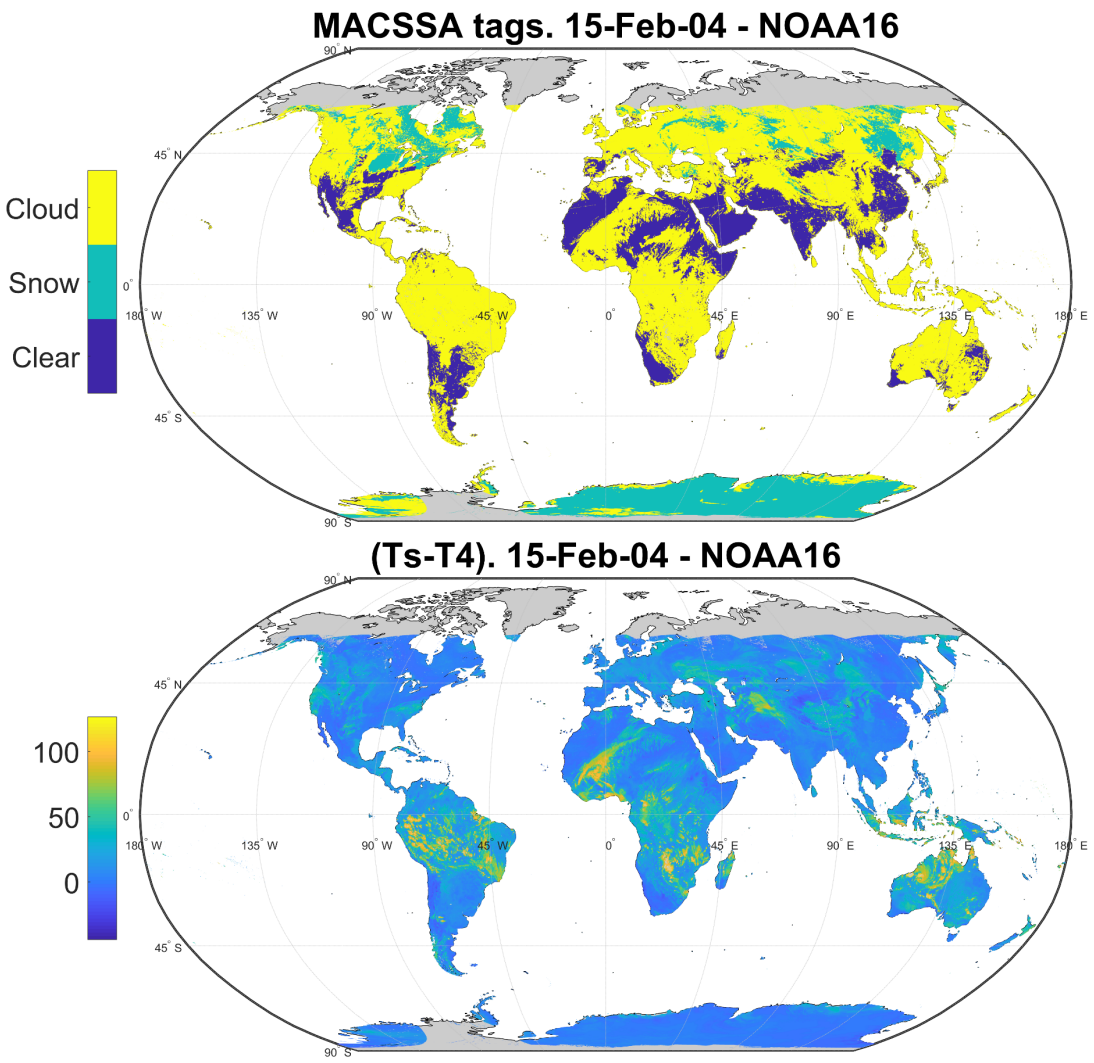

Figure 27: Tags obtained using the model described in this paper for a N16 image acquired on February 15 of 2004 (top) and the magnitude Ts-T4 for the same date (bottom). Land pixels with no data are shown in gray. Clouds are not shown in the water, because the algorithm used in this paper is intended over land pixels only.

Second, we applied the model to two pixels for the whole LTDR dataset, to analyze the temporal behavior of the model, and its consistency over the different sensors. Figure 28 shows the distance to the land cluster D_L of a pixel of open shrublands in Argentina (-38.65,-67.05) and the distance to the snow cluster (D_S) of a snow pixel in Greenland (70.95,-46.05) for the whole time series (1982-2019). The results show that firstly, both

D_L and D_S exhibit seasonality in their value. This is expected, given the nature of the algorithm, which is formed by bands whose values vary throughout the year. In the case of the snow pixel, during winter the D_S is lowest, suggesting a higher confidence in the determination of snow over cloud. Secondly, the results show a consistent behavior over the different NOAA satellites used, which are displayed using different colors.

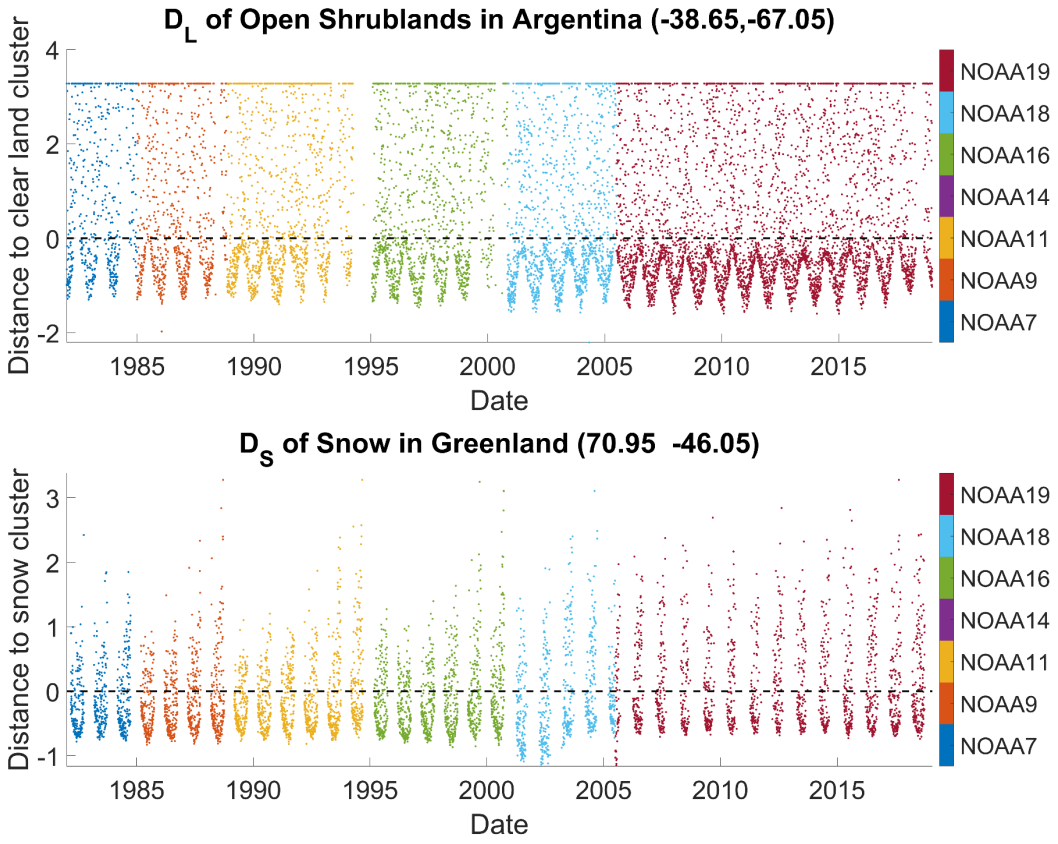

Figure 28: Distance to the land cluster D_L of a pixel of open shrublands in Argentina (-38.65,-67.05) and the distance to the snow cluster (D_S) of a snow pixel in Greenland (70.95,-46.05) for the whole time series (1982-2019).

3.4. Discussion

The MACSSA approach used in this paper was developed using pixels distributed around the world, covering a wide range of land covers, observation and atmospheric

conditions as an input. The tags retrieved were then compared against reference tags covering, as Figure 19 shows, almost every pixel around the world and obtaining reliable results. This serves as an indication of the overall robust performance of the model over different observation and atmospheric conditions, which can therefore be applied to the LTDR product to detect clear land and snow pixels to a good degree of accuracy and with a relatively simple and computationally cheap method.

Regarding the use of climatological information, we found it to be particularly useful for detecting clear land pixels, since the vegetation phenology is well captured on the monthly averages calculated. For the case of snow detection, however, climatological information provided no extra information compared to using the optical and thermal bands directly. The use of a priori information (probability of snow cover) aided in reducing the number of misclassifications, especially on pixels with a lot of cloud cover such as equatorial latitudes. Similarly, ancillary information derived from Merra-2 was useful for both clear land and snow detection. Nonetheless, limitations with these kind of approaches arise when trying to use the model for prediction outside of the climatological time range used. The average values do not consider land cover changes and trends, very likely present in such a long time series, which would translate in increased inaccuracies in the pre-MODIS era (1982-2000). While this effect could be very pronounced when dealing with snow detection, due to a receding snow trend in northern latitudes, in clear land pixels the effects are mitigated. Clear land pixels combine climatological information with instantaneous multispectral data, limiting the amount of influence the trend component can have on the performance of the model.

When applying the models derived using MODIS data to AVHRR data, the performance of the product on the latter was ~2% less accurate in both models, despite our efforts to minimize these errors. This difference in performance can be attributed to calibration issues between the sensors. The individual bands were analyzed and presented very small and acceptable differences between them for coincident pixels. However, there was significant error in the computation of T3-T5, which persisted even after the spectral adjustment. This might be due to the known issues in the calibration of thermal AVHRR bands (Trishchenko, 2002; He *et al.*, 2016). Finally, since both satellites have different observation angles, it is entirely possible that for some coincident pixels the MODIS satellite was observing a clear or snow pixel, while the NOAA satellite was observing a cloud, or vice versa. These small differences can add up to a significant variation in performance between the two sensors.

Even so, it is important to note that in the development of this model we considered the tags provided by MYD10C1 to be the truth, and developed the model around it. The amount to which this product can be considered the truth depends on its validation with real measurements. The MOD10C1 product, which is used to derive the model parameters, has a 93% agreement with different ground measurements and satellite observations. This is sufficiently high for our applications, especially considering that the MOD10C1 product provides percentage clear, snow and cloud cover (Hall *et al.*, 2002). Only when a thin layer of snow is present, does the product provide significant errors. In the case of MYD10C1, band 6 ($1.6\mu m$) of MODIS Aqua has non-functioning detectors, so they use band 7 ($2.1\mu m$) instead. The results for cloud detection are almost identical to MODIS Terra, however Hall and Riggs (2007) (Hall *et al.*, 2002) report

subtle differences in the snow detection over dense forests. For the sake of our application, however, we consider these differences negligible, considering the limitations the AVHRR sensor has on discerning cloud and snow, and the potential errors provided by changes in spatial resolution when comparing instead with ground data or higher resolution products.

The comparison of the MACSSA approach to another AVHRR derived cloud mask, shows that, while using data corrected using different algorithms, and significantly different cloud retrieval approaches, both products compare similarly to the selected reference MODIS Aqua data. The direct comparison between both AVHRR products, however, show that they are not so similar between them. Since the probability of detection of the No Cloud class is below 90%, it is likely these differences occur mostly in the snow detection and cloud/snow discrimination. The better performance with MODIS of the MACSSA approach is expected, considering the nature of the model, however, this comes at a price. In this study, we can only detect three classes: Clear land, cloud and snow. Arguably, it can be said that we only detect two classes, and that the cloud class combines everything that does not fit on the first two, which includes mostly clouds. Other algorithms using AVHRR data, however, are able to distinguish between cirrus, cirrus over snow, sea ice, thin cloud and thick cloud [29], are more physically based, and therefore allow an easier physical interpretation of the model [35], or have the ability to detect clouds and snow at night [31].

While the temporal analysis indicates that the performance of the algorithm is consistent throughout the decades that the LTDR product spans, it also suggests quite visibly how the performance of a seasonal threshold could benefit the model and

improve the results. This is especially true in the D_L, where its calculation already involves some kind of seasonal threshold through the use of the monthly climatological data.

Other limitations of this product include its performance over cloud edges and coastlines, which present problems in the current version of the algorithm. The recommended approach for cloud edges depends on the application. For a restrictive cloud mask, tagging cloud edges as clouds is desirable, to ensure high quality of the land pixels, at the cost of fewer observations. This cost is a small price to pay given the more than 38 years of observations available in this product. For a more permissive cloud edge masking approach, the use of the distance to the hyperplane serves as an indication of the amount of cloud contamination in a pixel. The use of the MOD09 product for the computation of the climatological clear land mask is very useful for cloud detection, but could present inaccuracies in dates before the appearance of MODIS (2000). The higher the slope of the trend of a certain pixel, the less likely it is that the average from 2000-2015 represents the value of a pixel from 1982, and the higher the uncertainty involved in the process. This would effectively result in a change on the β_0 parameter of the hyperplanes derived, which can be modified and adjusted to the actual sensor of use.

Despite the limitations mentioned, the results show a clear improvement from the current LTDR product version. Firstly, there is an improved performance of the clear land pixels detection, making use of more AVHRR bands. Secondly, there is an inclusion of the cloud/snow discrimination algorithm, which was previously not considered. Finally, every pixel is assigned a value of the distance to the hyperplane

that separates the classes, which can potentially be associated to the thickness of the cloud cover, or serve as an indication of the percentage of mixed features within a pixel. Future versions of MACSSA algorithm will focus on the derivation of cloud shadow, for which a combination of a geometric and climatological approach shows promise. To exploit the nature of this algorithm fully, a formal association of the distance to the percentage of cloud cover or the thickness of a cloud can be done using the same MYD10C1 product as truth, since it provides cloud percentage information. To solve specific problems such as the misclassification of clouds over coastlines, targeted solutions can be achieved using a posteriori information, so that the rest of the pixels around the globe are not affected by model modifications. The model could also be applied a third time to create a separation of clusters within the cloud cluster, that could detect cirrus or thin clouds over thicker clouds. Finally, another improvement could be to add a seasonal and trend component to the thresholds derived. The former could be applied by obtaining a different model for every month, with different hyperplane parameters, while the latter could be applied by calculating the trend component of every pixel and applying a linear correction to the seasonal thresholds derived.

3.5. Conclusions

In this paper, we propose the MODIS-based AVHRR Class Separation Algorithm (MACSSA), whose goal is to identify clear land and snow pixels using AVHRR data. The MACSSA algorithm was designed to be applied over the LTDR product, at 0.05° spatial resolution, which covers different NOAA satellites from 1982-2020. The algorithm uses data from the MOD09 product, which are spectrally adjusted to look like analogous to AVHRR bands. To complete the limited information that using only

analogous bands to AVHRR provides we download the skin temperature from MERRA-2 reanalysis data. After data homogenization, the data was used as input for first, a Support Vector Machine (SVM) model that discriminates clear land pixels from clouds and snow, and second, using only those previously tagged as clouds and snow, a SVM model to discriminate between them. We used clear, cloud and snow percentage information from the MOD10C1 product to determine the reference land cover. These models were then applied to AVHRR data over pixels with less than 2 minutes overpass time difference between MODIS Aqua and NOAA16-19. We analyzed the results over pixels all around the world and over individual images, and found the product to be very accurate in identifying clear land pixels, with a POD_{clear} of 97%. The discrimination of snow and clouds is of less quality, with a POD_{snow} of 88%, however, considering the limited tools available in the AVHRR sensor to do this, the results are encouraging and reliable for application on daily images from the LTDR product.

The first version of the MACSSA approach used in this paper comes with limitations on the amount of classes detected, misclassifications of coastlines and especially on the detection of cloud edges. Nonetheless, future versions will aim to tackle these issues in order to provide a model that can discriminate a larger number of classes, especially within cloud types. It will also aim to provide a reliable direct association between distance to the hyperplanes dividing the classes and cloud fraction percentage of a certain pixel, and the incorporation of a cloud shadow detection. However, these limitations are acceptable in the broader scope of this paper, which aims to obtain cloud and snow information for the development of a global surface albedo dataset using the LTDR product, where a very restrictive cloud mask is required and the information on

different cloud types is not of great significance. This is also the case for other applications needing land pixels of the upmost quality, where the masking of clouds is essential to increase the accuracy of the results.

Chapter 4: Land and Snow Albedo Computation

The contents of this chapter are divided in two sections. Since different methods are used for land and snow albedo retrieval, the first section will focus on modelling the BRDF shape for AVHRR data to calculate the land surface albedo, while the second section will focus on calculating snow albedo.

The contents of the first section have been published in (Villaescusa-Nadal, Franch, Vermote, *et al.*, 2019)

4.1. Land surface albedo computation

4.1.1. Abstract

The Long Term Data Record (LTDR) project has the goal of developing a quality and consistent surface reflectance product from coarse resolution optical sensors. This paper focuses on the AVHRR part of the record, using the MODIS instrument as a reference. When a surface reflectance time-series is acquired from satellites with variable observation geometry, the directional variation generates an apparent noise, which can be corrected by modeling the bidirectional reflectance distribution function (BRDF). The VJB method estimates a target's BRDF shape using 5 years of observations and corrects for directional effects maintaining the high temporal resolution of the measurement through the use of the instantaneous NDVI. The method was originally established on MODIS data but its viability and optimization for AVHRR data has not been fully explored. In this study, we analyze different approaches to find the most robust way of applying the VJB correction to AVHRR data, considering that high noise in the red band (B1) caused by atmospheric effect

makes the VJB method unstable. Firstly, our results show that for coarse spatial resolution, where the vegetation dynamics of the target do not change significantly, deriving BRDF parameters from 15+ years of observations reduces the average noise by up to 7% in the NIR band and 6% in the NDVI, in comparison to using 3-year windows. Secondly, we find that the VJB method can be modified for AVHRR data to improve the robustness of the correction parameters and decrease the noise by an extra 8% and 9% in the red and NIR bands with respect to using the classical VJB inversion. We do this by using the Stable method, which obtains the volumetric BRDF parameter (V) based on its NDVI dependency, and then obtains the geometric BRDF parameter (R) through the inversion of just one parameter.

4.1.2. Introduction

The Advanced Very High Resolution Radiometer (AVHRR) sensor provides a unique global remote sensing dataset that ranges from the 1980s to the present. Among the different products delivered from this sensor, NASA is currently funding the Long Term Data Record (LTDR) project (Vermote and Claverie, 2013) to develop a quality and consistent Climate Data Record (CDR) of AVHRR data with the use of the Moderate Resolution Imaging Spectrometer (MODIS) instrument as a reference. This data record creates daily global surface reflectance products with a geographic projection at coarse spatial resolution (0.05°). The utility of this long time series has been demonstrated in the literature for a large number of applications such as agriculture (Franch *et al.*, 2016a), burned area mapping (Moreno Ruiz *et al.*, 2012), LAI and FAPAR retrieval (Verger *et al.*, 2012; Claverie *et al.*, 2016), snow cover

estimation (Wang *et al.*, 2017), global vegetation monitoring (Julien and Sobrino, 2011), and surface albedo estimation products (Saunders, 1990; Hu *et al.*, 2000; Strugnell, Lucht and Schaaf, 2001; Trishchenko *et al.*, 2008a).

Long-term consistent data records are becoming crucial to provide improved detection, attribution and prediction of global climate and environmental changes, as well as helping decision makers respond and adapt to climate change and other variability in advance (Schulz *et al.*, 2008; Hollmann *et al.*, 2013; Bates *et al.*, 2015). In particular, the knowledge of surface albedo is of critical importance to monitor land surface processes and plays an important role in energy-budget considerations within climate and weather-prediction models. For this reason, it has been listed as an Essential Climate Variable by the GCOS (Hollmann *et al.*, 2013; Bojinski *et al.*, 2014). Surface albedo can be derived from satellite data. The most common procedure consists on integrating a BRDF angular model, which can explain the reflectance's anisotropic behavior on different types of surfaces to obtain the black-sky (direct beam) and white-sky (completely diffuse) narrowband albedo. One can then perform narrow-to-broadband conversions to obtain the respective broadband albedos (Qu *et al.*, 2015) and obtain the actual (blue-sky) albedo by doing a weighted average, using the fraction of diffuse skylight (Schaaf *et al.*, 2002a).

For this product to be of highest quality, it is critical that the surface reflectance data record has minimal uncertainties in the calibration, geo-location, spectral correction, cloud masking, atmospheric correction and directional effects correction. Issues regarding calibration, cloud masking and atmospheric correction in the AVHRR data have been accurately corrected, after the year 2000, when MODIS data were used as a

reference (Franch *et al.*, 2016a). However, some issues persist for data before this year (1982-2000), such as aerosol and water vapor correction and calibration (Vermote and Claverie, 2013). These errors propagate resulting in surface reflectance time-series with high noise. This is especially true in the red band, where the atmospheric errors are higher, compared to the Near Infrared (NIR) band. Therefore, the BRDF parameters derived from these time series have high uncertainties and might not provide an accurate correction of the directional effects.

To address this issue, the LTDR product uses MODIS retrieved parameters using the VJB method (Vermote, Justice and Breon, 2009b; Franch *et al.*, 2018), and then applies them to AVHRR data. The VJB method uses a pixel's time series (typically 5 years) to compute BRDF parameters (V, R) in a daily manner with the use of the instantaneous NDVI. These parameters can later be used to correct the database. This method is based on the assumptions that 1) the target reflectance changes during the year but BRDF shape variations are limited and 2) the difference in surface reflectance between successive acquisitions is mostly explained by directional effects.

Assumption 1 holds true while retrieving the correction parameters with short enough periods, or in other words, if the surface does not change significantly over this period. When dealing with AVHRR data, due to the lower number of high quality observations, a larger number of years is required to make the computation of the BRDF parameters reliable, in which the surface is subject to change. One could argue, however, that because the product is at 0.05° spatial resolution, the stability of the pixel through the years is more likely to be maintained. Assumption 2 holds true for MODIS data because the evolution of the view zenith angle during the year is not gradual, so the difference

between successive observations is high, and atmospheric errors are low. This means that the time series have high directional effects, which are higher than the atmospheric correction errors. This is not the case for AVHRR data; the difference of view zenith angle between successive observations is low and atmospheric errors are high, especially for the red band. These facts could justify the use of MODIS parameters to correct AVHRR data; however, these also experience propagated uncertainties that can arise from the surface reflectance differences between them, caused by the different spectral response of the two sensors or calibration issues of AVHRR.

In this chapter, we explore different approaches to the AVHRR directional effects correction using the VJB method, to optimize it to AVHRR data. Firstly, we find relationships between BRDF correction parameters using different bands and band combinations derived from MODIS data, to attempt to minimize the propagation of atmospheric errors to the correction of directional effects. Secondly, we calculate said parameters using 3 years and the whole time series (15+ years). In order to test the best method, we compare the noise of the normalized surface reflectance to check which one shows the lowest noise in the time series. Section 4.1.3 describes the materials used for the study and the methodology employed. Section 4.1.4 presents the results. Section 4.1.5 presents a discussion of the results and section 4.1.6 presents the conclusion.

4.1.3. Materials

For this study we downloaded MODIS data from the MOD09 product (Vermote and Vermeulen, no date; Vermote, 2015) from 2000- 2015 and AVHRR from the LTDR product (Vermote and Claverie, 2013). We divided the data into AVHRR-pre MODIS

(1982-2000) and AVHRR (2000-2015). These data contain surface reflectance at CMG spatial resolution (0.05°). We use the red and NIR surface reflectance bands, as well as the view zenith (θv), solar zenith (θs), and relative azimuth (ϕ) angles, selecting pixels of the highest quality. We extracted the data for 445 BELMANIP2 sites. BELMANIP2 sites are an update of BELMANIP1 (Baret *et al.*, 2006a) and were selected due to their representativeness and variability of vegetation types and climatological conditions around the world. The product includes no spectral adjustment method, which is necessary considering that the time series is composed of data from several different NOAA satellites. Moreover, an accurate intercomparison with MODIS requires that all data be on the same radiometric scale. For this reason, we perform spectral adjustment using methods from (J. L. Villaescusa-Nadal, Franch, Roger, *et al.*, 2019), selecting NOAA14 as a reference.

4.1.4. Methods

An outline of the methodology is shown in Figure 29. We first use MODIS data to obtain relationships between the BRDF parameters, so we can use them to build different models with AVHRR data. They are then applied to MODIS and AVHRR data, using parameters derived every 3 years, and for the full time series. With these, we derive BRDF correction parameters, which are used to calculate the normalized time series using Equation 9. Finally, given the lack of BRDF field measurements that can be used as a reference to evaluate the best method; we derive the noise of the time series before correction and after the model inversions. This allows us to compare the noise improvement depending on the different BRDF model inversion used, and the

number of years employed. The noise is calculated using the statistical difference between the center measurement of three successive triplets and the linear interpolation between the two extremes (Vermote, Justice and Breon, 2009b):

$$Noise(y) = \sqrt{\frac{\sum_{i=1}^{n-2}\left(y_{i+1} - \frac{y_{i+2} - y_i}{day_{i+2} - day_i}(day_{i+1} - day_i) - y_i\right)^2}{N-2}} \qquad (33)$$

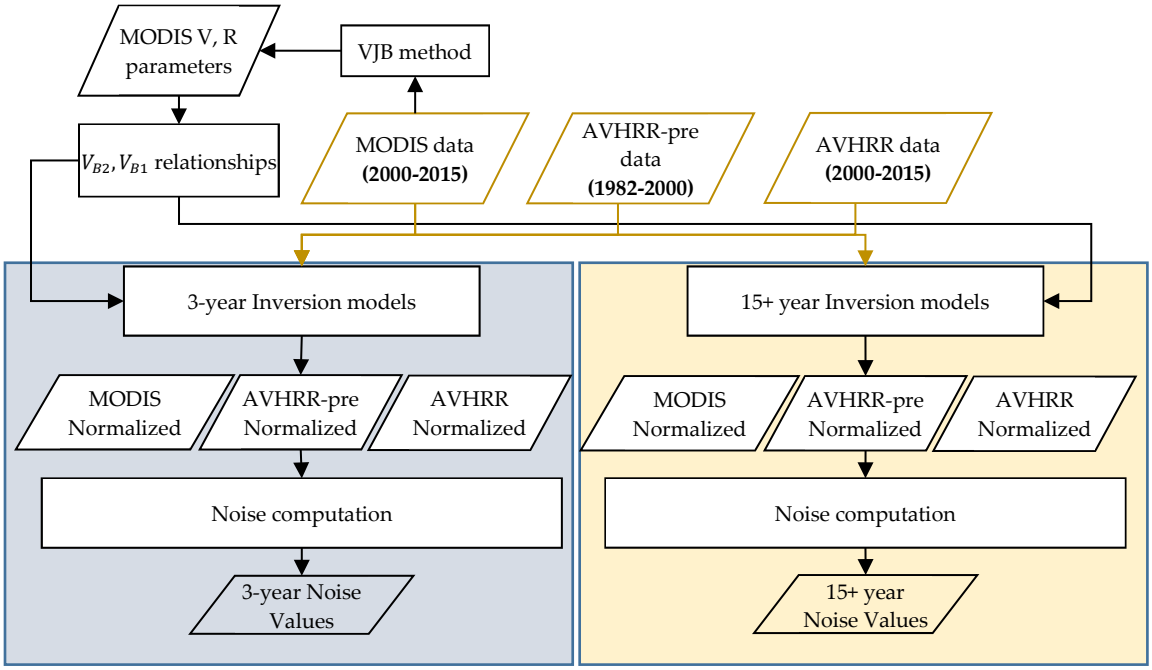

Figure 29: Flow diagram of the methodology followed by this study.

VJB method

The details of the VJB method were described in the introduction, in section 1.4.2.

BRDF parameters relationship

To minimize the propagation of the atmospheric errors into the BRDF correction, we analyze the V and R parameters for bands 1 (red) and 2 (NIR). The goal is finding a

physical relationship between the BRDF parameters of both bands to avoid using the noisy red AVHRR band. Therefore, we can derive the BRDF parameters of the NIR band and then estimate the red band based on these parameters. To build this physical relationship we use MODIS data, since we need data with the least error possible.

To do this, we use 5 points for every pixel. Every point represents an NDVI population. We use the average NDVI of this population as its core NDVI value, and the V or R values derived from them. This gives us a total of 2225 points. We then do simple regressions between the parameters for the different bands and with the NDVI itself.

Inversion period

The idea of this section is to analyze the effect of using a short versus a long period in the computation of the BRDF parameters. For the short period, we use 3 years to make sure the AVHRR time series has enough observations to allow a reliable estimate of parameters. We divided the data from (1982-1999) into three year intervals 1982-1984, 1985-1987, 1988-1990, 1991-1993, 1994-1996, and 1997-1999, and the data from (2000-2015) in 2000-2002, 2003-2005, 2006-2008, 2009-2011, and 2012-2015. For the long period, we use 18 years for AVHRR-pre and 15 years for MODIS and AVHRR. We compute the BRDF parameters using the VJB inversion and the original sensor's data. In other words, we use MODIS data to calculate MODIS BRDF parameters and AVHRR data to calculate AVHRR BRDF parameters.

Inversion models

In this section, we compare the different inversion models whose choice is based on different possible hypotheses. The aim is to see which of these are valid for the different data employed. The inversion models used in this paper are the following:

1) MODIS

We calculate the V and R parameters using the VJB method directly from MODIS data, under the hypothesis that calculating BRDF parameters using a time series with small atmospheric and calibration errors that can be propagated to the correction of directional effects provides the best correction.

2) AVHRR

Analogous to the MODIS approach, but using AVHRR data. Here we hypothesize that calculating V and R from the sensor we are attempting to correct is more representative than using a different sensor, even if said sensor has less noise in the time series. In other words, we theorize that propagated uncertainties from the atmospheric correction are smaller than data harmonization uncertainties and problems in the original model's assumption.

3) Average

Here we make the broad assumption that given the high noise in the AVHRR time series, average V and R parameters, which directly depend on the NDVI, can be applied. The correction parameters used are derived from Bréon and Vermote (Bréon and Vermote, 2012):

Table 17: V(NDVI) and R(NDVI) from (Bréon and Vermote, 2012)

Band 1 (red)	V = NDVI + 0.50	R = 0.20*NDVI + 0.10
Band 2 (NIR)	V = 2.00*NDVI + 0.50	R = -0.05*NDVI + 0.15

4) B1 (B2)

Given that the red AVHRR band (B1) is noisy due to the higher errors in the atmospheric correction, especially compared to the NIR band (B2), we attempt to correct the red band using the parameters from the NIR band. The relationships between them is estimated using MODIS data, which has a robust atmospheric correction and is now a well-established product (Vermote, El Saleous and Justice, 2002). We derive the NIR parameters using normal VJB inversion, so one value of V and R for each of the 5 NDVI populations in each pixel. Then, we apply Equation 14 and continue with the regular VJB method procedure (dependence with NDVI). These relationships are derived in the results section, but are:

$$V_{B1} = 0.84 * V_{B2} + 0.10$$
$$R_{B1} = 0.94 * R_{B2} + 0.04 \quad (34)$$

5) Stable

In this inversion, we hypothesize that the instability of AVHRR BRDF parameters is due to performing a matrix inversion using two parameters. This provides occasionally very unstable correction parameters when using noisy data. For this reason, we calculate the V_{B1} parameter using the NDVI, then the V_{B2} parameter from the V_{B1}. We finally solve R for each band from the second Equation of Equation 14. Again, this is done for each of the five NDVI populations within every pixel, after which a linear regression with the NDVI is performed.

$$V_{B1} = 1.26 * NDVI + 0.64$$
$$V_{B2} = 0.90 * V_{B1} + 0.21 \quad (35)$$

4.1.5. Results

BRDF parameters relationship

Figure 30 shows the relationship obtained between V_{B1} and V_{B2} with the NDVI, and between V and R of bands 1 and 2. The r^2, RMSE and linear fit (red line) regression values are shown in the top left of each subplot. The results show that there is a general dependence of the V parameter with the NDVI. This result was expected considering that the V parameter models the volumetric component of the vegetation. A high V value means a denser vegetation, a higher biomass, and effectively a higher NDVI value. However, the high RMSE values both for band 1 and band 2 (0.42,0.45), suggest that this is not a very precise approximation. In the case of the inter-band relationships, the results show that there is high correlation ($r^2 > 0.8$) between the parameters derived from bands 1 and 2. The small RMSE values (0.24,0.04) indicate that this approximation is reliable and could provide a smaller error than that derived by the atmospheric effects propagation from AVHRR or the spectral adjustment and calibration errors from MODIS. The cluster of points that show a 1:1 relation belongs to points with a small NDVI (NDVI < 0.2). Figure 31 shows the relationship between the Band 1 and Band 2 parameters for low NDVI values. It has been shown in previous studies that for low vegetation amount, the R_{B1} and R_{B2} values are almost identical (Roujean, Leroy and Deschamps, 1992; Marticorena *et al.*, 2004). We also noticed the

same behavior for the V parameters, when the NDVI < 0.1. In this study, we also computed the relationship of R with the NDVI, but there was little or no correlation. This is expected considering that the R parameter is associated with the geometric component, and higher NDVI values such as for forests show a similar value to bare ground.

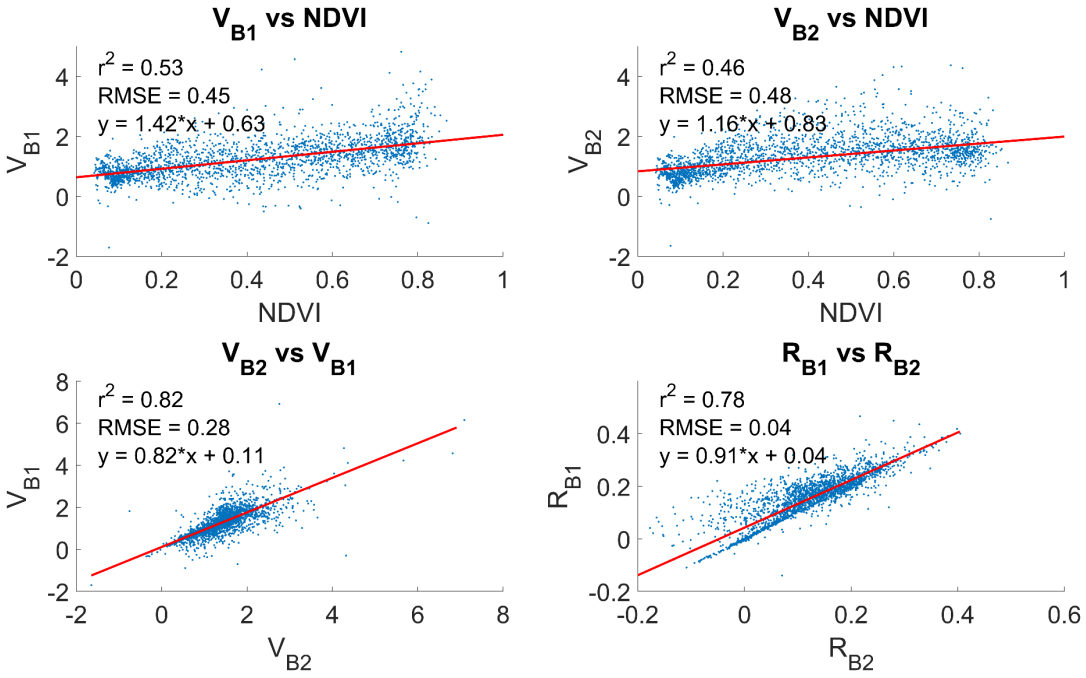

Figure 30: Relationships between V_{B1}, V_{B2}, R_{B1} and R_{B2} with each other and the NDVI, derived from MODIS.

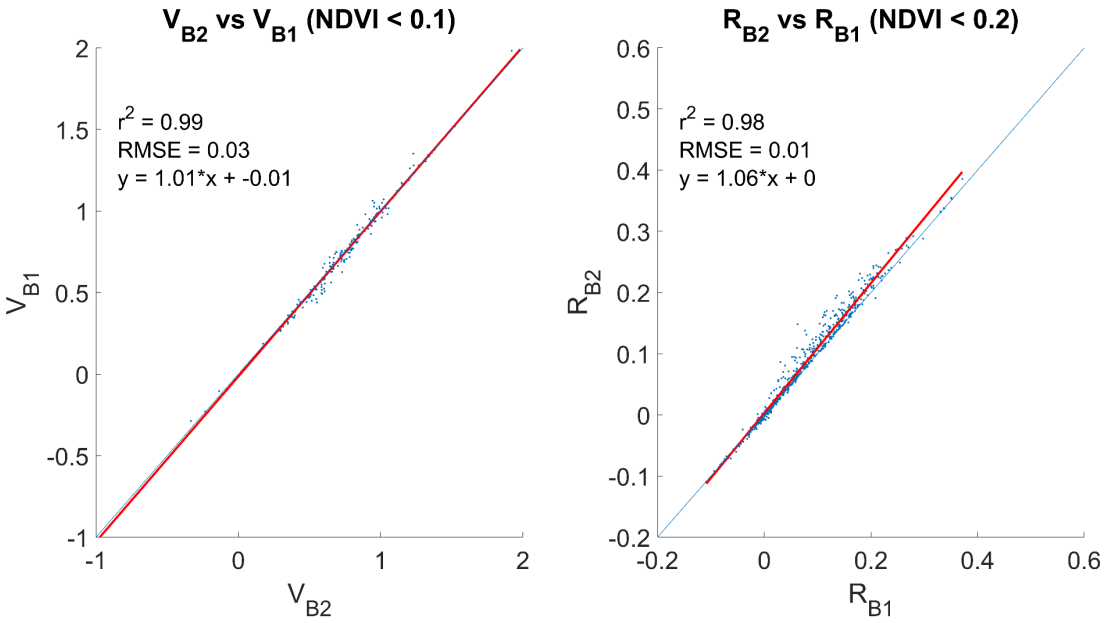

Figure 31: Regression between V_{B1}, V_{B2}, R_{B1} and R_{B2} for low NDVI values. The red line represents the linear regression fit. The blue line shows the 1:1 line.

Inversion period

Table 18 shows the average absolute noise (x10^3) of the BELMANIP sites' time series obtained when the full dataset and 3-year intervals are used to derive the correction parameters for the red, NIR and NDVI. Inversion using full and 3-year parameters is shown in green and brown font respectively. The percentage under every noise value indicates the improvement with respect to the raw data. For almost every band and dataset, the average noise of the time series using full parameters is lower than using 3-year parameters. In MODIS data, the difference between the full and 3-year parameters is of ~2.5%, 8% and 5% in the red, NIR and NDVI time series noise. This difference is lower for AVHRR-pre (~0%, 7% and 6%) and AVHRR (~2%, 5% and 1%) data.

Effectively, these results show that the effect of the gradual surface change in coarse spatial resolution pixels has little impact on the noise of the time series, as compared with the effect of the number of observations used to compute the parameters. Using a larger number of years retrieves information about the surface, which is used in the model to retrieve parameters that are more accurate and reduce the noise of the normalized time series by a significant amount, especially for the NIR and NDVI.

Table 18: Average noise (x10^3) of the BELMANIP sites' time series obtained before (Raw) and after directional effects for the red and NIR bands and the NDVI, using MODIS, AVHRR-pre and AVHRR data from top to bottom. Full and 3-year columns describe the noise after computing BRDF parameters using the whole time series, or 3-year intervals, respectively. The percentage under every noise value indicates the improvement with respect to the raw data.

		Red		NIR		NDVI	
		Full	**3-year**	**Full**	**3-year**	**Full**	**3-year**
MODIS	Raw	201.42	201.42	430.45	430.45	162.21	162.21
	MODIS	48.38 (75.98%)	53.44 (73.47%)	76.23 (82.29%)	107.80 (74.96%)	113.20 (30.22%)	121.19 (25.29%)
AVHRR pre	Raw	212.97	212.97	456.51	456.51	379.83	379.83
	AVHRR pre	130.46 (38.74%)	130.16 (38.88%)	198.10 (56.61%)	230.63 (49.48%)	363.58 (4.28%)	389.08 (-2.43%)
AVHRR	Raw	168.22	168.22	292.62	292.62	317.32	317.32
	AVHRR	103.73 (38.34%)	106.58 (36.64%)	144.02 (50.78%)	158.68 (45.77%)	315.33 (0.63%)	319.48 (-0.68%)

Inversion models

Figure 32 shows the time series of two BELMANIP pixels for different inversion models and their noise value using AVHRR-pre data. In brackets is shown the relative noise of the time series. For visual purposes, the data is shifted in the y-axis by 0.3*n in the red and 0.6*n in the NIR and NDVI for the n^{th} model. The first one is a savanna pixel located in Brazil (-14.72, -41.75). The red and NIR band show a significant improvement in the noise after the directional effects' correction of ~60% and ~80% respectively, even when using the average method, which is based on the broadest

approximation. The result can be appreciated visually, where the seasonal variation of the data can be distinguished after the correction. In the case of the NDVI, however, there is little or no improvement in the noise. When using MODIS parameters, for example, the noise increases. This is due to the intrinsic directional effects' correction of the NDVI computation (Vermote, Justice and Breon, 2009b). The second pixel is a bare ground pixel located in the Algerian Saharan Desert (28.28, -5.03). In this case, there is also a significant decrease in the red and NIR noise when using the different inversion models, but not in the NDVI. The average method, however, significantly increases the noise, evidencing that the approximation it uses might not be viable for non-vegetated sites. These results also show that the assumption that for low NDVI values, the parameters are the same for both bands is reasonable.

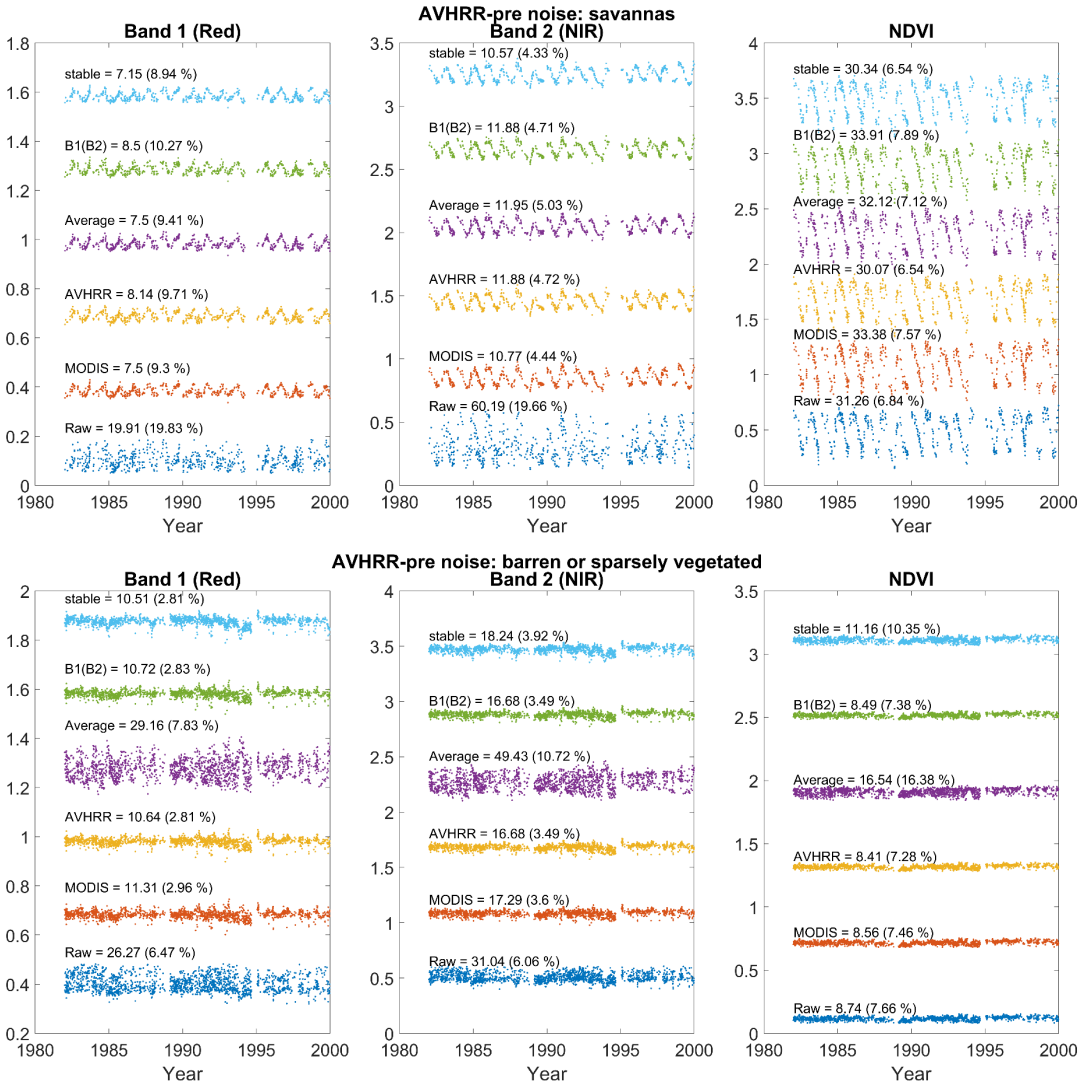

Figure 32: Time series of two BELMANIP pixels (savanna and barren) for different inversion models and their noise value using AVHRR-pre data. In brackets is shown the relative noise of the time series. For visual purposes, the data is shifted in the y-axis by 0.3n in the red band, and 0.6n in the NIR and NDVI for the n^{th} model.

To analyze the performance of every individual model in detail, we plotted the distribution of the noise corrections for every pixel considered in this study. Figure 33 shows these distributions in the form of a boxplot, using the different inversion models and for MODIS, AVHRR-pre and AVHRR data. The top and bottom blue edges of the box represent the 25^{th} and 75^{th} percentiles, respectively, while the middle red line shows

the median. Points outside the black bars are considered outliers. The green diamond represents the average of the distribution. These values are shown in Table 19.

Firstly, we can see that the average raw noise of the red and NIR time series is similar for MODIS data (0.020, 0.043) and AVHRR-pre data (0.021, 0.045), but higher than the AVHRR data (0.017, 0.029). This is caused by the large directional errors in MODIS data and the high atmospheric errors in AVHRR-pre data. Evidence of this can be seen on the NDVI noise. In MODIS, its value is very low (0.016), meaning that the intrinsic directional correction of this index has corrected most of the directional effects. In AVHRR-pre, because the directional effects are not as high, the NDVI correction errors are mostly because of atmospheric uncertainty propagation (0.038).

Secondly, looking at MODIS data (Figure 33, column 1) gives an indication of the quality of the approximations considered by the different models. As is expected, the MODIS inversion provides the best correction (75.7%, 82.3% and 30.2% for the red, NIR and NDVI respectively). Using the Average model, not only is the red and NIR noise improvement lower by ~20%, as compared to the MODIS inversion, but it also has a higher spread of the noise distribution. This is expected considering the broad generalizations of the model. The B1(B2) model shows the second best performance, only 2% worse than the MODIS inversion, indicating that this a valid approximation that could reduce the computational time while achieving high quality directional correction. For the NDVI, however, this method shows a significantly smaller improvement (10.0%) than the MODIS model (30.2%). Finally, the Stable method shows to be a valid alternative for the red band, but not for the NIR band. For the NDVI value it can correct ~5% better than the B1(B2) method.

Analyzing the effects of these models on AVHRR-pre data (Figure 33, column 2) can now show whether the error provided by their approximations is smaller or higher than the propagated atmospheric error. The MODIS model on AVHRR-pre provides a good correction of the directional effects with ~45.6%, 59.7% in the red and NIR bands, 5% and 3% better than the AVHRR-pre model. This shows that MODIS parameters are preferable to AVHRR-pre derived parameters. The opposite is true for the NDVI. The Average and the B1(B2) model show the worst performances among all of them, with significant difference with the MODIS model in the red (~8% and 9%) and the NIR (~6% and 3%). This is expected for the Average method but is surprising for the B1(B2) model considering its good performance with MODIS data. It seems like the inversion with two parameters still is not good enough, despite having reliable assumptions. In the case of the NDVI, the three of them provide a negative improvement (~4%) given that the noise on the raw data is already low. Finally, the Stable method provides the best improvement in the red and NIR bands, with differences of ~9% and 8% respectively, compared to the AVHRR-pre model. This shows that performing the inversion with one parameter provides a higher stability to the parameters and therefore a smaller distribution in the corrected noise values, as can be appreciated by the width of the boxplots in Figure 33. In the NDVI, it provides a positive improvement of 2.87%, but it is still lower than using the AVHRR-pre data.

These results are analogous to the AVHRR data (Figure 33, column 3), but with a significantly smaller difference between the methods. The Stable method, for example, only provides a ~3% and 2% improvement difference with the AVHRR model in the red and NIR bands respectively. The average method on AVHRR data improves

significantly less than with AVHRR-pre data. This is because atmospheric errors are not as high in this time series and, therefore, the broad assumptions made by the model provide more uncertainty than the propagated atmospheric perturbations.

Table 19: Average noise (x10^3) of the BELMANIP sites' time series obtained before (Raw) and after directional effects using the models described for the red and NIR bands and the NDVI, and using MODIS, AVHRR-pre and AVHRR data from top to bottom. The percentage next to every noise value indicates the improvement with respect to the raw data.

		Red	NIR	NDVI
MODIS	Raw	**201.42**	**430.45**	**162.21**
	MODIS	**48.94** (75.70%)	**76.23** (82.29%)	**113.20** (30.22%)
	Average	**90.19** (55.22%)	**163.47** (62.02%)	**175.16** (-7.98%)
	B1(B2)	**53.28** (73.55%)	**76.28** (82.28%)	**146.00** (10.00%)
	Stable	**53.33** (73.52%)	**89.74** (79.15%)	**136.81** (15.66%)
AVHRR pre	Raw	**212.97**	**456.51**	**379.83**
	MODIS	**115.96** (45.55%)	**184.07** (59.68%)	**396.65** (-4.43%)
	AVHRR-pre	**126.98** (40.37%)	**198.10** (56.61%)	**363.58** (4.28%)
	Average	**132.78** (37.65%)	**210.16** (53.96%)	**394.81** (-3.94%)
	B1(B2)	**134.41** (36.89%)	**199.32** (56.34%)	**397.18** (-4.57%)
	Stable	**108.75** (48.93%)	**163.30** (64.23%)	**368.93** (2.87%)
AVHRR	Raw	**168.22**	**292.62**	**317.32**
	MODIS	**103.42** (38.52%)	**145.35** (50.33%)	**314.67** (0.84%)
	AVHRR	**104.08** (38.13%)	**144.02** (50.78%)	**315.33** (0.63%)
	Average	**116.37** (30.82%)	**166.03** (43.26%)	**329.07** (-3.70%)
	B1(B2)	**105.14** (37.50%)	**144.74** (50.53%)	**315.00** (0.73%)
	Stable	**99.28** (40.98%)	**140.84** (51.87%)	**314.92** (0.76%)

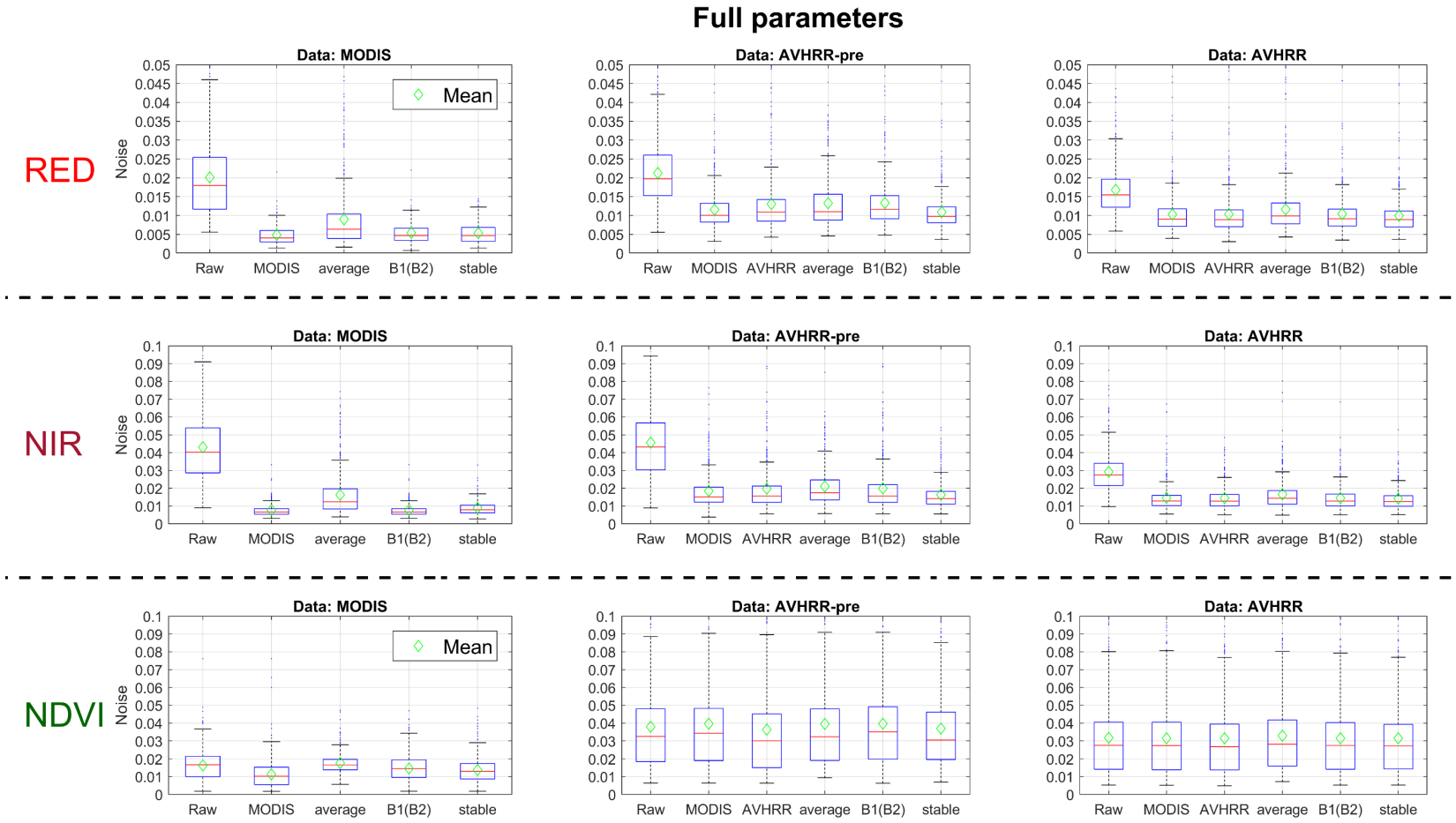

Figure 33: Noise distributions for all the bands considered (rows), using the different inversion models and for MODIS, AVHRR-pre and AVHRR data, (columns 1, 2, and 3, respectively). The green diamonds represent the average of the distribution. The top and bottom blue edges of the box represent the 25th and 75th percentiles, respectively, while the middle red line shows the median. Points outside the black bars are considered outliers.

4.1.6. Discussion

BRDF parameters relationship

The V parameter shows good correspondence with the NDVI, which is expected considering that it models the volumetric component of vegetation. Therefore, it is not surprising that we find a relationship between them. The R parameter can be physically interpreted as the aerodynamic roughness (Marticorena *et al.*, 2004). The relationship between the aerodynamic roughness and the NDVI is not that evident, in fact we did not find any meaningful relationship between the parameters. Given a certain pixel and its geometry, it is reasonable to think that for higher amounts of vegetation, the aerodynamic roughness is bound to change. In fact, Franch et al., studied the possibility of a quadratic evolution of R with the NDVI within a pixel (Franch *et al.*, 2014).

Considering that the R parameter is associated with a geometrical component, one would expect it to be independent of the spectral band. Experimental results have shown that this isn't true and that there is a difference between both values for medium to high NDVI values (Roujean, Leroy and Deschamps, 1992; Marticorena *et al.*, 2006; Franch *et al.*, 2013). We did find, nevertheless, a good relationship between the R parameter for both bands, which have a slope relatively close to one and an intercept close to zero. For low NDVI values, the R parameters are independent of the spectral band. This was also the case for V parameters with NDVI < 0.1, which as far as we are concerned, has never been observed in previous literature.

Inversion period

Originally, the VJB method was performed using 5-years of data. The results showed an improvement of ~30% in the NDVI using MODIS data (Vermote, Justice and Breon, 2009b), which agree with our results. When including a higher number of years in the inversion, we are increasing the amount of observations that are used in the model. This means increasing the range of observation geometries and of possible NDVI values that the pixel can have during the years. However, the accuracy gained by including these observations in the models might be counterbalanced by the change in vegetation characteristics of the target over the years. The larger the amount of years, the more likely it is that this change occurs, and the less likely it is for the assumptions behind the VJB method to hold. However, the analysis from this section on the different bands and sensors has shown that this change in vegetation is insignificant compared to the information gained by the increased number of observations. This might only be the case for coarse spatial resolution, where vegetation dynamics do not change the pixel value significantly. When using high spatial resolution, vegetation dynamics or human factors such as deforestation or agriculture practices, can change the surface drastically. In this case, a further analysis is required to determine what the adequate inversion period to retrieve the V and R parameters would be.

Inversion models

The results of this section show that the conclusions are different for the NDVI correction than they are for the individual bands. For the red and NIR bands, the Stable model proved to be the best method to use when the data's time series has too much

noise to derive the correction parameters from it. This is true especially for AVHRR-pre, for which the Stable method provided a significant improvement in the noise correction. This is therefore the recommended model for the derivation of surface albedo using AVHRR-pre and AVHRR data, if the NDVI computation is not required. For MODIS data, the use of the MODIS inversion is still preferable, as assumptions made by the models devised introduce uncertainty. In the case of the NDVI, however, the use of the regular VJB model using parameters derived from the same data is preferred. For users with a large computational burden that look for a compromise between computational time and accuracy, the use of the Average method provides very fast correction parameters at the expense of ~10% noise improvement. If the BRDF correction parameters are already available from MODIS data or another sensor with little atmospheric perturbation at the same spatial resolution, the use of these parameters provides the second best correction after the Stable method with virtually no significant computational time required in comparison.

4.1.7. Conclusions

In this paper, we explore different approaches to find the most robust way of applying the VJB correction to AVHRR data. To do this we use AVHRR data from 1982-2015 divided in AVHRR-pre (1982-2000) and AVHRR (2000-2015) and MODIS data (2000-2015) at CMG spatial resolution (0.05°) in 445 BELMANIP2 sites. First, we compare the effect of using 3-years or 15+ years to derive the BRDF parameters. We found that for coarse spatial resolution, where the vegetation characteristics of the target do not appear to change significantly, it is preferable to use 15+ years of

observation. This result was true both for AVHRR and for MODIS data. The differences were higher for the NIR band, where the average noise was reduced by 7% when using the whole time series from AVHRR-pre data instead of 3-year parameters.

Secondly, we used MODIS data to retrieve relationships between the BRDF parameters. With the information derived from this sensor, we built different models based on the VJB method, which aim to minimize the propagation of the atmospheric errors present in the AVHRR data to the correction of directional effects. We found that for the red and NIR bands, the Stable method provides a robust correction in terms of reducing both the average noise of the pixels considered and the width of the noise distribution. This is the recommended model for surface albedo retrieval for the VJB method using AVHRR data. For the NDVI, however, we found that the lowest average noise is obtained by correcting MODIS data with MODIS derived parameters and AVHRR data with AVHRR derived parameters. These results are true both for AVHRR-pre, which has no aerosol or water vapor correction, and for AVHRR, which uses MODIS information for the atmospheric correction.

Further studies should focus on the effect of the spatial resolution on the assumptions made by the VJB method, such as the invariability of a certain site during the composite period of the model. This information is especially useful for the derivation of surface albedo. A surface albedo using AVHRR data from 1982-2018 is of great interest to the scientific community, especially one which relies heavily on observations and on semi-empirical physical models.

4.2. Land surface albedo computation

Once all the previous steps have been applied on the original LTDR data, the surface albedo for land is obtained by using Equation 36.

$$a(\theta_s) = \frac{2}{\pi}\int_0^{\pi} d\phi \int_0^{\pi/2} \rho(\theta_s, \theta_v, \phi)\cos(\theta_v)\sin(\theta_v)\, d\theta_v \quad (36)$$

After substituting $\rho(\theta_s, \theta_v, \phi)$ for the definition in Equation 6, the predictive relation in Equation 37 calculates the land surface albedo (Roujean, Leroy and Deschamps, 1992; Schaaf *et al.*, 2002b).

$$\alpha(\theta_s) = k_{geo} I_{geo} + k_{vol} I_{vol} \quad (37)$$

For the Black-sky albedo:

$$I_{geo} = \frac{4}{3\pi}(-1.29 + 0.02\,\theta_s - 0.20\,\theta_s^2 + 0.05\,\theta_s^3) \quad (38)$$

$$I_{vol} = 0.14\,\theta_s - 0.24\,\theta_s^2 + 0.37\,\theta_s^3 \quad (39)$$

For the **White-sky albedo**, the result does not depend on θ_s:

$$I_{geo} = -1.37 \quad (40)$$

$$I_{vol} = 0.09 \quad (41)$$

To obtain the **Blue-sky albedo**, I need to calculate the diffuse skylight ratio (D). In order to do this, I use

Finally, in order to obtain the shortwave surface albedo, narrowband to broadband coefficients need to be used for the AVHRR bands, as described in Equation 5. Liang 2001 (Liang, 2001) provides accurate conversion formulae for AVHRR sensors, by

using radiative-transfer simulations for different surface reflectance spectra and atmospheric conditions. These are shown in Equation 42:

$$\alpha_{sw} = -0.338\,\alpha_1^2 - 0.271\,\alpha_2^2 + 0.707\,\alpha_1\alpha_2 + 0.292\,\alpha_1 + 0.526\,\alpha_2 + 0.004 \quad (42)$$

Where α_1, α_2 are the surface albedos of band 1 and band 2, respectively.

4.3. Snow albedo computation

4.3.1. Abstract

Due to its distinctive physical properties and large seasonal variability, snow plays a critical role in the Earth's radiative forcing though positive feedbacks in terms of surface albedo. Snow albedo depends on two main parameters: snow grain size and impurity content. The AVHRR sensor, however, lacks the critical bands to estimate them accurately. For this reason, in this study I attempt to obtain snow albedo using the MCD43 product as a reference, whose snow albedo retrieval has been validated over snow-covered sites yielding uncertainties below 0.05. In order to do this, I use observations with less than 10-minute overpass time difference between MODIS Aqua and AVHRR to create two random forest regression models that predict snow black-sky and white-sky albedos from AVHRR input bands. This process is done both when band 3A is operational, and when band 3B is operational. These models allowed me to retrieve snow albedo from the LTDR product with a RMSE < 0.07 when using the AVHRR data with band 3B operational, and RMSE < 0.05 when band 3A was operational. These results can be applied on the LTDR product all around the world, ensuring less than 10% uncertainty in the retrieval.

4.3.2. Introduction

Due to its distinctive physical properties and large seasonal variability, snow plays a critical role in the Earth's radiative forcing though positive feedbacks related to albedo, moisture storage, latent heat and insulation of the underlying surface (Groisman, Karl and Knight, 1994; Stieglitz *et al.*, 2003). Ecosystems at high latitudes (50^0-90) are experiencing an enhanced climate warming (~0.50^0C decade-1 over Eurasia, and ~1.06 ^{0}C decade-1 over North America, (2003)) which will be aggravated by a series of positive feedbacks (Chapin *et al.*, 2005b). The two main processes that are driving the terrestrial to climate feedbacks are the northward expansion of vegetation (Pearson *et al.*, 2013b) and the changes in extent and duration of snow cover (Chapin *et al.*, 2005b; Déry and Brown, 2007b). The decline in albedo ($\Delta\alpha$) between snow-covered and snow-free conditions represents the strength of the albedo feedback associated with these changes (Qu and Hall, 2007b; Loranty *et al.*, 2014b). This feedback is known to be very important for regional climate change and plays a very significant role in Arctic amplification. Using satellite data, (He *et al.*, 2013) found that melting in Greenland from 1981 to 2012 decreased surface albedo at a rhythm of -0.009 ± 0.002 decade-1, while (Loranty *et al.*, 2014b), showed that a gradual increase in tree cover in northern high latitudes from 2006-2010 captured by MODIS data was accompanied by a gradual decrease in albedo (from ~0.75 to around 0.25) in April due to snow-masking effects of vegetation.

As the temperature rises, the snow melts faster and sooner and the extent of the snow cover is reduced, allowing vegetation to expand and grow where it was not possible before. The land under what previously was snow has a lower albedo than the snow

itself, so the Earth absorbs more solar radiation (reducing the solar heating at TOA and increasing the thermal energy provided by the Earth). Snow packs that aren't completely melted also experience a decrease in their albedo values (Qu and Hall, 2007b). This raises the temperature and encourages further melting. Snow albedo feedback values using MODIS range from -0.87% K-1 (Qu and Hall, 2014) to -1.22% K-1 (Fletcher, Thackeray and Burgers, 2015), which represent the percentage reduction in albedo per degree kelvin. Its substantial contribution to high latitude warming trends therefore highlights the importance of understanding how surface albedo is changing in these latitudes.

In the literature, the methods to obtain snow albedo vary from physically based models (Lyapustin *et al.*, 2009; Gardner and Sharp, 2010), to empirically based methods (Liu *et al.*, 2013). The former requires atmospheric correction over the snow covered pixels, while the latter might not work for a wide variety of locations and illumination or observation conditions. Empirical methods establish a direct relationship between the Top of Atmosphere (TOA) reflectance and the broadband albedo. Studies have shown that if these empirical methods study a wide variety of illumination/observation conditions around the world, they can provide reliable results (Liu *et al.*, 2013).

Typically, models used for land BRDF modelling and further surface albedo retrieval do not provide accurate results when applied to snow or ice covered pixels, because they vary significantly with the grain size and angle of incidence of the incoming radiation (Warren, 1982), the amount of impurities such as soot, dust and volcanic ash (Warren and Wiscombe, 1980), and surface roughness (Carroll and Fitch, 1981). The absence of any 1.6μm spectral band in AVHRR/2 sensors (before 2000) makes the

retrieval of the snow grain size using satellite data unreliable (Lyapustin *et al.*, 2009), and the impurities concentration present in the snow is difficult to quantify using AVHRR data, especially the computation of the light-absorbed carbon which is used in the snow albedo parametrization (Gardner and Sharp, 2010).

For this reason, I attempt to obtain snow albedo using the MCD43 product as a reference, whose snow albedo retrieval has been validated over snow-covered sites (Liang, Stroeve and Box, 2005; Stroeve *et al.*, 2005; Wang *et al.*, 2012), yielding uncertainties below 0.05. This product however, has shown a slight bias and problems for pixels with a high solar zenith angle (>65^0) and during times of spring snow melt (Zhang *et al.*, 2010).

4.3.3. Material

First, I downloaded the MCD43C3v006 product from https://lpdaac.usgs.gov/products/mcd43c3v006/. This dataset is produced daily using 16 days of Terra and Aqua MODIS data at CMG spatial resolution. Second, I downloaded all surface reflectance AVHRR bands from the LTDR product from the period coinciding with MODIS observations (2000-2018) along with angular and overpass time information. Thirdly, I downloaded data from the MYD10C1 product, to determine with high accuracy what pixels are snow. Finally, I downloaded the Water Vapor (WV) from MERRA2 reanalysis data and interpolated it to CMG resolution and AVHRR overpass times.

4.3.4. Methods

The core methodology behind this study relies on performing a statistical regression between the LTDR product's bands and the broadband shortwave surface albedos available in the MCD43C3 product, namely the black-sky and white-sky albedos. However, before proceeding, two previous steps need to be completed.

First, since MODIS and AVHRR have different overpass times, a methodology similar to that from chapter 3 was employed: only snow pixels with an overpass time difference of less than 10 minutes were retrieved from both databases for comparison. This ensures that they are observing the same surfaces and with the same solar zenith angle. Figure 34 shows a map of the distribution of said pixels used for this study.

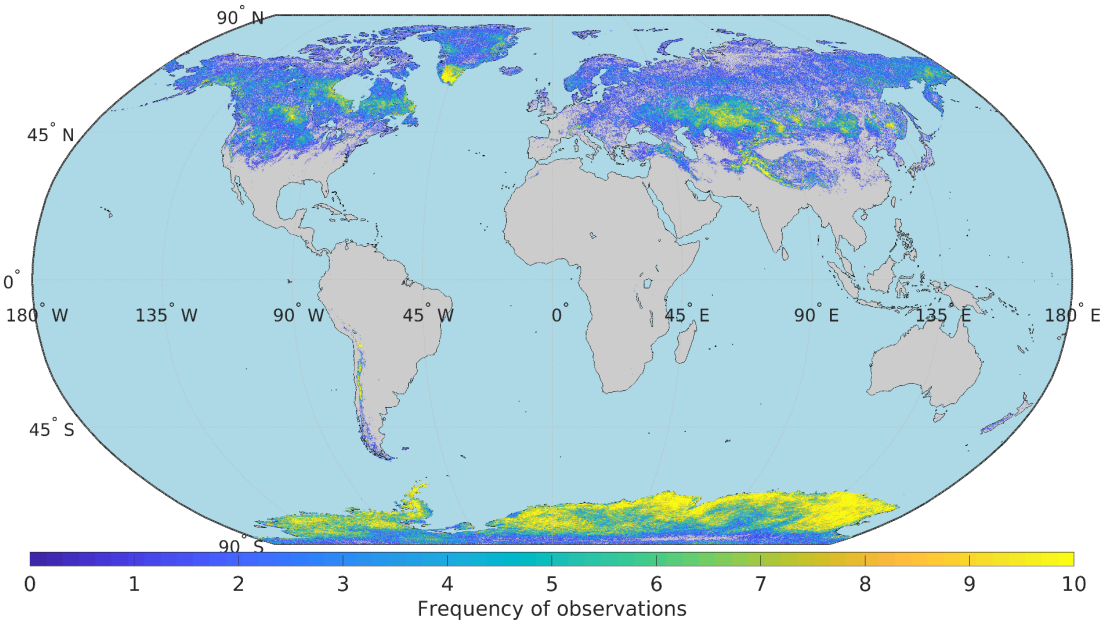

Figure 34: Frequency of observations with an overpass difference between LTDR and MCD43C3 smaller than 10 minutes. The total number of pixels is ~34 million.

To identify snow pixels from cloud or clear land pixels, the snow mask from MYD10C1 was used. Second, since there are specific periods where the AVHRR band

3A was active in place of band 3B, the regression algorithms need to be calculated for both scenarios. In order to increase the number of features and the quality of the regression, the band 3B reflectance was calculated from the thermal 3B band, whenever this is active, following the same procedure as in section 3.2.3. When the band 3A is active, the NDSI is calculated by using Equation 43. In this case, AVHRR band 1 is used as $\rho_{0.6\mu m}$ and band 3A is used as $\rho_{1.6\mu m}$. Table 20 shows a list of the features used as inputs for both cases.

$$NDSI = \frac{\rho_{0.6\mu m} - \rho_{1.6\mu m}}{\rho_{0.6\mu m} + \rho_{1.6\mu m}} \tag{43}$$

Table 20: Features used as input for the regression algorithm when band 3B is available (left) and when band 3A is available (right).

With B3B	With B3A
B1	B1
B2	B2
B3B	B3A
T3	NDSI
T4	T4
T5	T5
SZA	SZA
VZA	VZA
PHI	PHI

These features are finally input into a random forests regression model. This model is commonly used as a regression tool in remote sensing, because it can successfully handle large amounts of data, high data dimensionality and multicolinearity. It is also fast to apply and is insensitive to overfitting, though it is sensitive to the sampling design (Breiman, 2001; Belgiu and Drăguț, 2016). The most common ways to apply

this model are using a boosting or bagging approach. In particular, the bagging random forest approach consists of using a bootstrapped dataset of the original input data to be fed into several regression trees (Strobl, Malley and Tutz, 2009). The trees are then trained using two different tuning parameters: The number of trees and the leaf size. The former controls the amount of trees to be trained, while the latter controls the size of each tree. There is no penalty other than computational time increase on increasing the number of trees; however, larger trees tend to be more robust over the testing data. Predictions made by the individual trees are then averaged to retrieve the final prediction of the bagged random forest regression model.

In this study, I first divided the input data into a train and a test dataset, containing ~27.5 million and ~7 million pixels, respectively for the models using band 3B, and ~6.8 million and ~1.8 million pixels for the models using band 3A. The training data is used as an input for the random forest model, whereas the train data was used later to check its performance with data outside the training sample. Once the data is ready, four different random forest regression models were trained in this study. Two to obtain Black-Sky albedo and White-Sky albedo for the cases where the band 3B is operational and another two to obtain them when the band 3A is operational. The prediction of the black sky albedo was used as an input to the model, since the White-Sky albedo is obtained theoretically through the integration of the Black-Sky albedo over all illumination angles.

The next step is to tune the number of trees and the leaf size. In order to do this, I run the model under different values for these parameters. The retrieved predictions by the model are then compared to the true MCD43C3 broadband albedo value via the RMSE

and Mean Absolute Error (MAE). Figure 35 shows the evolution of these parameters as the number of trees is increased (left) and the leaf size is increased (right). The RMSE is shown on the left axis, while the MAE is shown in the right axis. Orange lines represent testing data, while blue lines represent training data.

In order to select the final parameters, one has to consider what values will provide a low enough RMSE, while at the same time, not yielding significant differences in performance between the train and test data. In this case, I chose a number of leaves of 5000, and a number of trees of 80. Following the same approach for the band 3A models, I chose a number of leaves of 1000, and a number of trees of 80, since the amount of input data was significantly lower.

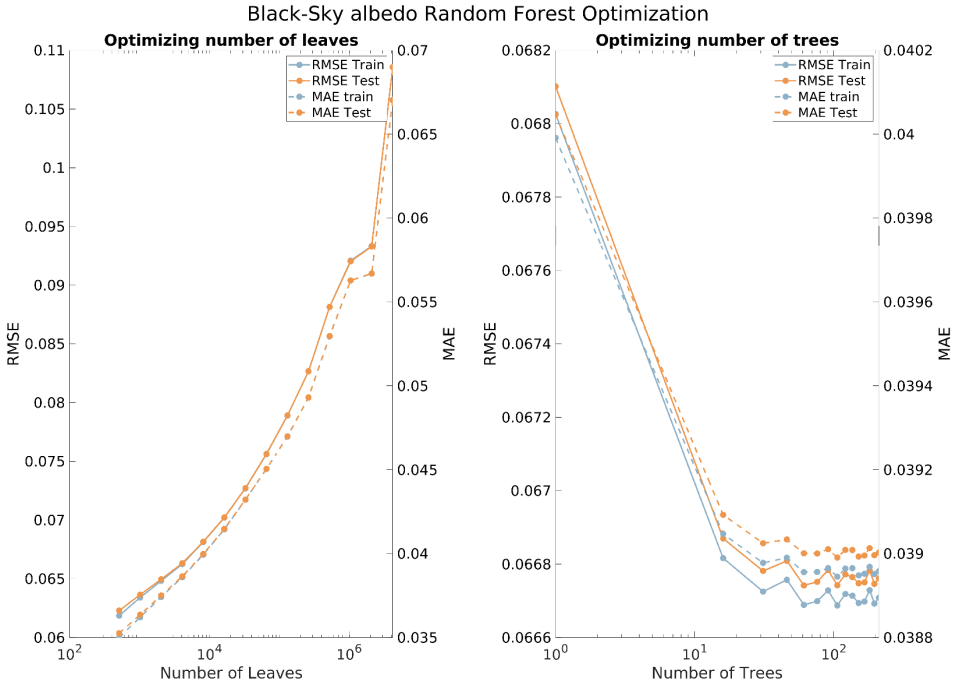

Figure 35: Black-Sky albedo parameter tuning. The left plot shows the changing performance of RMSE (left axis) and MAE (right axis) as the number of leaves changes. The right plot shows the same, but when the number of trees changes. Orange lines represent testing data, while blue lines represent training data.

4.3.5. Results and discussion

Figure 36 shows the comparison between predicted (Random Forest) and true (MCD43C3) Black-Sky and White-Sky albedos for the **training** datasets of the LTDR data when band 3B is active (top) and when band 3A is active (bottom). The results show values of RMSE similar to what was expected from Figure 35 when using the optimum tuning parameters. The overall correlation coefficient between the parameters is of > 0.85 when using band 3B and ~0.7 when using band 3A. The bias of the 3A model is significantly higher (4% vs 1%), especially for low snow albedo values. The uncertainty, however, is lower, (0.07 vs 0.05). Both cases perform satisfactorily for snow albedo values above 0.5. The results when applying these models on the **testing** dataset are shown in Figure 37. The results on data that was not used to build the model are almost identical. This indicates that firstly, the choice of the tuning parameters is acceptable, and secondly, that the application of these regression models on data from the rest of the LTDR product are acceptable for use on a global scale, with errors below 10%.

The difference in performance between the 3A and 3B models has to do with the limited data available to build the model in the former case. The data that we used as input to the model includes almost every pixel available measured with the band 3A in the LTDR product. This translates into a different value of the tuning parameters for this model, which in turn affects the resulting RMSE and correlation values. Overall, the band 3A, along with information from the NDSI, provides a better estimate to obtain the snow albedo, at least for values above 0.6, which are more likely to be pure snow.

One limitation behind this methodology, though, is the fact that the snow mask used in this study is of higher quality than the one used in the LTDR product and developed in Chapter 3. Uncertainties related to misclassifications of the MACSSA algorithm could arise that are not accounted for in this study.

4.3.6. Conclusions

In this section, I have attempted to estimate snow albedo for the AVHRR product by means of a random forest regression model. This model used all AVHRR bands available at the time of observation; when the 3A band was operative, the inputs were different from when the 3B band was operative. The MCD43C3 product was used as true snow value, and was obtained for pixels with less than 10-minute overpass difference between AVHRR and MODIS Aqua satellites, to ensure that snow pixels were being observed. The regression models were optimized to minimize RMSE and MAE parameters, and the final predictions from the model were compared to both the training and testing data. The performance of the product (RMSE < 0.07) make this product applicable to the LTDR product all around the world, ensuring less than 10% uncertainty in the retrieval.

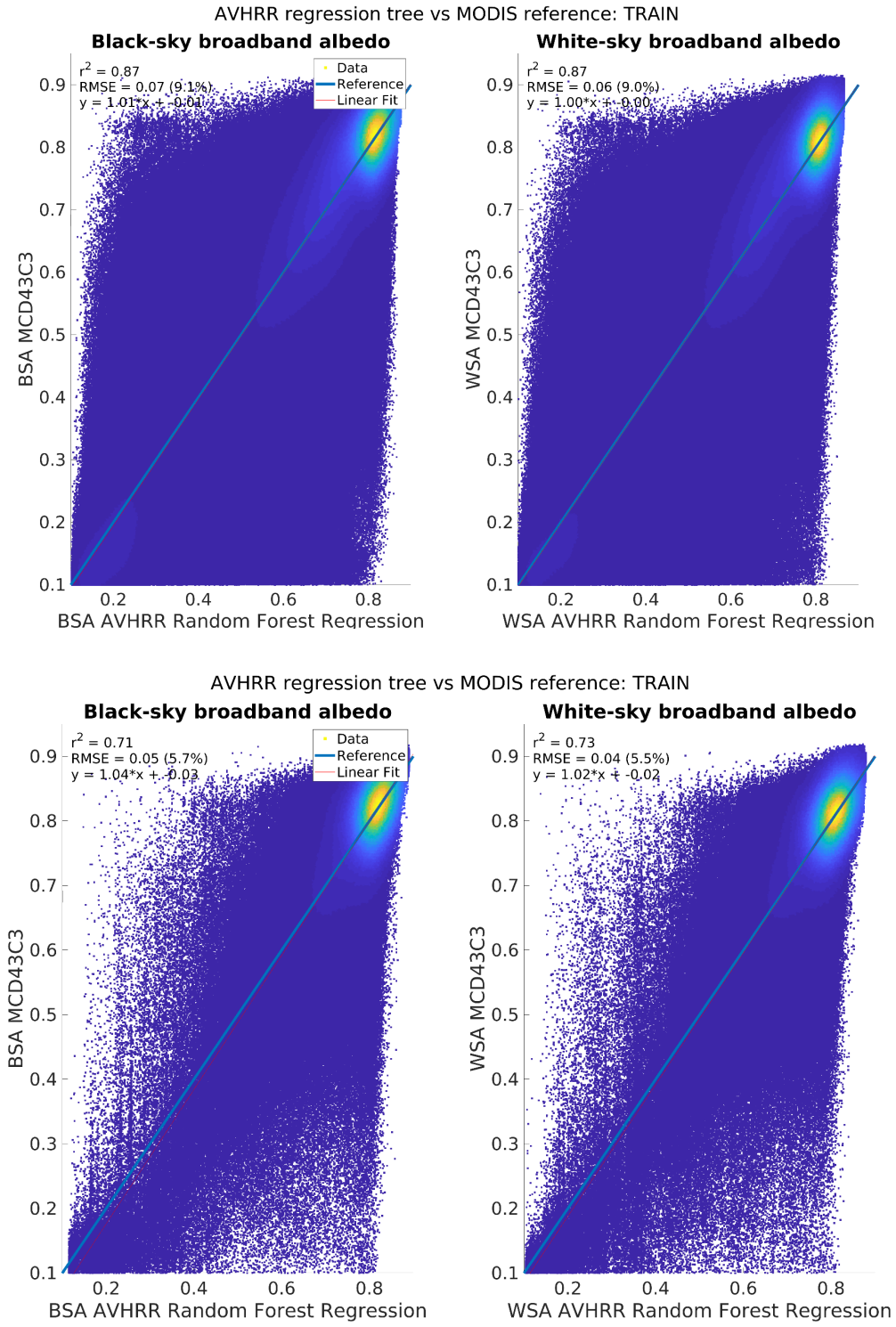

Figure 36: Comparison between predicted (Random Forest) and true (MCD43C3) Black-Sky and White-Sky albedos for the training datasets of the LTDR data when band 3B is active (top) and when band 3A is active (bottom).

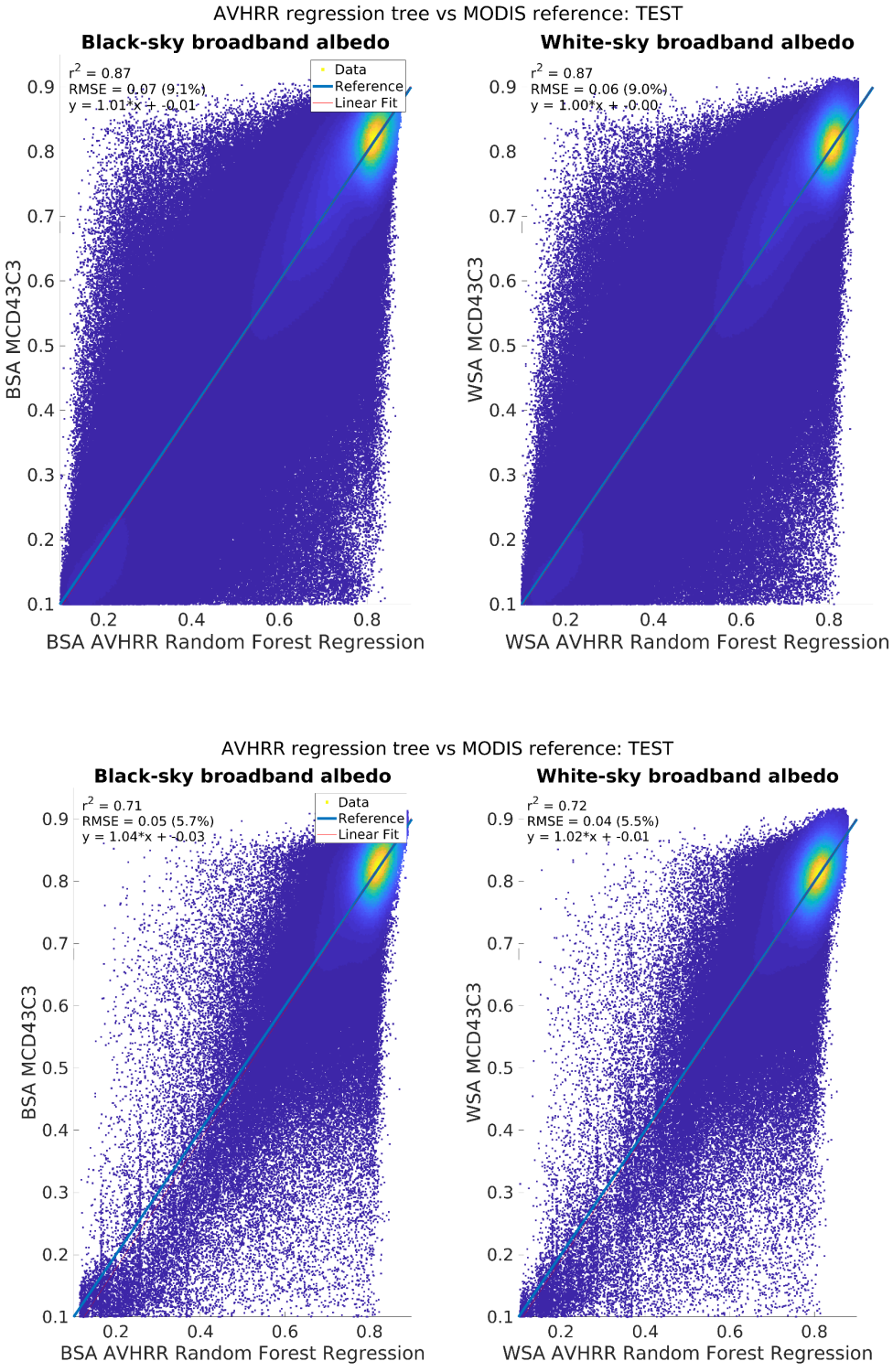

Figure 37: Comparison between predicted (Random Forest) and true (MCD43C3) Black-Sky and White-Sky albedos for the testing datasets of the LTDR data when band 3B is active (top) and when band 3A is active (bottom).

Chapter 5: Surface Albedo of the Earth and cross-comparison

After the steps completed from chapters 2-4, the SALSA product is ready for a global analysis. In order to ensure its reliability and stability, it needs a comprehensive cross-comparison with the MCD43C3 surface albedo product, along with the analysis of its performance in a spatiotemporal manner. In the first section, I will cross-compare the SALSA and MCD43C3 products spatially, analyze their seasonal behavior, the performance along different NOAA satellites and the differences in trend estimation. To do this, the MCD43C3v006 product is downloaded for its whole time series (2000-2018) and for the whole world. In the second section, I will analyze the surface albedo retrieved from the SALSA product as a whole, studying the long-term trends and some qualitative analysis of what is causing said trends.

5.1. Comparison of SALSA with MCD43C3

5.1.1. Temporal average

The first study consists on computing the average of all high quality pixels of white-sky and black-sky albedos for the same period (2000-2018) for the SALSA and MCD43C3 products. Figure 38 shows a map of the resulting white sky albedos for the SALSA (top) and MCD43C3 (bottom). The grey colors in land represent pixels without any values during the composite period. These results show an overall qualitative agreement between the products, with realistic surface albedo values for the different biomes present in the Earth. The highest average values (0.8-0.9) are obtained in high latitude pixels covered in snow such as Greenland or Antarctica, followed by barren land (0.4-0.6) in the Sahara desert, the Arabian Peninsula or Australia. Lower surface

albedo values correspond to vegetated regions, with higher values around croplands, grasslands and savannas (0.15-0.2) and lower values around forested areas like the Amazon forest, the Congo Basin or Northern latitudes conifer forests.

Figure 39 shows the density scatter plot of the black-sky (top) and white-sky (bottom) global averages. The overall number of pixels is of ~8.6 million. The black line shows the 1:1 line, whereas the red line represents the best linear fit between them. In order to compare them quantitatively, the plot also shows the fit parameters, the r^2, the Accuracy, Precision and Uncertainties. The results show a good agreement between both datasets, with an $r^2 > 0.99$ in both cases, an Accuracy value < 0.005 and an Uncertainty of the order of 0.02. This uncertainty value is comparable to other surface albedo products obtained using AVHRR data when compared against MCD43C3 (Liu *et al.*, 2013; Sánchez-Zapero, 2019). The performance over snow seems to be slightly worse in terms of uncertainty than the performance over land, as expected from the snow albedo retrieval algorithm. Section 5.1.4 will focus on the comparison over different biomes.

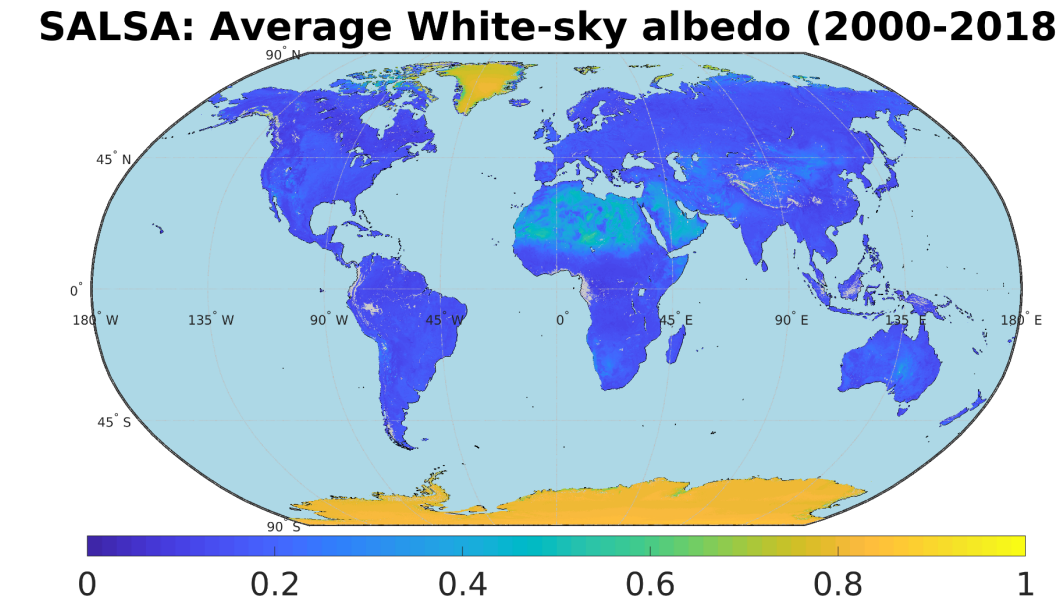

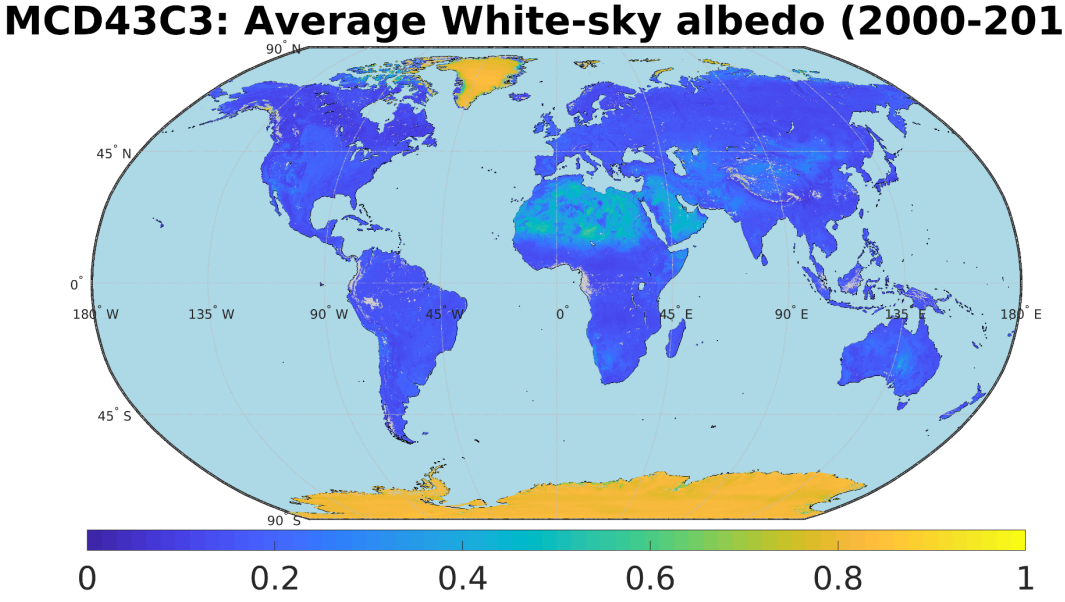

Figure 38: Map of the white sky albedo averages from 2000-2018 for the SALSA (top) and MCD43C3 (bottom) products. The grey colors in land represent pixels without any values during the composite period.

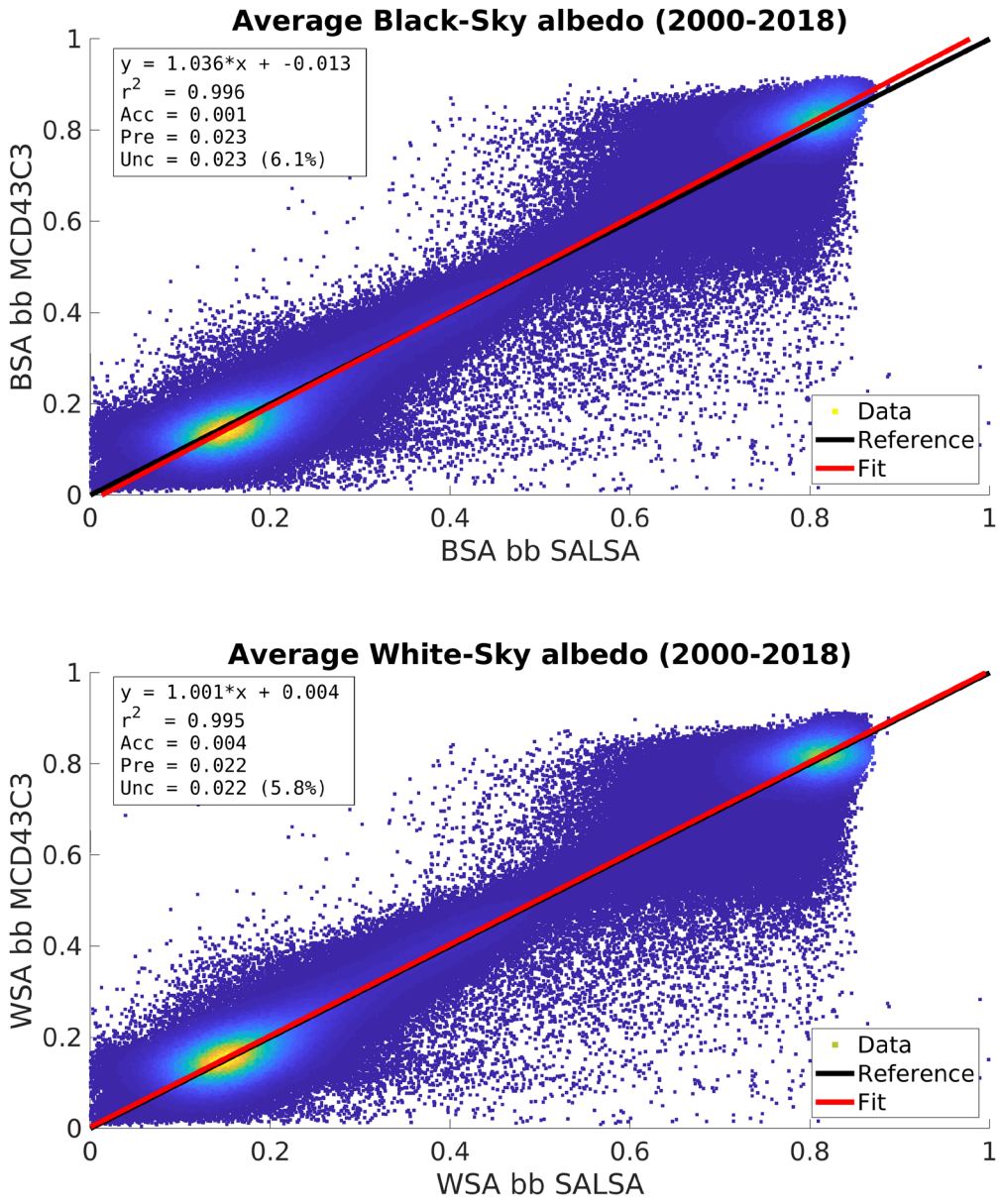

Figure 39: Density scatter plot of the black-sky (top) and white-sky (bottom) global averages. The overall number of pixels is of ~8.6 million. The black line shows the 1:1 line, whereas the red line represents the best linear fit between them.

5.1.2. Seasonal average

The next step is to compare the product's seasonality behavior with that of the MCD43C3's product. In order to do this, I computed the global average of every month

from 2000-2018. In order to estimate the global albedo, averaging all the pixels equally would lead to an overestimation of albedo values. This happens because the equirectangular projection used in the CMG that both products use, is not an equal-area projection, so pixels in high and low latitudes would be overrepresented in the average. Since these are typically also the ones with the highest albedo values, the effect becomes too large to ignore. To convert an equirectangular projection to an equal-area projection such as the sinusoidal, the cosine of the latitude can be used as an approximation of the weighting factor (Zhang *et al.*, 2010). The sinusoidal coordinates (x,y), are Once this correction is applied, the global averages can be calculated.

The results are shown in Figure 40. The SALSA product is shown in blue, the MCD43C3 product is shown in red and the difference between them is shown in black (right axis). The solid lines represent the White-sky albedo, while the dashed lines represent the Black-sky albedo.

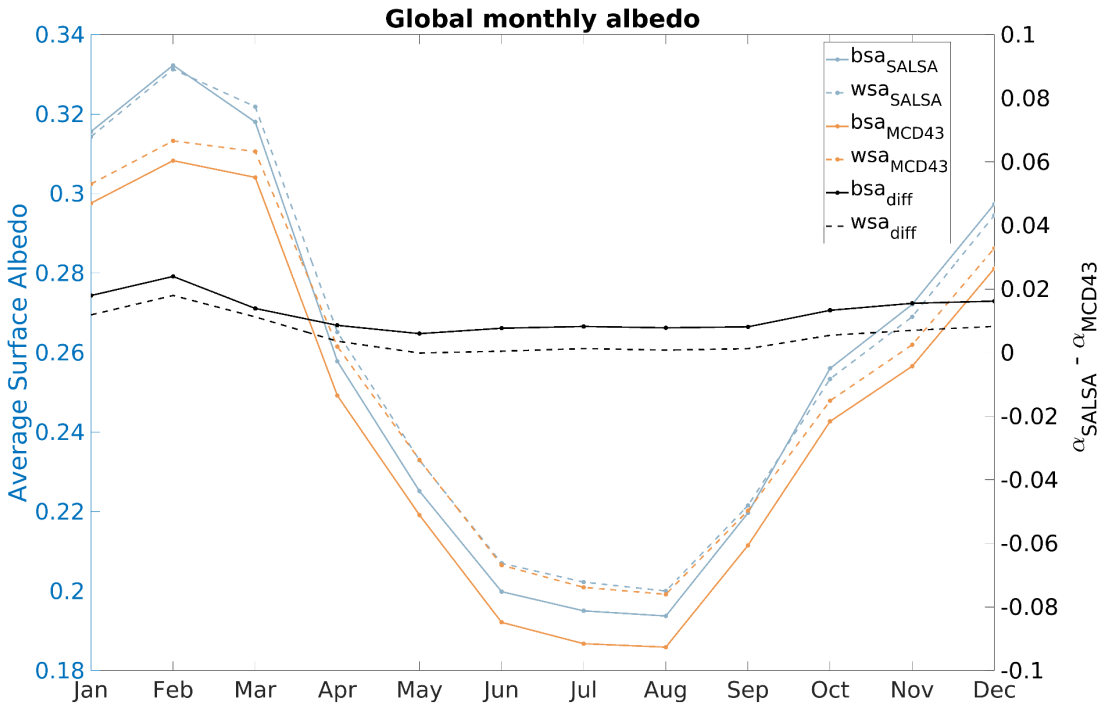

Figure 40: Comparison between the global monthly albedos of the SALSA and MCD43C3 products. The SALSA product is shown in blue, the MCD43C3 product is shown in red and the difference between them is shown in black (right axis). The solid lines represent the White-sky albedo, while the dashed lines represent the Black-sky albedo.

These results show that, firstly, the evolution of both Black-Sky and White-Sky albedos over the year is similar in both products, with higher values occurring in the winter months, and lower values in the summer months. Secondly, the difference between SALSA and MCD43C3 are highest in the winter months, with biases of up to 0.02, due to the presence of snow and the uncertainties of snow albedo retrieval. The difference between the products is especially high for the Black-sky albedo. This happens because Black-sky albedo depends on the solar zenith angle. Since the NOAA and MODIS satellites have different overpass times, this translates into a difference in the solar zenith angle of each observation, which leads to a bias. The differences between the products in the summer for White-sky albedos is very close to zero, since the biggest

sources of error are not present, namely snow albedo retrieval and solar zenith angle difference.

These conclusions are consistent when analyzing the Accuracy, Precision, Uncertainty, and r^2 values, as shown in Figure 41. The largest accuracy, precision and uncertainty values occur in the winter months and for the Black-sky albedos, while the lowest ones occur for the summer. Nonetheless, these results show a good seasonal behavior of the SALSA product when compared to the MCD43C3 product.

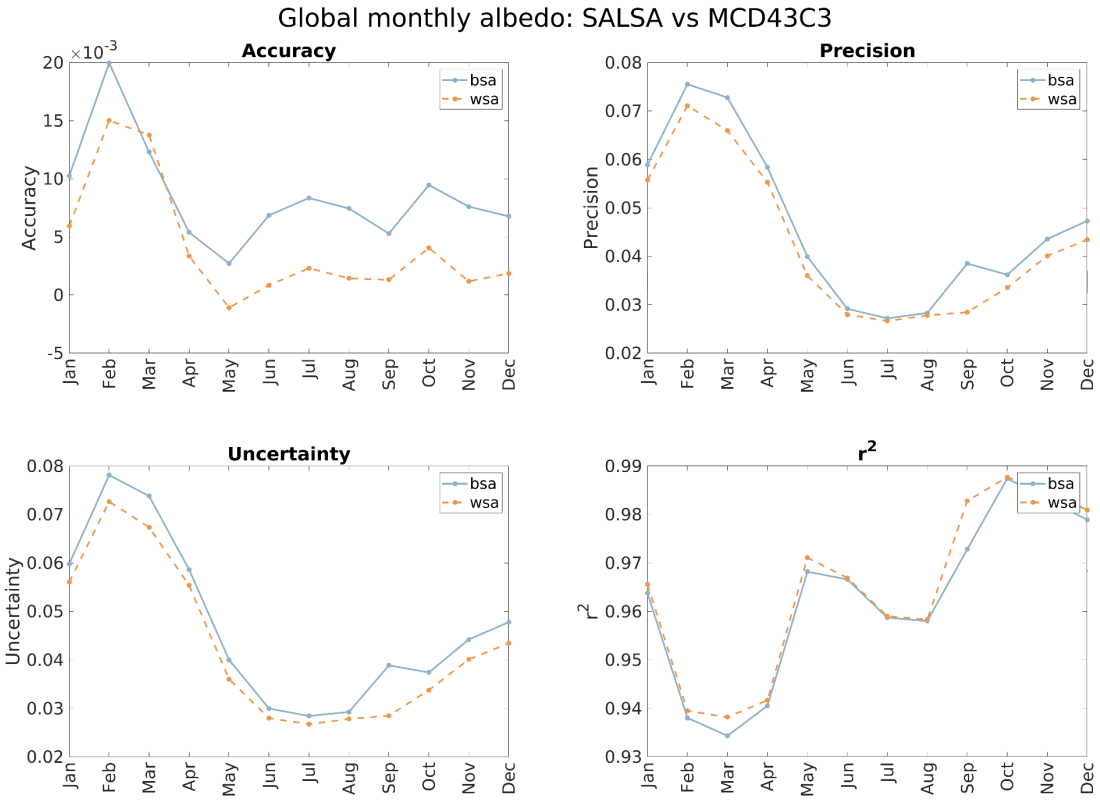

Figure 41: Comparison between SALSA and MCD43C3 products for the global seasonal averages from 2000-2018 by means of the Accuracy, Precision, Uncertainty and r^2 parameters. The orange line represents the White-Sky albedo, while the blue line represents the Black-Sky albedo.

5.1.3. Satellite average

In this section, I compare the performance of the AVHRR sensors aboard the different NOAA satellites, which are coincident with the MODIS sensor in the period 2000-2018. These include NOAA-14, 16, 18 and 19. Figure 42 shows their Accuracy, Precision, Uncertainty and r^2 values when compared to MCD43C3. The blue line represents the Black-sky albedo, while the orange line represents the White-sky albedo. These results show, firstly, that the performance of the SALSA product using NOAA16-19 is of good quality for both albedo types, with Accuracy values close to zero (<0.005), and Precision and Uncertainty values below 0.03. The correlation is also very close to one. The performance of the SALSA product when using NOAA14, however, presents some issues. It is important to note that only 249 days coincide between NOAA14 and MODIS Terra. Moreover, in this year, NOAA14 suffers from the effect of a very large orbital drift, where the change in Solar Zenith Angle can reach up to a 23^0 difference from the first years of the satellite (Ji and Brown, 2017). The effect of the orbital drift is quite evident especially on the Black-Sky albedo, where the uncertainty reaches values of up to 0.08. This happens because Black-Sky albedo inherently depends on the Solar Zenith Angle. In theory, this effect should not be visible in the White-sky albedo, which integrates over all illumination conditions, and therefore should not depend on the Solar Zenith Angle. However, as the data shows, the effect in the White-sky albedo, while significantly lower, is still notable. This could have to do with errors in the BRDF modelling or with the fact that the LTDR data does not account for atmospheric aerosols or water vapor. This can lead to spurious results

whenever these values change from MODIS overpass time to the NOAA14 overpass time (Nagol, Vermote and Prince, 2014).

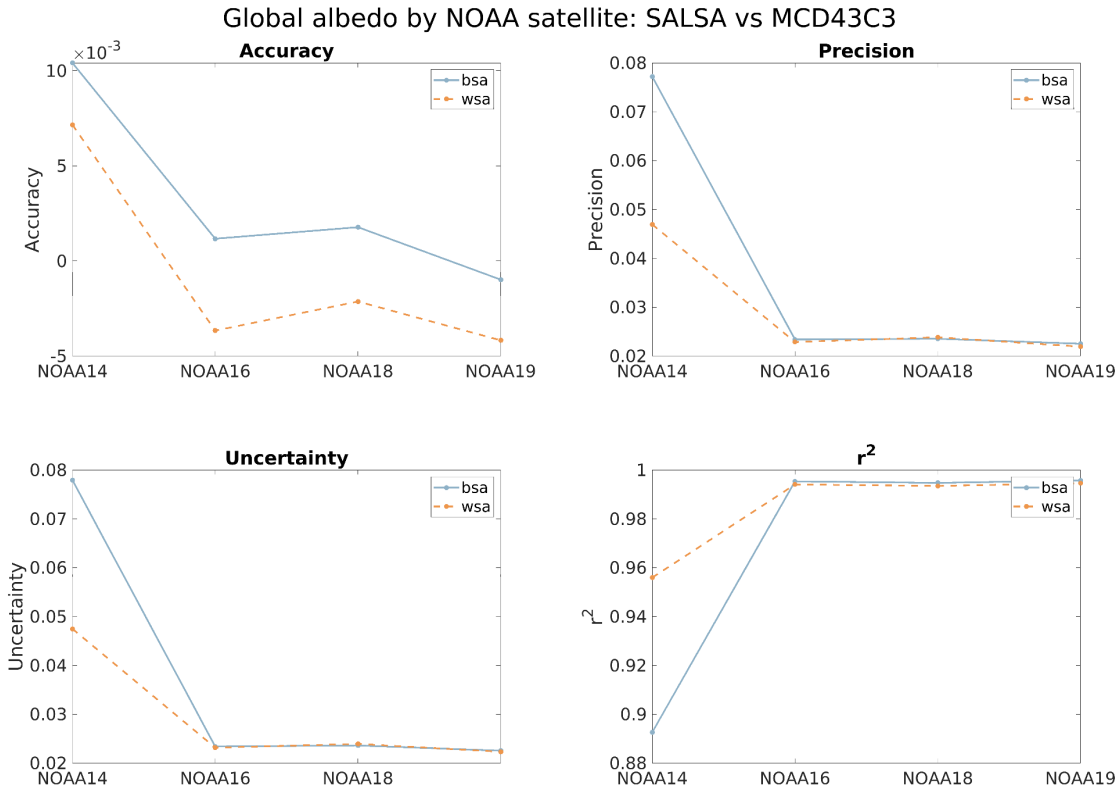

Figure 42: Accuracy, Precision, Uncertainty, and r^2 values of the global albedo for each NOAA satellite coincident with the MODIS sensor. Orange lines represent White-sky albedo, while blue lines represent Black-sky albedo.

5.1.4. Biome averages

In this section, I compare both products for the different biomes present around the Earth, in order to analyze for what biomes the SALSA product can be deemed acceptable, and for which ones it needs improvement. In order to do this, I first obtained the pixel average from 2000-2018, similarly to section 5.1.1. I then determined the actual biome present in the average pixel by downloading the yearly images from the MCD12C1 product. This is a combined MODIS Terra + Aqua Land Cover product that

identifies the primary land cover of all pixels in a CMG grid in a certain year for 17 different classes defined by the International Geosphere-Biosphere Program (IGBP) (Strahler *et al.*, 1999). Since the average of the pixels used for this study covers 18 years, during which the land cover could have changed on a certain pixel, I downloaded the MCD12C1 product for the 18 years and selected the mode land cover of each pixel to use as their final tag. Figure 43 shows the map of the mode. The association between the number and the name of the biome is shown in Table 21.

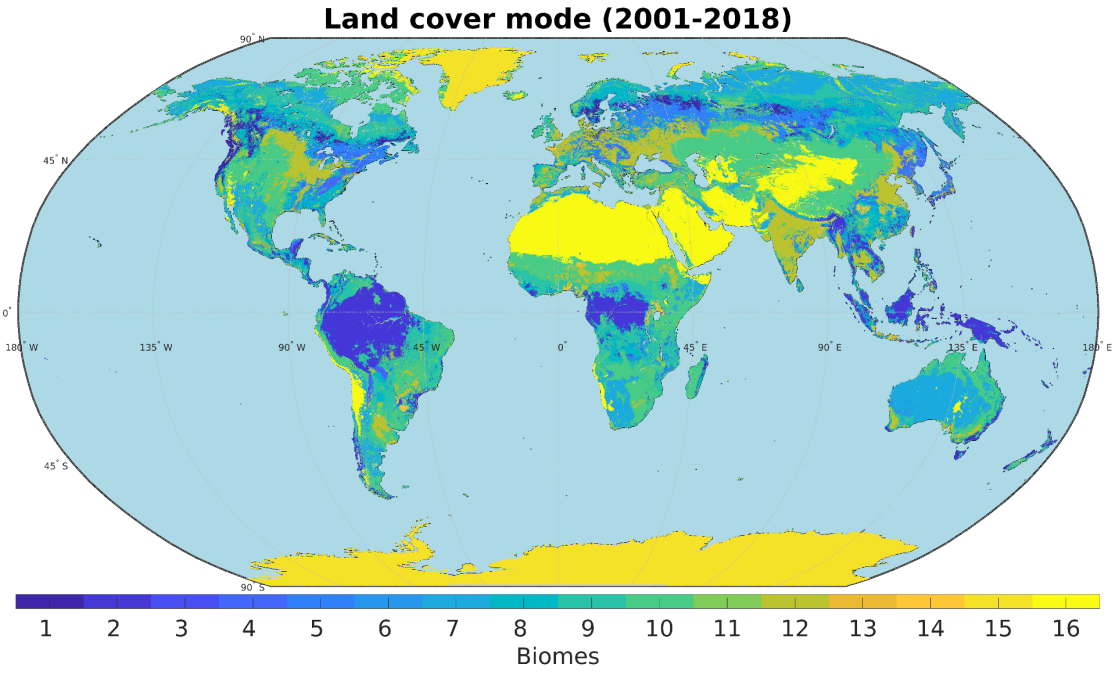

Figure 43: Mode land cover from 2001-2018 using the MCD12C1 product. Each number represents a different biome, as specified by Table 21.

For simplicity purposes, the biomes were regrouped into seven different classes, as shown in the last column of Table 21.

Table 21: The first two columns show the IGBP number and its associated biome. The third column shows how these were grouped into a new category with less biomes.

IGBP num.	Biome	New Biome
1	evergreen needleleaf forest	Forests
2	evergreen broadleaf forest	
3	deciduous needleleaf forest	
4	deciduous broadleaf forest	
5	mixed forests	
6	closed shrubland	Shrublands
7	open shrublands	
8	woody savannas	Savannas
9	savannas	
10	grasslands	Grasslands
11	permanent wetlands	
12	croplands	Croplands
13	urban and built-up	-
14	cropland/natural vegetation mosaic	Croplands
15	snow and ice	Snow
16	barren or sparsely vegetated	Desert

The comparison between SALSA and MCD43C3 for the new biomes is shown in Figure 44. These results show that the Accuracy, Precision and Uncertainty values, remain consistently low (< 0.02, < 0.03 and <0.03, respectively) for all biomes considered, with the highest absolute values happening for snow, and highest relative values for forests. The White-sky albedo provides a better accuracy, but slightly lower precision. In terms of correlation, however, the results show a particularly small r^2 value when comparing forest values. This difference in performance has to do with two main factors. Firstly, equatorial forests tend to be masked by a high cloud cover percentage. This means that there is a limited number of observations with which to build an accurate BRDF model. This means that the comparison done in those pixels

likely has high uncertainty values in both datasets. Secondly, high latitude coniferous forests tend to have a combination of snow and vegetation over the year. Differences in how the snow-covered vegetation is modelled and how the snow is detected between the algorithms increases the discrepancy between both datasets.

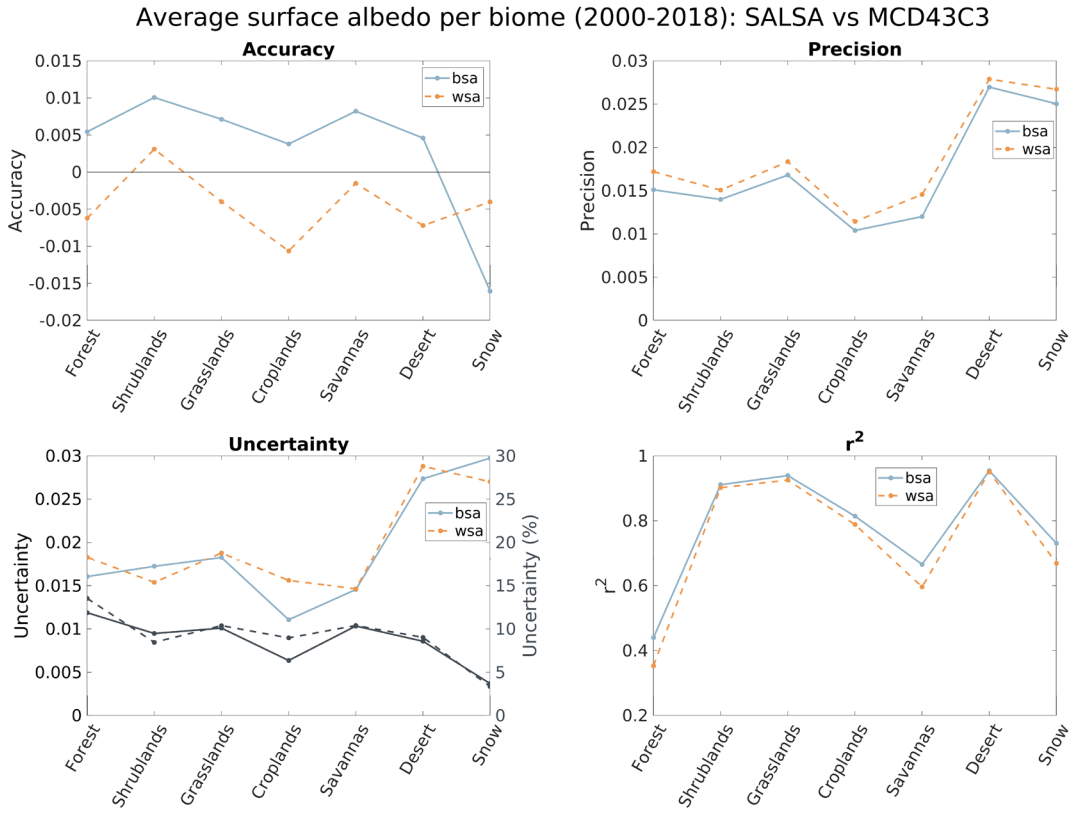

Figure 44: Accuracy, Precision, Uncertainty and r^2 of the grouped biomes shown in Table 21. Blue lines represent Black-sky albedo, while orange lines represent White-sky albedo.

5.1.5. Trends Comparison

In this section, I attempt to replicate the results from (Zhang *et al.*, 2010), who used MCD43C3v005 data to compute White-Sky albedo trends from 2000-2009, by both using MCD43C3v006 and the SALSA product. The main results from (Zhang *et al.*, 2010) were described in section 1.4.4. In order to do this, I first followed several steps.

Firstly, I produced a monthly SALSA product by averaging the data points in each month from 2000-2009, in order to reduce the number of data points while making the data less bound to outliers and more robust. This monthly product was then used to obtain a global, northern hemisphere and southern hemisphere time-series, as shown in Figure 45. The behavior of the monthly product is similar to that described in section 5.1.2, when analyzing the seasonal average. The biggest differences occur in the winter, where differences in snow detection and uncertainties in the snow albedo retrieval lead to the largest discrepancies for the White-sky albedo, while the lowest differences occur in the summer months.

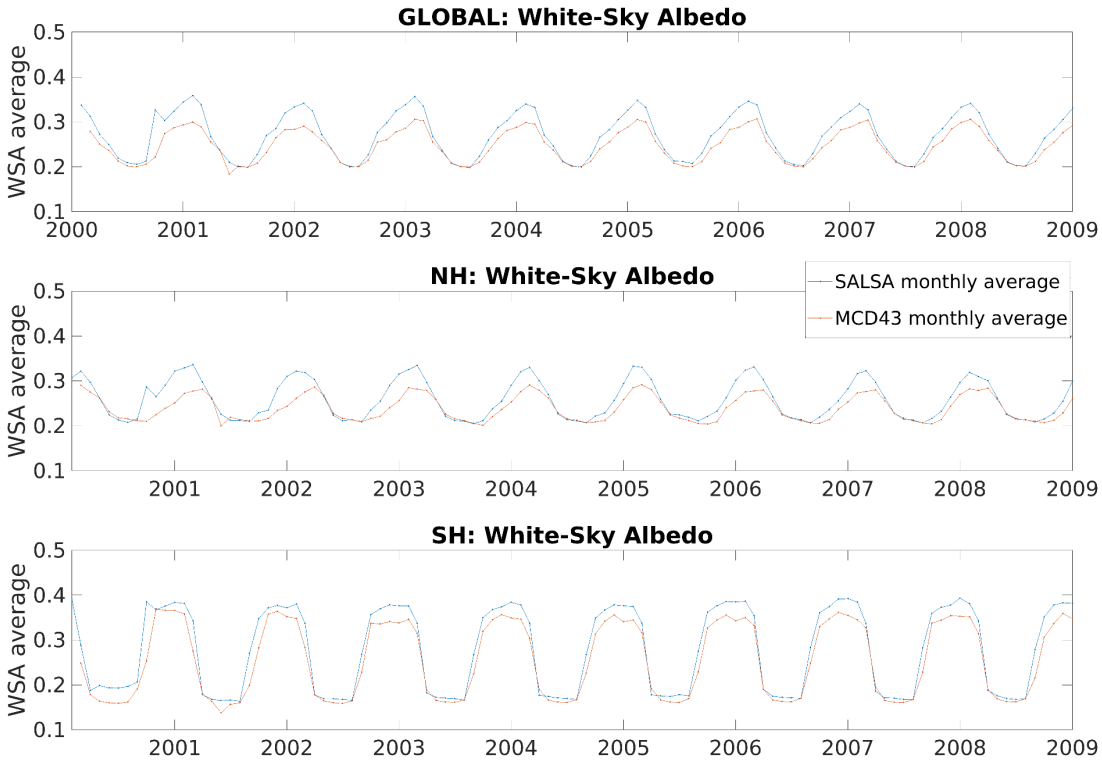

Figure 45: Global (top), Northern Hemisphere (middle) and Southern Hemisphere (bottom) White-sky albedos from the monthly SALSA product.

Secondly, I calculated the averages of every month – that is, the average of every January from 2000-2009, of every February from 2000-2009 and so on. This is done to calculate the deseasonalized monthly albedo anomalies ($\Delta\alpha(yy, mm)$), following Equation 44:

$$\Delta\alpha(yy, mm) = \alpha(yy, mm) - \bar{\alpha}(mm) \quad (44)$$

where $\alpha(yy, mm)$ is the monthly mean albedo in the year "*yy*" and month "*mm*", and $\bar{\alpha}(mm)$ is the average from 2000-2009 of month "*mm*".

Finally, I calculated the trends of the deseasonalized anomalies to estimate the change in surface albedo for this time-period. The trend's significance was calculated using the non-parametric Mann-Kendall test, which has been widely used in the literature (Mann, 1945; Unganai and Kogan, 1998; Dorigo *et al.*, 2012; Sobrino and Julien, 2016). The slope was calculated using Theil-Sen estimator (Sen, 1968), which is a non-parametric method insensitive to outliers and computationally very efficient (Wilcox, 2010). Figure 46 shows the Global (top), Northern Hemisphere (middle) and Southern Hemisphere (bottom) White-sky deseasonalized albedo anomalies from the monthly SALSA product. The blue colors represent the SALSA product, while the orange color represent the MCD43 product. The thin line shows the monthly anomalies, and the thick line shows the yearly averages of said anomalies. The slope and its uncertainty are displayed in the top left corner of each plot. Values showing zeros on both indicate that no statistically significant slope was found to the 10% level. The slope represents the change of White-sky albedo per decade.

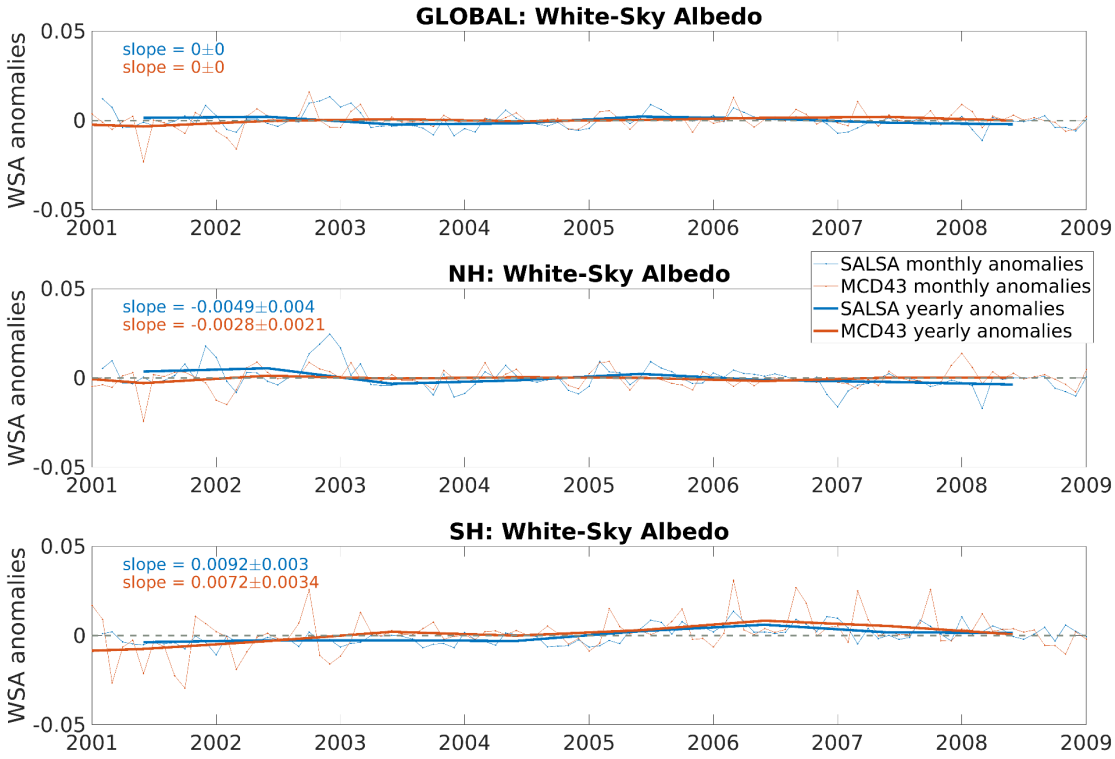

Figure 46: Global (top), Northern Hemisphere (middle) and Southern Hemisphere (bottom) White-sky deseasonalized albedo anomalies from the monthly SALSA product. The blue colors represent the SALSA product, while the orange color represent the MCD43 product. The thin line shows the monthly anomalies, and the thick line shows the yearly averages of said anomalies. The slope and its uncertainty are displayed in the top left corner of each plot. Values showing zeros on both indicate that no statistically significant slope was found to the 10% level.

The results show that, firstly, the estimation of the trends for both products is quite similar, especially for the Southern Hemisphere. In both hemispheres, the decadal trends lie within one sigma of each other. In the case of the global albedo, they both show statistically insignificant results to the 0.1 level. Secondly, the results are consistent in sign with the results displayed in (Zhang *et al.*, 2010), who estimated an increase in the Southern Hemisphere of ~0.01, and a decrease in the Northern Hemisphere of ~-0.01. In the former, the results match in sign and magnitude, while in the latter, only in sign.

5.2. SALSA product analysis

5.2.1. Global average trends

In this section, I will compute global, Northern Hemisphere (NH) and Southern Hemisphere (SH) averages from 1982-2018. To do so, the same approach as for section 5.1.5 was carried out, instead, using a yearly SALSA composite. First, the global, NH and SH averages were obtained by applying the cosine conversion to ensure an equal-area projection and averaging over the relevant pixels. This provides three vectors with 37 elements each. Second, yearly anomalies were calculated for each of these three and trends were derived from them using the Mann-Kendall test for significance, and the Theil-Sen's slope for the slope estimation. Once again, the White-sky albedo was favored over the Black-sky or Blue-sky albedo, as this value is independent of the solar zenith angle and therefore represents a better estimate of the intrinsic property of the surface. Finally, the value of the slope was multiplied by 10, to represent the decadal White-sky albedo change.

Figure 47 shows the global (top), Northern Hemisphere (middle) and Southern Hemisphere (bottom) trends for White-sky albedo. The thin lines show the monthly product, while the thick lines show the yearly product. Blue lines represent the SALSA product, while red lines represent the MCD43 product. Slopes with their uncertainties and p-values are shown in the top left of each plot. The uncertainty is calculated from the 95/5 percentiles of the individual slopes in the Theil-Sen's slope estimation (Toutenburg, 1975). The slopes from the MCD43 product are obtained for the period (2000-2018) only.

The results show a stable performance of the SALSA product over the whole time-series for the global average and NH, but shows some remnant effect of the orbital drift effects in the SH. This can be seen in the monthly averages for the years with the highest orbital drift: 1988, 1994, 2000 and 2018. The yearly product shows how there is a constant difference in average values between the SALSA and MCD43 products, similar to that shown in sections 5.1.5 and 5.1.2. This effect was already observed when computing surface albedo for AVHRR data, where weaker cloud detection ability of the AVHRR sensors makes it more likely for cloud pixels to be misidentified as snow/ice pixels at high latitudes ($>50^0$), leading to overestimation of surface albedo (Key *et al.*, 2001; Karlsson *et al.*, 2013; He, Liang and Song, 2014).

The study of the global 37-year White-sky albedo trends using the SALSA product, reveals a slightly negative statistically significant ($p < 0.1$) decadal trend, of -0.00078 ± 0.00056. This value is very close to zero, indicating no long-term change. This value is within one sigma from the GLASS surface albedo from 1982-2010, which reported a trend of -0.0013 per decade (He, Liang and Song, 2014). Trends for a similar period using the Global Energy and Water Exchanges project (GEWEX) and the International Satellite Cloud Climatology Project (ISSCP), showed steeper negative trends of -0.0053 and -0.0086 per decade, respectively.

The trend from 2000-2010 calculated using the MCD43 product, however, shows a slight increase in the surface albedo value for that period, which is strongly influenced by the SH changes of 0.0045 per decade. The trends for the NH and SH using the SALSA product show also a slightly negative value, though with a statistically non-

significant value. The uncertainty is too large for us to tell whether these trends are slightly positive or slightly negative.

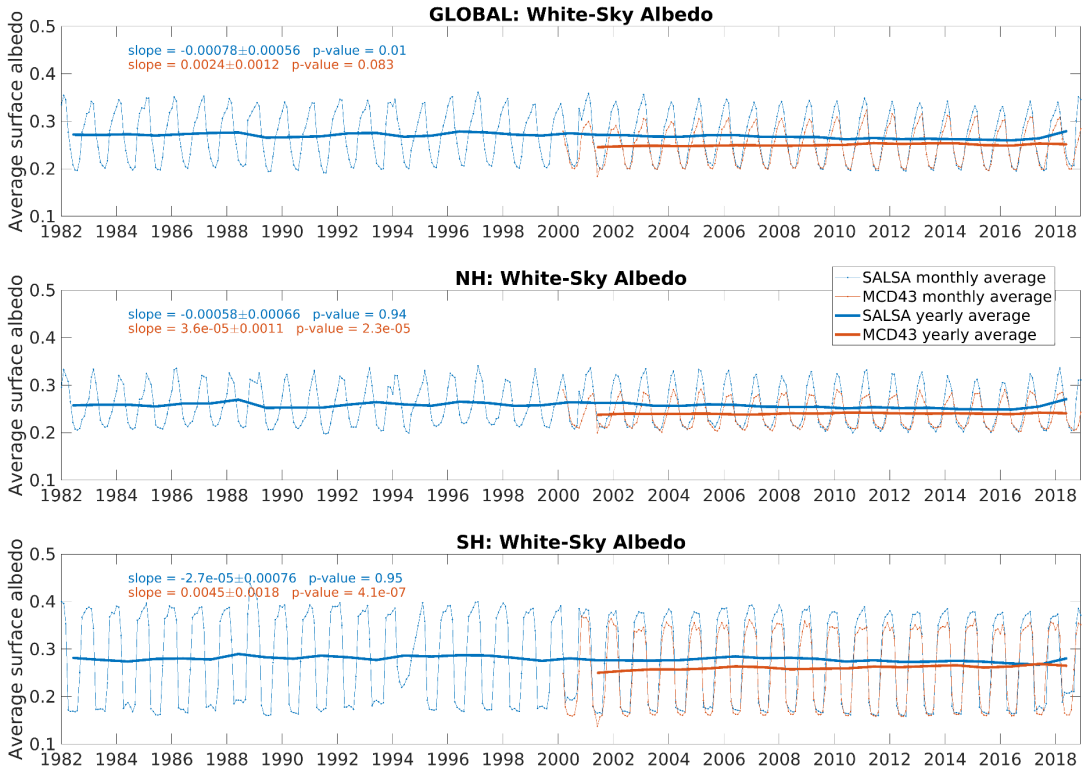

Figure 47: Global (top), Northern Hemisphere (middle) and Southern Hemisphere (bottom) decadal trends for White-sky albedo. The thin lines show the monthly product, while the thick lines show the yearly product. Blue lines represent the SALSA product, while red lines represent the MCD43 product. Slopes with their uncertainties and p-values are shown in the top left of each plot.

5.2.2. Trends per pixel

The comparison with the MCD43C3 revealed some issues in the SALSA product that could hinder the ability to extract reliable per pixel trends. First, there are differences in snow detection between NOAA satellites before and after the year 2000, mostly due to significant trends and uncertainties in the thermal calibration of AVHRR radiometers before NOAA-15 (Trishchenko *et al.*, 2002). These effects lead to large average differences in high latitude pixels between the first half (1982-2000) and the second

half (2001-2018) of the dataset, which in turn yield spurious trends in surface albedo. In order to tackle this issue, I calculated the monthly deseasonalized anomalies for the two periods separately. Since the values from which the trends will be calculated are now deviations from the mean, the actual mean difference between the two periods will have no effect in the slope.

Second, the orbital drift mentioned in section 5.1.3 could also modify the long-term surface albedo trends, so long as two conditions are met: 1) the solar zenith angle (SZA) has a trend component, and 2) there is a high correlation between the SZA and the White-sky albedo for a certain pixel (Ji and Brown, 2017). If both conditions are true, the trends will rely unreliable values for that pixel. However, if only one of them is true, the trend will likely not suffer any effects. If the solar zenith angle has a trend component, but there is low or statistically non-significant correlation between the SZA and White-Sky albedo, this means that the latter does not depend on the former. Similarly, if there is high correlation between the variables, but the SZA induces no trend into the data, whatever trend is detected, cannot be an artifact of the SZA, and would reflect the evolution of the White-sky albedo. For this reason, before computing the per pixel long-term trends for the SALSA product from 1982-2018, I identified what pixels satisfy both conditions. The results are shown in Figure 48.

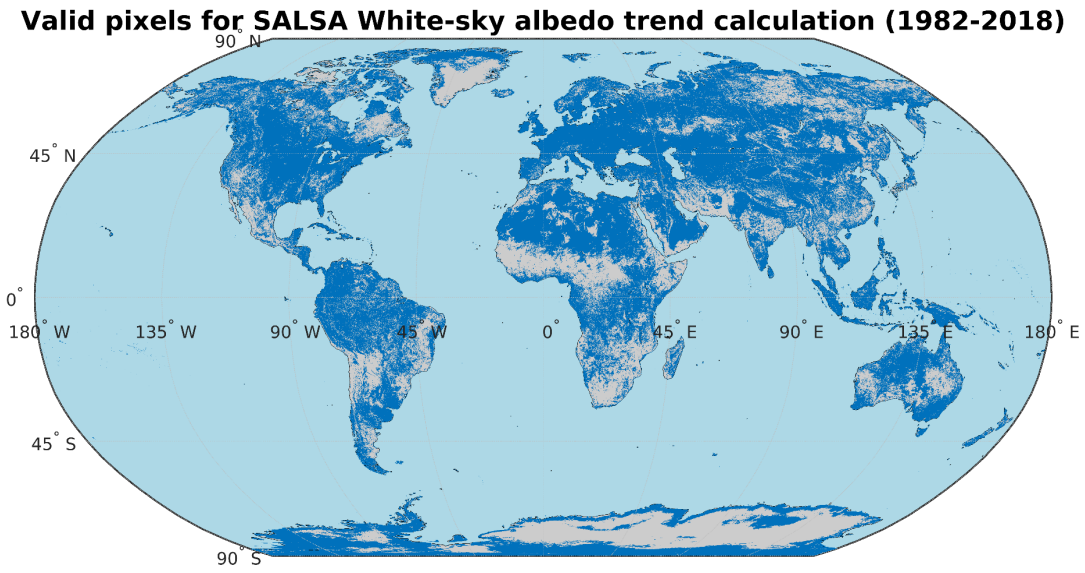

Figure 48: Pixels that satisfy conditions 1) and 2) specified in this section for reliable trend calculation from 1982-2018. Dark blue pixels represent these values, while grey, light blue represent non-valid, and water pixels, respectively.

In order to compute the global trends, the same approach as the previous section was used. This means that every pixel has 37 data points to determine their surface albedo evolution. The results are shown in Figure 49. Figure 50 shows the standard error of the slope associated with each pixel, and Figure 51 shows the statistically significant pixels to the 10% level. The highest uncertainties in the slope retrieval occur especially around high northern latitudes.

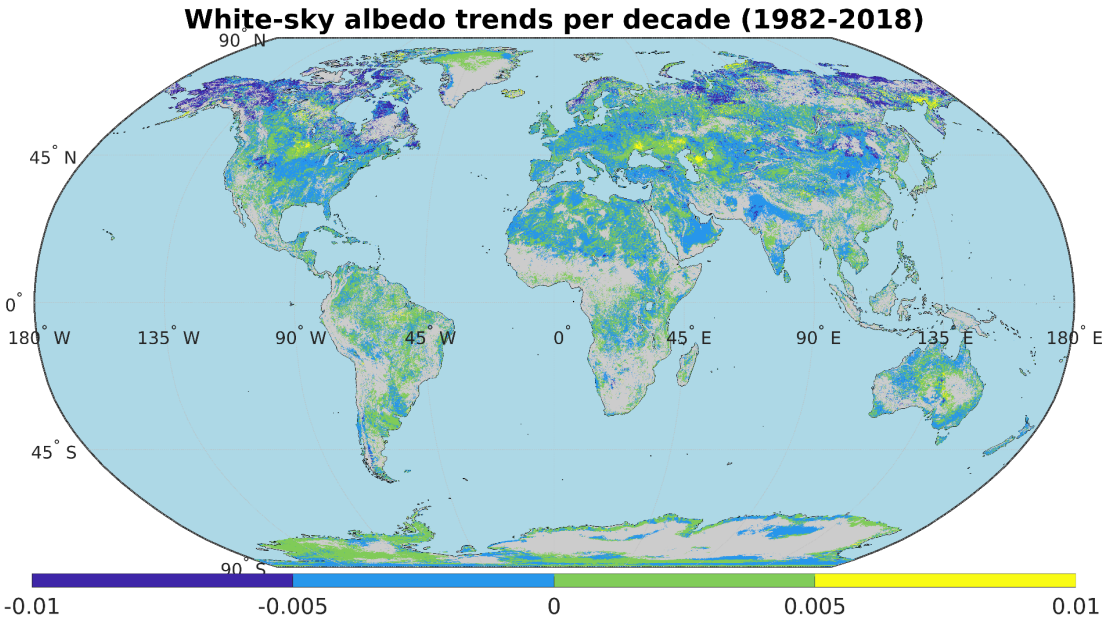

Figure 49: White-sky albedo trends per decade from 1982-2018.

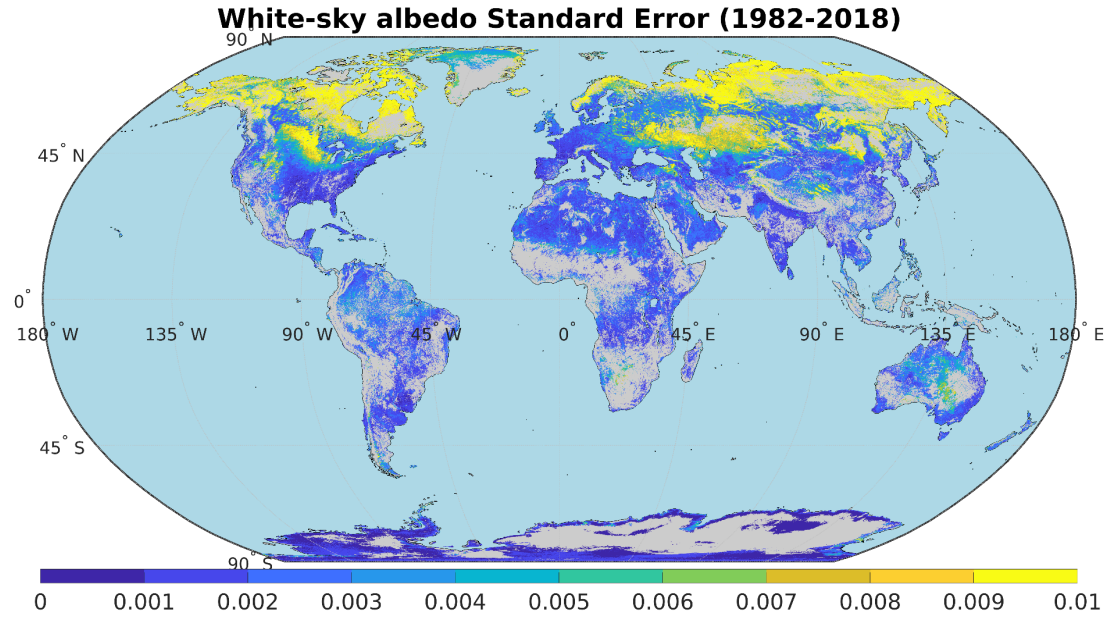

Figure 50: Standard Error of the White-sky albedo trends derived from 1982-2018.

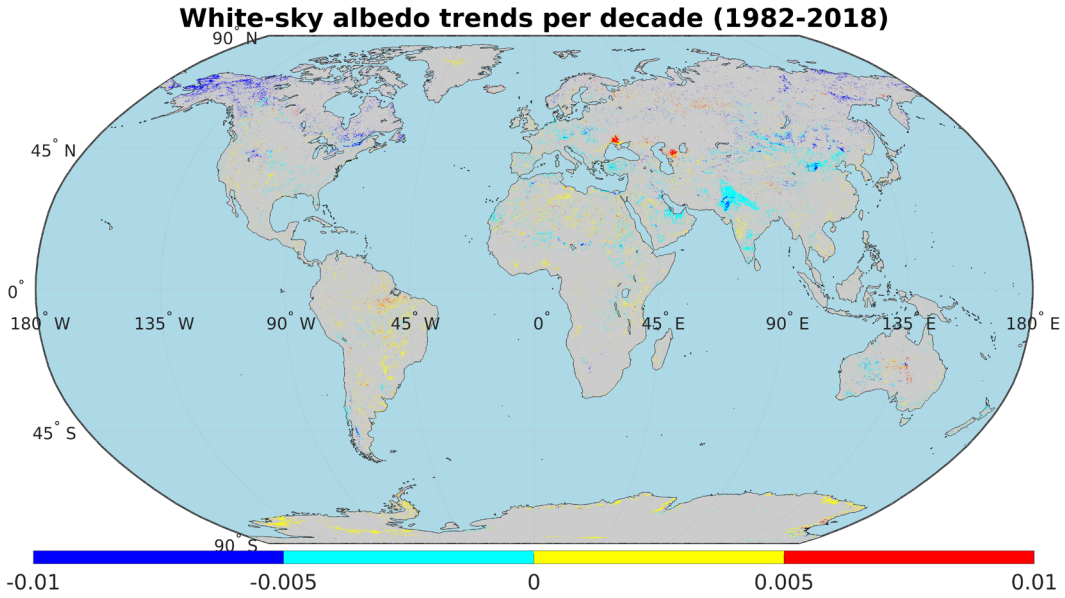

Figure 51: Statistically significant White-sky albedo trends per decade (1982-2018).

The majority of the trends shown are accounted for in the literature: In South America, trends derived from 1982-2018 show an increase in surface albedo for the Amazon forest. The effect of deforestation on surface albedo and radiative forcing is well known, and has been the focus of many studies in the literature (Gash and Shuttleworth, 1991; Myhre *et al.*, 2013; Lejeune *et al.*, 2015; Querin *et al.*, 2016; Faria *et al.*, 2018). The lowest values in South America are found near snow-covered mountains, where there is growing evidence that high-mountain environments experience more rapid temperature changes that lead to early snowmelt and decrease in albedo (Pepin *et al.*, 2015). In North America, the forests in the Western United States are suffering from increasing stress from insects, wildfires, heat and droughts due to regional warming, which lead to increases in surface albedo (Mantgem *et al.*, 2009), while in eastern United States, the decreasing albedo is related to forests that are recovering from historical disturbances or are under intensive forestry management (Birdsey, Pregitzer

and Lucier, 2006). Finally, in higher latitudes, warming is leading to woody vegetation growth in Northeastern Siberia, Western Alaska, Greenland's borders and Northern Quebec, which in turn decreases the surface albedo (McManus *et al.*, 2012).

In Africa, decreasing albedo trends are found in the Sahel, where field observations and satellite data have confirmed that this region is experiencing re-greening led by increases trends in precipitation (Govaerts *et al.*, 2008; Dardel *et al.*, 2014). Positive albedo trends in the Sahara desert have not been observed before, and are typically reported as zero or very close to zero. It is possible that, since the LTDR product has no aerosol retrieval, and the concentration of aerosols is highest near deserts, the trends are related to trends in Aerosol Optical Thickness (AOT) and not to White-Sky albedo. The same phenomenon is observed in Saudi Arabia.

In the Eurasian territory, increasing surface albedo trends in Ukraine and Kazakhstan can be attributed to a decreasing soil moisture trend, caused by a natural atmospheric variability (Dole *et al.*, 2011). Decreasing trends in Europe are associated with an increase in tree canopy, which has experienced the highest tree canopy gain of all continents (Song *et al.*, 2018), while in India and Pakistan, the negative trends are due to a rainfall increase, which leads to increased soil moisture, caused by the intensification of the monsoon circulation from the El Niño Southern Oscillation (ENSO). Finally, in Australia, the positive trends in the central region were also observed by several other studies (Zhang *et al.*, 2010; Chrysoulakis, Mitraka and Gorelick, 2018), and are attributed to the 'Big Dry'; a severe drought predominantly driven by the Indian Ocean Dipole (Ummenhofer *et al.*, 2009).

5.2.3. Impact of period length on albedo trends

In the introduction of this document (section 1.2), I exposed the current GCOS requirements for long-term surface albedo datasets, that require at least a temporal coverage of 30 years, since less than this period is a short time for climate change purposes cannot allow us to separate long-term trends from inter-annual and decadal variability in a reliable way (Trenberth *et al.*, 2006; Yang *et al.*, 2013b; Qu *et al.*, 2015; GCOS-200, 2016) . The goal of this section is to analyze the impact of the period length in the value of the slopes of White-sky albedo, and to study their behavior as this period varies.

In order to do this I first selected seven different periods with which to calculate the trends. The specific years used for each period are shown in Table 22. Next, I calculated the correlation coefficient between the White-sky albedo and the SZA for the global yearly product, and removed those pixels with a value greater than 0.1, in order to eliminate trends likely due to the SZA and not the White-sky albedo evolution. The trends were then calculated using the Theil-Sen's slope method for the seven different periods for all land pixels. Figure 52 shows the boxplot of the global distribution of trends for each period considered. The red line represents the median; the blue borders are the lower (Q1) and upper (Q3) quartiles. Blue dots show the outliers, which lie beyond the limits, marked with a black line, calculated using 1.5*(Q3-Q1).

Table 22: Years and period length used in this study.

Years	Period length
2006-2011	5
2001-2010	10
2001-2015	15
1996-2015	20
1991-2015	25
1985-2015	30
1982-2018	37

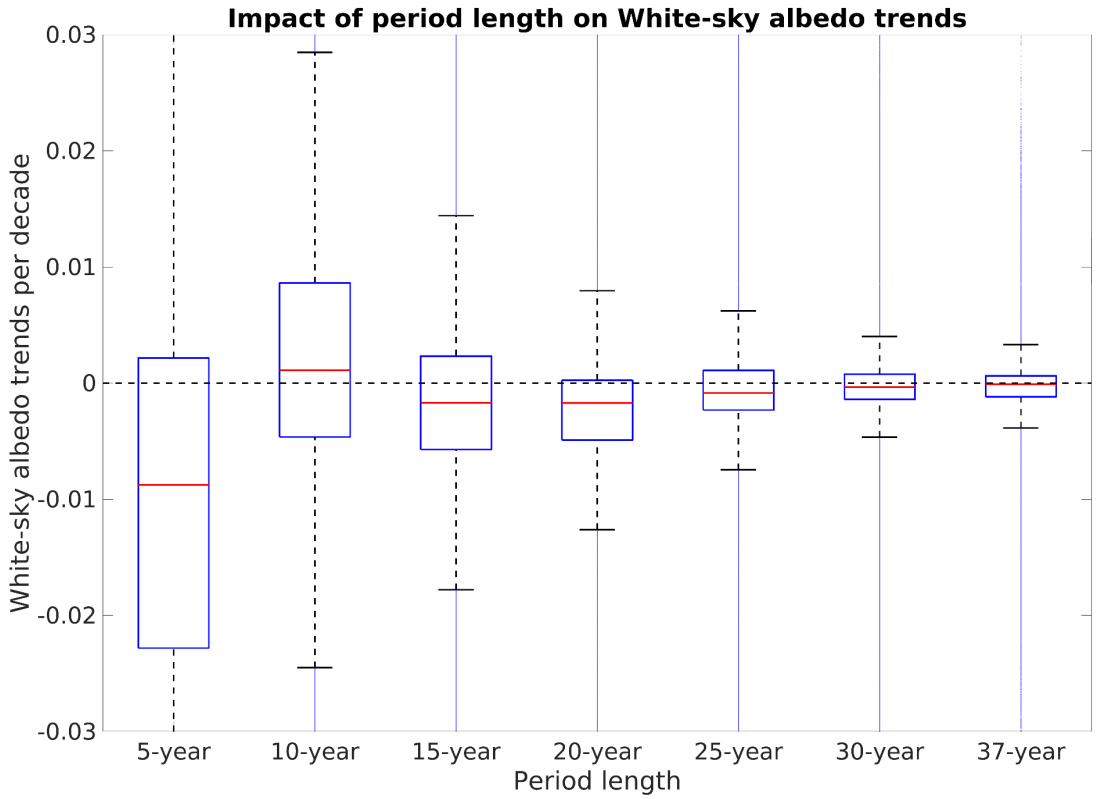

Figure 52: Boxplot of the global distribution of trends for each period considered in this study. The red line represents the median; the blue borders are the lower (Q1) and upper (Q3) quartiles. Blue dots show the outliers, which lie beyond the limits, marked with a black line, calculated using 1.5*(Q3-Q1).

These results show firstly, that the longer the period considered for the trend computation, the more the average value approached zero. The difference between the 5-year and 37-year average is ~0.01. This is a significant difference, considering that studies show using climate models that a global surface albedo trend of 0.01 could yield

a temperature difference of around 2K (Akbari, Damon Matthews and Seto, 2012). The standard deviation of the distribution, vaguely associated with the box width, also becomes smaller as the period increases. The period length, therefore, has a big impact on the distribution of White-sky albedo trends across the globe. The overall long-term global change is close to zero, as demonstrated in section 5.2.1, and studies using a shorter period, could yield unreliable conclusions of the long-term surface albedo evolution. At 30 years of period length, the decadal albedo trends are already very close to zero, pointing towards the need for greater than 30 years for the computation of global surface albedo changes.

5.3. Conclusions

In the first section, of this chapter, I compared the SALSA product, obtained after the steps shown in the previous chapter, and compared it to the well-calibrated and widely used MCD43C3v006 product. The comparison was performed in an extensive manner, analyzing the differences in temporal averages, seasonal averages, and differences per biome, satellite and trend computation. These studies revealed some of the strengths and weaknesses of the SALSA product. The product showed a very good agreement on land pixels, across different biomes and satellites. However, it revealed the impact of that the orbital drift effects have on the White-sky albedo retrieval, along with the limitations present in the snow algorithm retrieval.

In the second section, I used the SALSA product to reveal the evolution of surface albedo from 1982-2018, in terms of global averages and in a per pixel basis. The results showed that the overall surface albedo has not been changing significantly for this period, with an order of magnitude of 10^{-4}, and is therefore very close to zero. Zonal

changes, however were analyzed, and revealed similar geographical patterns as other studies in the literature, which analyzed trends using a shorter period. Finally, a short study analyzing the impact of the period length on the global distribution of White-sky albedo trends evidenced that the longer the period used to estimate said changes, the closer these approach 0, highlighting the importance of using more than 30 years to estimate this parameter.

Chapter 6: Summary of findings and conclusions

6.1. Summary of findings

The main goal of this dissertation was to create a global surface albedo dataset that follows the requirements set by the GCOS, described in detail in section 1.2, and to answer the research questions posed in section 1.5. In order to do so, several steps were required, which are described in detail throughout chapters 2-5, and establish the core of this dissertation's methodology.

The LTDR product is composed by a set of AVHRR sensors aboard different NOAA satellites, all with slightly different spectral characteristics. The need to spectrally harmonize surface reflectance values from these sensors led to the first scientific question:

1. What are the strategies and associated uncertainties related to the harmonization of the LTDR products for the different NOAA satellites?

In chapter 1, I proposed a methodology to address this issue and cross-calibrate all of these sensors, through a novel spectral adjustment method. Results using simulated data showed that the application of an exponential model for the red band, and a multilinear model for the NIR band significantly improved the Accuracy, Precision and Uncertainty of the cross-calibration, virtually eliminating the effect of the spectral differences between the different sensors in the LTDR product.

Once the data was set to a common radiometric scale, a reliable clear, cloud and snow mask was needed for the LTDR product, which is described in detail in Chapter 2. The need for this step has to do with the fact that different models were used for the retrieval

of surface albedo over clear land and snow pixels. Using a model meant for land surface albedo retrieval applied over snow covered surfaces (or vice versa), leads to unrealistic and inaccurate values. In order to discriminate between these three classes, I developed the MODIS-based AVHRR Class Separation Algorithm (MACSSA). This algorithm combines optical and thermal information from MODIS data, along with reanalysis information and monthly climatology to create a Support Vector Machine (SVM) model. This model sets linear thresholds between all the input data to separate between the three classes. The results showed that the MACSSA algorithm provides a probability of detection of clear and snow pixels of ~97% and ~88%, respectively, making it applicable to the LTDR product on a global basis.

With reliable information about the surface type, the next step is to calculate surface albedo. Two different approaches were used for clear and snow pixels. Clear land surface albedo was obtained through the integration of the Bidirectional Reflectance Distribution Function (BRDF) of the surface being observed by the satellite. The modelling of this shape typically requires an 8-16 days composite, however, (Vermote, Justice and Breon, 2009b), developed a model (VJB) which estimates a target's BRDF shape using 5 years of observations and corrects for directional effects allowing the computation of land surface albedo on a daily basis through the use of the NDVI. The method was originally established on MODIS data but its viability and optimization for AVHRR data was not fully explored. This led to the second research question:

2. What is the optimum way of modelling the BRDF shape for the LTDR product to obtain surface albedo? How accurately can we calculate this for snow covered pixels?

In section 4.1, I analyzed different approaches to find the most robust way of applying the VJB correction to AVHRR data. The main findings of the study show that first, the model benefits from increasing the temporal composite from 5-years to 15 or more years, by decreasing the NIR and NDVI average noise by up to 7%. This greatly benefits the LTDR product, considering the length of the dataset. Secondly, a modification of the model using assumptions based on the nature of the model's parameters revealed that the average noise of the dataset decreased a further 9% in the red and NIR bands with respect to using the original model. These results directly answer the first half of the second research question, by optimizing the VJB model and allowing daily surface albedo estimation using AVHRR data. These BRDF shapes were then used to estimate Black-sky, White-sky and Blue-sky albedos.

The approach to obtain snow albedo was different, as described in section 4.2. The ability to accurately model the BRDF shape of snow using the AVHRR sensor is limited by the lack of critical bands to estimate the two main parameters that describe its shape: snow grain size and impurity content. For this reason, I obtained snow albedo using the MCD43 product as a reference. I used observations with less than 10-minute overpass time difference between MODIS Aqua and AVHRR to create random forest regression models that predict snow black-sky and white-sky albedos from AVHRR input bands. These models allowed me to retrieve snow albedo from the LTDR product

with a RMSE < 0.07 when using the AVHRR data with band 3B operational, and RMSE < 0.05 when band 3A was operational. These results can be applied on the LTDR product all around the world, ensuring less than 10% uncertainty in the retrieval, which answers the second half of the research question number 2.

The retrieved SALSA product was cross-compared to the MCD43C3 product in terms of temporal and seasonal averages, across different satellites and biomes, and in terms of trend estimation, in order to ensure the reliability and robustness of the product. The results in section 5.1 revealed a very good agreement on land pixels, across different biomes and satellites. However, it revealed the impact of that the orbital drift effects have on the White-sky albedo retrieval, along with the limitations present in the snow algorithm retrieval.

Once these questions were answered, and said methods were found, they were finally applied to the LTDR product to obtain the surface albedo trends. The final and main goal of this dissertation was therefore to use this product to create a long-term surface albedo dataset, which satisfies the GCOS requirements for temporal resolution and span of dataset. This led to the research question:

3. What are the global surface albedo trends since 1982? What is the impact of the data record length on the trends?

The results showed that the overall surface albedo has not been changing significantly for this period, with changes of the order of 10^{-4}, and is therefore very close to zero. Zonal changes, however, revealed similar geographical patterns as other studies in the

literature, which analyzed trends using a shorter period. Finally, a short study analyzing the impact of the period length on the global distribution of White-sky albedo trends evidenced that the longer the period used to estimate said changes, the closer these approach 0, highlighting the importance of using more than 30 years to estimate this parameter, and answering the second half of the last research question.

In terms of GCOS requirements, the SALSA product currently satisfies the length of the dataset of more than 30-years and the daily temporal resolution. This is one more than other similar products such as the C3S, or the GLASS product. In terms of accuracy and stability of the dataset, these quantities are only obtained in the context of a ground validation, which has not been performed in this dissertation. Other products using AVHRR however, report accuracy and stability values that do not satisfy the GCOS requirements (Liu *et al.*, 2013; Benhadj, 2018). Similar results are expected from this dataset. The question then remains whether it is realistically possible to satisfy these two requirements using AVHRR data, and if instead, we will have to wait until datasets that do satisfy these requirements, such as MCD43, cover 30+ years of observations, or until efforts on the harmonization of data from different satellites are increased.

6.2. Limitations

The methodology employed in computing the SALSA product comes with some limitations that were evidenced through the comparison with the MCD43 product.

First, the effect of the orbital drift is quite significant, especially on the Black-Sky albedo, which depends exclusively on the SZA. The average uncertainty when compared to MCD43 of the year with the highest orbital drift was of ~0.08, this is 3

times larger than the uncertainty when compared to other years where there was no SZA difference. This factor became only 2 times larger on the White-sky albedo, which is theoretically independent of the SZA, and should therefore not be affected by orbital drift effects. Rather, these differences are likely caused by the lack of water vapor and especially aerosol estimation, which has a direct impact in the quality of the atmospheric correction. These effects can affect the retrieval of long-term trends by providing spurious trends that are by SZA changes rather than surface albedo. To solve this issue, pixels with a high correlation between the White-sky albedo and the SZA, along with pixels whose SZA evolution evidenced a statistically significant trend, were removed and deemed unreliable.

Second, seasonal analyses of the SALSA product revealed biases in the retrieval of surface albedo for the winter months. This bias has been observed before on other AVHRR datasets, and is associated with cloud pixels being misidentified as snow pixels at high latitudes ($>50^0$), leading to overestimation of surface albedo (Karlsson *et al.*, 2013; He, Liang and Song, 2014). The magnitude of this bias was of ~0.02. The only step towards eliminating this bias is to improve the snow detection using AVHRR data, which is a challenging issue, given the nature of the AVHRR bands.

Third, the SALSA product used MCD43C3 as a reference for many of its steps. The assumption that this product represents the truth has its limitations. This product has been extensively validated, exhibiting a good accuracy and uncertainty, and is used as a reference for Global Climate Models (GCMs). However, it has been shown to underestimate snow albedo for high solar zenith angles (Stroeve *et al.*, 2005; Liu *et al.*, 2009). An analysis of the SALSA product over ground measurements or to different

surface albedo product would be of use to determine the quality and robustness of the dataset.

Another limitation of the SALSA product comes from the propagated noise of the raw dataset. Since there is no Water Vapor or AOT estimation for pixels before the year 2000, the noise, especially for the red band, is high (Villaescusa-Nadal, Franch, Vermote, *et al.*, 2019). This noise propagates into the broadband surface albedo, hampering the performance and usefulness of the daily temporal resolution.

Finally, this product makes use of several fully empirical methods, which are not based on physical models. This is the case, for example, of the snow albedo computation. These models make the reproducibility of the methodology problematic, since the result is very sensitive to the choice of the data used to build the model. A very large dataset is required to train the models, which often times results in high computational requirements, sometimes out of reach for the user.

6.3. Looking forward

The limitations present in this product immediately invite for improvements in the dataset that either eliminate or reduce the effects that these have on the quality of the final SALSA product.

The first and most important step to do next is to perform a comprehensive validation of the blue-sky or actual albedo (which is the closest quantity to the measured surface albedo in the ground). Recently, the Committee on Earth Observation Satellites (CEOS) published a document that provides recommendations for best practices to be used for the validation of global surface albedo products (CEOS, 2019). These include three main approaches: 1) Direct ground-truth validation, using tower-based

instruments on a spatially homogenous land cover, that can be representative of a coarse satellite derived observation. 2) Indirect validation via other satellite-derived albedo products and 3) Upscaling of pixel-to-pixel validation relying on high resolution airborne satellite surface albedo datasets to assess the satellite products at coarser spatial resolution. Following these practices, not only would it allow me to see the robustness and confidence of the model, but also provide values of accuracy and stability that can be compared to the GCOS requirements.

The second step is to attempt to improve the raw surface reflectance and thermal data that are used as an input for many of this product's steps. The high noise present in the bands propagates to the broadband surface albedo estimation. To solve this, reanalysis data at a similar spatial resolution could be used to complete the information. This would not only solve issues with the noise, but also minimize the effect that the orbital drift has on the final product.

In order to limit the amount of machine learning algorithms used in the processing chain, and to repeatedly use the MCD43C3 product as a reference, which has its limitations, a method to retrieve snow surface albedo using solely AVHRR data would be of great benefit for this product. Recently, a study was published that modified the RTLSR model by including an extra kernel to account for snow surfaces (Jiao *et al.*, 2019). This contribution provides a promising opportunity to estimate the BRDF shape of snow using AVHRR data, if a valid assumption can be found that allows the inversion of the algorithm on a daily basis, similar to the VJB method. Perhaps a dependency of the new kernel on the NDSI, or a pseudo-NDSI retrieved with bands available in AVHRR could provide reliable estimates. This would be very valuable to

this product, so that it can provide independent estimates and, more importantly, retrieve snow and land surface albedo by means of the same model.

The ultimate motivation behind these improvements is to provide a surface albedo dataset that can satisfy, or at least come close, to the accuracy and stability stipulated by the GCOS requirements. This way, there would be confidence that the product can aid the scientific community by improving the quality of climate models and climate change predictions. These predictions are used by governments and agencies all around the world to estimate the possible impacts of our changing climate and its implications on a regional and global scale.

Judging by the current state of affairs, the most valuable way to do this would be to improve our efforts in satellite data harmonization, so that the best of each surface albedo dataset can be used to create a homogenous global surface albedo dataset (Liang, Li and Wang, 2012; He, Liang and Song, 2014). However, this requires state of the art algorithms, along with an open access facility for performing albedo product validation, and a portal for accessing reference albedo datasets (CEOS, 2019). This can only be achieved with a strong international cooperation.

This dataset will be released to the public, once some of the limitations are improved upon, in the hope that future researchers use it to improve its quality, identify unseen issues or use it as a reference or input for their own models and studies.

Appendices

Appendix A

Tables A1-A5 show the spectral adjustment parameters for the different sensors used in this study, using NOAA14 as a reference. The Equations used for each band can be found in Equations 1-4. The band wavelengths can be found in Table 10.

Table A1: Spectral Adjustment parameters for the different sensors used in this study for Band 1.

	B1			
Sensor	**a**	**b**	**c**	**d**
N07	1.00E+00	1.25E-01	1.45E-04	8.53E+00
N09	1.11E-04	8.36E+00	1.00E+00	7.20E-02
N11	1.00E+00	7.62E-02	2.27E-04	7.64E+00
N16	9.95E-01	1.47E-01	9.02E-04	6.99E+00
N18	9.93E-01	1.15E-01	2.10E-03	6.07E+00
N19	2.70E-03	5.84E+00	9.93E-01	1.10E-01
Aqua	4.90E-03	5.42E+00	9.81E-01	5.85E-02
Terra	9.81E-01	5.78E-02	5.00E-03	5.40E+00

Table A2: Analogous to Table A1, but for Band 2.

	B2			
Sensor	**a**	**b**	**c**	**d**
N07	-1.75E-02	1.02E+00	5.68E-03	-5.80E-03
N09	-8.06E-03	1.01E+00	8.80E-03	-9.89E-03
N11	-6.97E-03	1.01E+00	9.49E-03	-1.09E-02
N16	1.68E-02	9.83E-01	6.17E-03	-7.33E-03
N18	1.69E-02	9.82E-01	1.46E-04	-1.22E-04
N19	1.50E-02	9.86E-01	1.64E-02	-1.94E-02
Aqua	5.48E-02	9.39E-01	1.13E-02	-1.28E-02
Terra	5.49E-02	9.39E-01	1.20E-02	-1.35E-02

Table A3: Analogous to Table A1, but for Band 3B (thermal).

	T3B	
Sensor	**a**	**b**
N07	9.88E-01	-1.98E-01
N09	9.86E-01	-2.96E-01
N11	9.89E-01	-3.21E-01
N16	9.83E-01	-5.68E-01
N18	9.99E-01	-2.61E-01
N19	9.95E-01	-3.37E-01
Aqua	1.01E+00	-1.05E+00
Terra	1.01E+00	-1.03E+00

Table A4: Analogous to Table A1, but for Band 4 (thermal).

	T4			
Sensor	**a**	**b**	**c**	**d**
N07	3.61E-05	-4.03E+00	1.00E+00	4.81E-05
N09	1.43E-05	-2.88E+00	1.00E+00	-2.53E-05
N11	3.70E-05	-3.82E+00	1.00E+00	2.21E-05
N16	1.33E-04	-3.74E+00	1.00E+00	3.12E-04
N18	2.41E-05	-2.96E+00	1.00E+00	3.82E-05
N19	3.08E-05	-3.47E+00	1.00E+00	2.83E-05
Aqua	4.29E-04	-3.97E+00	9.99E-01	5.48E-04
Terra	4.26E-04	-4.12E+00	9.99E-01	5.62E-04

Table A5: Analogous to Table A1, but for Band 5 (thermal).

	T5			
Sensor	**a**	**b**	**c**	**d**
N07	2.71E-04	-4.04E+00	1.00E+00	-3.29E-04
N09	4.69E-04	-3.65E+00	9.99E-01	-5.87E-04
N11	4.35E-04	-3.46E+00	9.99E-01	-4.65E-04
N16	1.00E+00	6.06E-05	-1.94E-04	-2.09E+00
N18	1.00E+00	1.32E-04	-1.39E-04	-2.69E+00
N19	1.00E+00	3.35E-04	-4.29E-04	-2.97E+00
Aqua	1.06E-03	-2.52E+00	9.99E-01	-4.07E-04
Terra	1.04E-03	-2.56E+00	9.99E-01	-4.25E-04

Bibliography

Akbari, H., Damon Matthews, H. and Seto, D. (2012) 'The long-term effect of increasing the albedo of urban areas', *Environmental Research Letters*, 7(2), p. 024004. doi: 10.1088/1748-9326/7/2/024004.

Bacour, C. and Bréon, F.-M. (2005) 'Variability of biome reflectance directional signatures as seen by POLDER', *Remote Sensing of Environment*, 98(1), pp. 80–95. doi: 10.1016/j.rse.2005.06.008.

Baret, F. *et al.* (2006a) 'Evaluation of the representativeness of networks of sites for the global validation and intercomparison of land biophysical products: proposition of the CEOS-BELMANIP', *IEEE Transactions on Geoscience and Remote Sensing*, 44(7), pp. 1794–1803. doi: 10.1109/TGRS.2006.876030.

Baret, F. *et al.* (2006b) 'Evaluation of the representativeness of networks of sites for the global validation and intercomparison of land biophysical products: proposition of the CEOS-BELMANIP', *IEEE Transactions on Geoscience and Remote Sensing*, 44(7), pp. 1794–1803. doi: 10.1109/TGRS.2006.876030.

Bates, J. J. *et al.* (2015) 'Sustained Production of Multidecadal Climate Records: Lessons from the NOAA Climate Data Record Program', *Bulletin of the American Meteorological Society*, 97(9), pp. 1573–1581. doi: 10.1175/BAMS-D-15-00015.1.

Belgiu, M. and Drăguţ, L. (2016) 'Random forest in remote sensing: A review of applications and future directions', *ISPRS Journal of Photogrammetry and Remote Sensing*, 114, pp. 24–31. doi: 10.1016/j.isprsjprs.2016.01.011.

Benhadj, I. (2018) *Target Requirements and Gap Analysis Document 2018*, p. 63.

Birdsey, R., Pregitzer, K. and Lucier, A. (2006) 'Forest Carbon Management in the United States', *Journal of Environmental Quality*, 35(4), pp. 1461–1469. doi: 10.2134/jeq2005.0162.

Bojinski, S. *et al.* (2014) 'The Concept of Essential Climate Variables in Support of Climate Research, Applications, and Policy', *Bulletin of the American Meteorological Society*, 95(9), pp. 1431–1443. doi: 10.1175/BAMS-D-13-00047.1.

Bounoua, L. *et al.* (2002) 'Effects of Land Cover Conversion on Surface Climate', *Climatic Change*, 52(1–2), pp. 29–64. doi: 10.1023/A:1013051420309.

Breiman, L. (2001) 'Random Forests', *Machine Learning*, 45(1), pp. 5–32. doi: 10.1023/A:1010933404324.

Bréon, F.-M. and Vermote, E. (2012) 'Correction of MODIS surface reflectance time series for BRDF effects', *Remote Sensing of Environment*, 125, pp. 1–9. doi: 10.1016/j.rse.2012.06.025.

Carroll, J. J. and Fitch, B. W. (1981) 'Effects of solar elevation and cloudiness on snow albedo at the South Pole', *Journal of Geophysical Research: Oceans*, 86(C6), pp. 5271–5276. doi: 10.1029/JC086iC06p05271.

CEOS (2019) 'Global Surface Albedo Product Validation Best Practices Protocol'. doi: 10.5067/doc/ceoswgcv/lpv/albedo.001.

Chander, G. *et al.* (2013) 'Applications of Spectral Band Adjustment Factors (SBAF) for Cross-Calibration', *IEEE Transactions on Geoscience and Remote Sensing*, 51(3), pp. 1267–1281. doi: 10.1109/TGRS.2012.2228007.

Chapin, F. S. *et al.* (2005a) 'Role of Land-Surface Changes in Arctic Summer Warming', *Science*, 310(5748), pp. 657–660. doi: 10.1126/science.1117368.

Chapin, F. S. *et al.* (2005b) 'Role of Land-Surface Changes in Arctic Summer Warming', *Science*, 310(5748), pp. 657–660. doi: 10.1126/science.1117368.

Chen, J. M. (1999) 'Spatial Scaling of a Remotely Sensed Surface Parameter by Contexture', *Remote Sensing of Environment*, 69(1), pp. 30–42. doi: 10.1016/S0034-4257(99)00006-1.

Chen, X. *et al.* (2015) 'Observed contrast changes in snow cover phenology in northern middle and high latitudes from 2001–2014', *Scientific Reports*, 5(1), p. 16820. doi: 10.1038/srep16820.

Chrysoulakis, N., Mitraka, Z. and Gorelick, N. (2018) 'Exploiting satellite observations for global surface albedo trends monitoring', *Theoretical and Applied Climatology*. doi: 10.1007/s00704-018-2663-6.

Claverie, M. *et al.* (2016) 'A 30+ Year AVHRR LAI and FAPAR Climate Data Record: Algorithm Description and Validation', *Remote Sensing*, 8(3), p. 263. doi: 10.3390/rs8030263.

Claverie, M. *et al.* (2018) 'The Harmonized Landsat and Sentinel-2 data set', *Remote Sensing of Environment (in review)*.

Claverie, M., Masek, J. and Ju, J. (2016) 'Harmonized Landsat-8 Sentinel-2 (HLS) Product User's Guide.' Available at: https://hls.gsfc.nasa.gov/wp-content/uploads/2017/08/HLS.v1.3.UserGuide_v2.pdf (Accessed: 9 February 2018).

Clerbaux, N. *et al.* (2020) 'The Climate Monitoring SAF Outgoing Longwave Radiation from AVHRR', *Remote Sensing*, 12(6), p. 929. doi: 10.3390/rs12060929.

Comiso, J. C. (2003) 'Warming Trends in the Arctic from Clear Sky Satellite Observations', *Journal of Climate*, 16(21), pp. 3498–3510. doi: 10.1175/1520-0442(2003)016<3498:WTITAF>2.0.CO;2.

Dardel, C. *et al.* (2014) 'Re-greening Sahel: 30years of remote sensing data and field observations (Mali, Niger)', *Remote Sensing of Environment*, 140, pp. 350–364. doi: 10.1016/j.rse.2013.09.011.

Davin, E. L. and de Noblet-Ducoudré, N. (2010) 'Climatic Impact of Global-Scale Deforestation: Radiative versus Nonradiative Processes', *Journal of Climate*, 23(1), pp. 97–112. doi: 10.1175/2009JCLI3102.1.

Deering, D. and Eck, T. (1987) 'Atmospheric optical depth effects on angular anisotropy of plant canopy reflectance', *International Journal of Remote Sensing*, 8(6), pp. 893–916. doi: 10.1080/01431168708948697.

Déry, S. J. and Brown, R. D. (2007a) 'Recent Northern Hemisphere snow cover extent trends and implications for the snow-albedo feedback', *Geophysical Research Letters*, 34(22), p. L22504. doi: 10.1029/2007GL031474.

Déry, S. J. and Brown, R. D. (2007b) 'Recent Northern Hemisphere snow cover extent trends and implications for the snow-albedo feedback', *Geophysical Research Letters*, 34(22), p. L22504. doi: 10.1029/2007GL031474.

Dickinson, R. E. (1983) 'Land Surface Processes and Climate—Surface Albedos and Energy Balance', *Advances in Geophysics*, 25, pp. 305–353. doi: 10.1016/S0065-2687(08)60176-4.

Dinguirard, M. and Slater, P. N. (1999) 'Calibration of Space-Multispectral Imaging Sensors: A Review', *Remote Sensing of Environment*, 68(3), pp. 194–205. doi: 10.1016/S0034-4257(98)00111-4.

D'Odorico, P. *et al.* (2013) 'Experimental Evaluation of Sentinel-2 Spectral Response Functions for NDVI Time-Series Continuity', *IEEE Transactions on Geoscience and Remote Sensing*, 51(3), pp. 1336–1348. doi: 10.1109/TGRS.2012.2235447.

Dole, R. *et al.* (2011) 'Was there a basis for anticipating the 2010 Russian heat wave?', *Geophysical Research Letters*, 38(6). doi: 10.1029/2010GL046582.

Dorigo, W. *et al.* (2012) 'Evaluating global trends (1988–2010) in harmonized multi-satellite surface soil moisture', *Geophysical Research Letters*, 39(18). doi: 10.1029/2012GL052988.

Drusch, M. *et al.* (2012) 'Sentinel-2: ESA's Optical High-Resolution Mission for GMES Operational Services', *Remote Sensing of Environment*, 120, pp. 25–36. doi: 10.1016/j.rse.2011.11.026.

Dybbroe, A., Karlsson, K.-G. and Thoss, A. (2005a) 'NWCSAF AVHRR Cloud Detection and Analysis Using Dynamic Thresholds and Radiative Transfer Modeling. Part I: Algorithm Description', *Journal of Applied Meteorology*, 44(1), pp. 39–54. doi: 10.1175/JAM-2188.1.

Dybbroe, A., Karlsson, K.-G. and Thoss, A. (2005b) 'NWCSAF AVHRR Cloud Detection and Analysis Using Dynamic Thresholds and Radiative Transfer Modeling. Part I: Algorithm Description', *Journal of Applied Meteorology*, 44(1), pp. 39–54. doi: 10.1175/JAM-2188.1.

Dybbroe, A., Karlsson, K.-G. and Thoss, A. (2005c) 'NWCSAF AVHRR Cloud Detection and Analysis Using Dynamic Thresholds and Radiative Transfer Modeling. Part II: Tuning and Validation', *Journal of Applied Meteorology*, 44(1), pp. 55–71. doi: 10.1175/JAM-2189.1.

Essential Climate Variables (2017) *World Meteorological Organization*. Available at: https://public.wmo.int/en/programmes/global-climate-observing-system/essential-climate-variables (Accessed: 2 July 2020).

Fan, X. and Liu, Y. (2016) 'A global study of NDVI difference among moderate-resolution satellite sensors', *ISPRS Journal of Photogrammetry and Remote Sensing*, 121, pp. 177–191. doi: 10.1016/j.isprsjprs.2016.09.008.

Fan, Xingwang and Liu, Y. (2017) 'A comparison of NDVI intercalibration methods', *International Journal of Remote Sensing*, 38(19), pp. 5273–5290. doi: 10.1080/01431161.2017.1338784.

Fan, X. and Liu, Y. (2017) 'A Generalized Model for Intersensor NDVI Calibration and Its Comparison With Regression Approaches', *IEEE Transactions on Geoscience and Remote Sensing*, 55(3), pp. 1842–1852. doi: 10.1109/TGRS.2016.2635802.

Faria, T. de O. *et al.* (2018) 'Surface albedo in different land-use and cover types in Amazon forest region', *Revista Ambiente & Água*, 13(2). doi: 10.4136/ambi-agua.2120.

Flasse, S. P. and Ceccato, P. (1996) 'A contextual algorithm for AVHRR fire detection', *International Journal of Remote Sensing*, 17(2), pp. 419–424. doi: 10.1080/01431169608949018.

Fletcher, C. G., Thackeray, C. W. and Burgers, T. M. (2015) 'Evaluating biases in simulated snow albedo feedback in two generations of climate models', *Journal of Geophysical Research: Atmospheres*, 120(1), p. 2014JD022546. doi: 10.1002/2014JD022546.

Franch, B. *et al.* (2013) 'Analysis of directional effects on atmospheric correction', *Remote Sensing of Environment*, 128(Supplement C), pp. 276–288. doi: 10.1016/j.rse.2012.10.018.

Franch, B. *et al.* (2014) 'Retrieval of Surface Albedo on a Daily Basis: Application to MODIS Data', *IEEE Transactions on Geoscience and Remote Sensing*, 52(12), pp. 7549–7558. doi: 10.1109/TGRS.2014.2313842.

Franch, B. *et al.* (2016a) 'A 30+ year AVHRR Land Surface Reflectance Climate 2 Data Record and its application to wheat yield 3 monitoring'.

Franch, B. *et al.* (2016b) 'A 30+ year AVHRR Land Surface Reflectance Climate 2 Data Record and its application to wheat yield 3 monitoring'.

Franch, B. *et al.* (2018) 'Toward Landsat and Sentinel-2 BRDF Normalization and Albedo Estimation: A Case Study in the Peruvian Amazon Forest', *Frontiers in Earth Science*, 6. doi: 10.3389/feart.2018.00185.

Franke, J., Heinzel, V. and Menz, G. (2006) 'Assessment of NDVI- Differences Caused by Sensor Specific Relative Spectral Response Functions', in *2006 IEEE International Symposium on Geoscience and Remote Sensing*. *2006 IEEE International Symposium on Geoscience and Remote Sensing*, pp. 1138–1141. doi: 10.1109/IGARSS.2006.294.

Frantz, D. *et al.* (2018) 'Improvement of the Fmask algorithm for Sentinel-2 images: Separating clouds from bright surfaces based on parallax effects', *Remote Sensing of Environment*, 215, pp. 471–481. doi: 10.1016/j.rse.2018.04.046.

Gardner, A. S. and Sharp, M. J. (2010) 'A review of snow and ice albedo and the development of a new physically based broadband albedo parameterization', *Journal of Geophysical Research: Earth Surface*, 115(F1), p. F01009. doi: 10.1029/2009JF001444.

Gash, J. H. C. and Shuttleworth, W. J. (1991) 'Tropical deforestation: Albedo and the surface-energy balance', *Climatic Change*, 19(1), pp. 123–133. doi: 10.1007/BF00142219.

GCOS-200 (2016) *The Global Observing System For Climate Implementation Needs*. Available at: https://library.wmo.int/doc_num.php?explnum_id=3417 (Accessed: 22 July 2020).

Gomez-Chova, L. *et al.* (2007) 'Cloud-Screening Algorithm for ENVISAT/MERIS Multispectral Images', *IEEE Transactions on Geoscience and Remote Sensing*, 45(12), pp. 4105–4118. doi: 10.1109/TGRS.2007.905312.

Goswami, S. *et al.* (2015) *Relationships of NDVI, Biomass, and Leaf Area Index (LAI) for six key plant species in Barrow, Alaska*. e1127. PeerJ Inc. doi: 10.7287/peerj.preprints.913v1.

Govaerts, Y. M. *et al.* (2008) 'Generating global surface albedo products from multiple geostationary satellites', *Remote Sensing of Environment*, 112(6), pp. 2804–2816. doi: 10.1016/j.rse.2008.01.012.

Groisman, P. Y., Karl, T. R. and Knight, R. W. (1994) 'Observed Impact of Snow Cover on the Heat Balance and the Rise of Continental Spring Temperatures', *Science*, 263(5144), pp. 198–200. doi: 10.1126/science.263.5144.198.

Gutman, G. G. (1991) 'Vegetation indices from AVHRR: An update and future prospects', *Remote Sensing of Environment*, 35(2), pp. 121–136. doi: 10.1016/0034-4257(91)90005-Q.

Haboudane, D. *et al.* (2004) 'Hyperspectral vegetation indices and novel algorithms for predicting green LAI of crop canopies: Modeling and validation in the context of precision agriculture', *Remote Sensing of Environment*, 90(3), pp. 337–352. doi: 10.1016/j.rse.2003.12.013.

Hall, D. K. *et al.* (2002) 'MODIS snow-cover products', *Remote Sensing of Environment*, 83(1), pp. 181–194. doi: 10.1016/S0034-4257(02)00095-0.

Hapke, B. and Hoen, H. van (1963) 'Photometric studies of complex surfaces, with applications to the Moon', *Journal of Geophysical Research (1896-1977)*, 68(15), pp. 4545–4570. doi: 10.1029/JZ068i015p04545.

He, K. *et al.* (2016) 'Sensor Stability for SST (3S): Toward Improved Long-Term Characterization of AVHRR Thermal Bands', *Remote Sensing*, 8(4), p. 346. doi: 10.3390/rs8040346.

He, T. *et al.* (2013) 'Greenland surface albedo changes in July 1981–2012 from satellite observations', *Environmental Research Letters*, 8(4), p. 044043. doi: 10.1088/1748-9326/8/4/044043.

He, T., Liang, S. and Song, D.-X. (2014) 'Analysis of global land surface albedo climatology and spatial-temporal variation during 1981–2010 from multiple satellite products', *Journal of Geophysical Research: Atmospheres*, 119(17), p. 2014JD021667. doi: 10.1002/2014JD021667.

Heidinger, A. K., Frey, R. and Pavolonis, M. (2004) 'Relative merits of the 1.6 and 3.75 □m channels of the AVHRR/3 for cloud detection', *Canadian Journal of Remote Sensing*, 30(2), p. 13.

Hollmann, R. *et al.* (2013) 'The ESA Climate Change Initiative: Satellite Data Records for Essential Climate Variables', *Bulletin of the American Meteorological Society*, 94(10), pp. 1541–1552. doi: 10.1175/BAMS-D-11-00254.1.

Hu, B. *et al.* (2000) 'Surface Albedos and Angle-Corrected NDVI from AVHRR Observations of South America', *Remote Sensing of Environment*, 71(2), pp. 119–132. doi: 10.1016/S0034-4257(99)00050-4.

Ji, L. and Brown, J. F. (2017) 'Effect of NOAA satellite orbital drift on AVHRR-derived phenological metrics', *International Journal of Applied Earth Observation and Geoinformation*, 62, pp. 215–223. doi: 10.1016/j.jag.2017.06.013.

Jiao, Z. *et al.* (2019) 'Development of a snow kernel to better model the anisotropic reflectance of pure snow in a kernel-driven BRDF model framework', *Remote Sensing of Environment*, 221, pp. 198–209. doi: 10.1016/j.rse.2018.11.001.

Julien, Y. and Sobrino, J. A. (2011) 'Monitoring global vegetation with the Yearly Land Cover Dynamics (YLCD) method', in *Analysis of Multi-temporal Remote Sensing Images (Multi-Temp), 2011 6th International Workshop on the*. IEEE, pp. 121–124. Available at: http://ieeexplore.ieee.org/abstract/document/6005063/ (Accessed: 28 June 2017).

Justice, C. O. *et al.* (2002) 'An overview of MODIS Land data processing and product status', *Remote Sensing of Environment*, 83(1), pp. 3–15. doi: 10.1016/S0034-4257(02)00084-6.

Karlsson, K.-G. *et al.* (2013) 'CLARA-A1: a cloud, albedo, and radiation dataset from 28 yr of global AVHRR data', *Atmospheric Chemistry and Physics*, 13(10), pp. 5351–5367. doi: https://doi.org/10.5194/acp-13-5351-2013.

Karlsson, K.-G. and Dybbroe, A. (2010) 'Evaluation of Arctic cloud products from the EUMETSAT Climate Monitoring Satellite Application Facility based on CALIPSO-CALIOP observations', *Atmospheric Chemistry And Physics*, 10(4), pp. 1789–1807.

Kaufman, Y. J. *et al.* (2005) 'A critical examination of the residual cloud contamination and diurnal sampling effects on MODIS estimates of aerosol over ocean', *IEEE Transactions on Geoscience and Remote Sensing*, 43(12), pp. 2886–2897. doi: 10.1109/TGRS.2005.858430.

Kendall, M. and Gibbons, J. D. (1990) *Rank Correlation Methods*. 5 edition. London : New York, NY: Oxford University Press.

Key, J. R. *et al.* (2001) 'Estimating the cloudy-sky albedo of sea ice and snow from space', *Journal of Geophysical Research: Atmospheres*, 106(D12), pp. 12489–12497. doi: 10.1029/2001JD900069.

Khlopenkov, K. V. and Trishchenko, A. P. (2007) 'SPARC: New Cloud, Snow, and Cloud Shadow Detection Scheme for Historical 1-km AVHHR Data over Canada', *Journal of Atmospheric and Oceanic Technology*, 24(3), pp. 322–343. doi: 10.1175/JTECH1987.1.

Kim, Y. *et al.* (2010) 'Spectral compatibility of vegetation indices across sensors: band decomposition analysis with Hyperion data', *Journal of Applied Remote Sensing*, 4(1), p. 043520. doi: 10.1117/1.3400635.

Kokaly, R. F. *et al.* (2003) 'Mapping vegetation in Yellowstone National Park using spectral feature analysis of AVIRIS data', *Remote Sensing of Environment*, 84(3), pp. 437–456. doi: 10.1016/S0034-4257(02)00133-5.

Kokaly, R. F. *et al.* (2017) *USGS Spectral Library Version 7*. USGS Numbered Series 1035. Reston, VA: U.S. Geological Survey, p. 68. Available at: http://pubs.er.usgs.gov/publication/ds1035 (Accessed: 20 February 2018).

Lebourgeois, F. *et al.* (2010) 'Simulating phenological shifts in French temperate forests under two climatic change scenarios and four driving global circulation models', *International Journal of Biometeorology*, 54(5), pp. 563–581. doi: 10.1007/s00484-010-0305-5.

van Leeuwen, W. J. D. *et al.* (2006) 'Multi-sensor NDVI data continuity: Uncertainties and implications for vegetation monitoring applications', *Remote Sensing of Environment*, 100(1), pp. 67–81. doi: 10.1016/j.rse.2005.10.002.

Lejeune, Q. *et al.* (2015) 'Influence of Amazonian deforestation on the future evolution of regional surface fluxes, circulation, surface temperature and precipitation', *Climate Dynamics*, 44(9), pp. 2769–2786. doi: 10.1007/s00382-014-2203-8.

Li, J. and Roy, D. P. (2017) 'A Global Analysis of Sentinel-2A, Sentinel-2B and Landsat-8 Data Revisit Intervals and Implications for Terrestrial Monitoring', *Remote Sensing*, 9(9), p. 902. doi: 10.3390/rs9090902.

Lian, M. S. and Cess, R. D. (1977) 'Energy Balance Climate Models: A Reappraisal of Ice-Albedo Feedback', *Journal of the Atmospheric Sciences*, 34(7), pp. 1058–1062. doi: 10.1175/1520-0469(1977)034<1058:EBCMAR>2.0.CO;2.

Liang, S. (2001) 'Narrowband to broadband conversions of land surface albedo I: Algorithms', *Remote Sensing of Environment*, 76(2), pp. 213–238. doi: 10.1016/S0034-4257(00)00205-4.

Liang, S. *et al.* (2002) 'Validating MODIS land surface reflectance and albedo products: methods and preliminary results', *Remote Sensing of Environment*, 83(1), pp. 149–162. doi: 10.1016/S0034-4257(02)00092-5.

Liang, S., Li, X. and Wang, J. (2012) *Advanced Remote Sensing: Terrestrial Information Extraction and Applications*. Academic Press.

Liang, S., Stroeve, J. and Box, J. E. (2005) 'Mapping daily snow/ice shortwave broadband albedo from Moderate Resolution Imaging Spectroradiometer (MODIS): The improved direct retrieval algorithm and validation with Greenland in situ measurement', *Journal of Geophysical Research: Atmospheres*, 110(D10), p. D10109. doi: 10.1029/2004JD005493.

Liu, J. *et al.* (2009) 'Validation of Moderate Resolution Imaging Spectroradiometer (MODIS) albedo retrieval algorithm: Dependence of albedo on solar zenith angle', *Journal of Geophysical Research: Atmospheres*, 114(D1), p. D01106. doi: 10.1029/2008JD009969.

Liu, Q. *et al.* (2013) 'Preliminary evaluation of the long-term GLASS albedo product', *International Journal of Digital Earth*, 6(sup1), pp. 69–95. doi: 10.1080/17538947.2013.804601.

Loranty, M. M. *et al.* (2014a) 'Vegetation controls on northern high latitude snow-albedo feedback: observations and CMIP5 model simulations', *Global Change Biology*, 20(2), pp. 594–606. doi: 10.1111/gcb.12391.

Loranty, M. M. *et al.* (2014b) 'Vegetation controls on northern high latitude snow-albedo feedback: observations and CMIP5 model simulations', *Global Change Biology*, 20(2), pp. 594–606. doi: 10.1111/gcb.12391.

Lucht, W., Schaaf, C. B. and Strahler, A. H. (2000) 'An algorithm for the retrieval of albedo from space using semiempirical BRDF models', *IEEE Transactions on Geoscience and Remote Sensing*, 38(2), pp. 977–998. doi: 10.1109/36.841980.

Lyapustin, A. *et al.* (2009) 'Retrieval of snow grain size over Greenland from MODIS', *Remote Sensing of Environment*, 113(9), pp. 1976–1987. doi: 10.1016/j.rse.2009.05.008.

Maignan, F., Bréon, F.-M. and Lacaze, R. (2004) 'Bidirectional reflectance of Earth targets: evaluation of analytical models using a large set of spaceborne measurements with emphasis on the Hot Spot', *Remote Sensing of Environment*, 90(2), pp. 210–220. doi: 10.1016/j.rse.2003.12.006.

Manabe, S. and Wetherald, R. T. (1975) 'The Effects of Doubling the CO2 Concentration on the climate of a General Circulation Model', *Journal of the Atmospheric Sciences*, 32(1), pp. 3–15. doi: 10.1175/1520-0469(1975)032<0003:TEODTC>2.0.CO;2.

Mann, H. B. (1945) 'Nonparametric Tests Against Trend', *Econometrica*, 13(3), pp. 245–259. doi: 10.2307/1907187.

Mantgem, P. J. van *et al.* (2009) 'Widespread Increase of Tree Mortality Rates in the Western United States', *Science*, 323(5913), pp. 521–524. doi: 10.1126/science.1165000.

Marticorena *et al.* (2004) 'Mapping the aerodynamic roughness length of desert surfaces from the POLDER/ADEOS bi-directional reflectance product', *International Journal of Remote Sensing*, 25(3), pp. 603–626. doi: 10.1080/0143116031000116976.

Marticorena, B. *et al.* (2006) 'Surface and aerodynamic roughness in arid and semiarid areas and their relation to radar backscatter coefficient', *Journal of Geophysical Research: Earth Surface*, 111(F3), p. F03017. doi: 10.1029/2006JF000462.

Martínez-Beltrán, C. *et al.* (2009) 'Multisensor comparison of NDVI for a semi-arid environment in Spain', *International Journal of Remote Sensing*, 30(5), pp. 1355–1384. doi: 10.1080/01431160802509025.

Masson-Delmotte, V. *et al.* (2019) *Global warming of 1.5°C. An IPCC Special Report on the impacts of global warming of 1.5°C above pre-industrial levels and related global greenhouse gas emission pathways, in the context of strengthening the global response to the threat of climate change, sustainable development, and efforts to eradicate poverty*. IPCC.

Mateo-García, G. *et al.* (2018) 'Multitemporal Cloud Masking in the Google Earth Engine', *Remote Sensing*, 10(7), p. 1079. doi: 10.3390/rs10071079.

McClain, E. P., Pichel, W. G. and Walton, C. C. (1985) 'Comparative performance of AVHRR-based multichannel sea surface temperatures', *Journal of Geophysical Research: Oceans*, 90(C6), pp. 11587–11601. doi: 10.1029/JC090iC06p11587.

McManus, kelly M. *et al.* (2012) 'Satellite-based evidence for shrub and graminoid tundra expansion in northern Quebec from 1986 to 2010', *Global Change Biology*, 18(7), pp. 2313–2323. doi: 10.1111/j.1365-2486.2012.02708.x.

Miura, T., Huete, A. and Yoshioka, H. (2006) 'An empirical investigation of cross-sensor relationships of NDVI and red/near-infrared reflectance using EO-1 Hyperion data', *Remote Sensing of Environment*, 100(2), pp. 223–236. doi: 10.1016/j.rse.2005.10.010.

Moreno Ruiz, J. A. *et al.* (2012) 'Burned area mapping time series in Canada (1984–1999) from NOAA-AVHRR LTDR: A comparison with other remote sensing products and fire perimeters', *Remote Sensing of Environment*, 117, pp. 407–414. doi: 10.1016/j.rse.2011.10.017.

Musial, J. P. *et al.* (2014) 'Probabilistic approach to cloud and snow detection on Advanced Very High Resolution Radiometer (AVHRR) imagery', *Atmospheric Measurement Techniques (AMT)*, 7(3), pp. 799–822. doi: info:doi:10.5194/amt-7-799-2014.

Myhre, G. *et al.* (2013) 'Anthropogenic and Natural Radiative Forcing', p. 82.

Nagol, J. R., Vermote, E. F. and Prince, S. D. (2014) 'Quantification of Impact of Orbital Drift on Inter-Annual Trends in AVHRR NDVI Data', *Remote Sensing*, 6(7), pp. 6680–6687. doi: 10.3390/rs6076680.

Ohring, G. and Wielicki, B. A. (2005) *Satellite Instrument Calibration for Measuring Global Climate Change. Report of a Workshop*. Available at: https://journals.ametsoc.org/doi/pdf/10.1175/BAMS-86-9-1303 (Accessed: 22 May 2020).

Pearson, R. G. *et al.* (2013a) 'Shifts in Arctic vegetation and associated feedbacks under climate change', *Nature Climate Change*, 3(7), pp. 673–677. doi: 10.1038/nclimate1858.

Pearson, R. G. *et al.* (2013b) 'Shifts in Arctic vegetation and associated feedbacks under climate change', *Nature Climate Change*, 3(7), pp. 673–677. doi: 10.1038/nclimate1858.

Pepin, N. *et al.* (2015) 'Elevation-dependent warming in mountain regions of the world', *Nature Climate Change*, 5(5), pp. 424–430. doi: 10.1038/nclimate2563.

Planque, C., Carrer, D. and Roujean, J.-L. (2017) 'Analysis of MODIS albedo changes over steady woody covers in France during the period of 2001–2013', *Remote Sensing of Environment*, 191, pp. 13–29. doi: 10.1016/j.rse.2016.12.019.

Qu, X. and Hall, A. (2007a) 'What Controls the Strength of Snow-Albedo Feedback?', *Journal of Climate*, 20(15), pp. 3971–3981. doi: 10.1175/JCLI4186.1.

Qu, X. and Hall, A. (2007b) 'What Controls the Strength of Snow-Albedo Feedback?', *Journal of Climate*, 20(15), pp. 3971–3981. doi: 10.1175/JCLI4186.1.

Qu, X. and Hall, A. (2014) 'On the persistent spread in snow-albedo feedback', *Climate Dynamics; Heidelberg*, 42(1–2), pp. 69–81. doi: http://dx.doi.org/10.1007/s00382-013-1774-0.

Qu, Y. *et al.* (2015) 'Mapping Surface Broadband Albedo from Satellite Observations: A Review of Literatures on Algorithms and Products', *Remote Sensing*, 7(1), pp. 990–1020. doi: 10.3390/rs70100990.

Querin, C. A. S. *et al.* (2016) 'Spatiotemporal NDVI, LAI, albedo, and surface temperature dynamics in the southwest of the Brazilian Amazon forest', *Journal of Applied Remote Sensing*, 10(2), p. 026007. doi: 10.1117/1.JRS.10.026007.

Randerson, J. T. *et al.* (2006) 'The Impact of Boreal Forest Fire on Climate Warming', *Science*, 314(5802), pp. 1130–1132. doi: 10.1126/science.1132075.

Roesch, A. (2006) *Evaluation of surface albedo and snow cover in AR4 coupled climate models - Roesch - 2006 - Journal of Geophysical Research: Atmospheres - Wiley Online Library*. Available at: https://agupubs.onlinelibrary.wiley.com/doi/epdf/10.1029/2005JD006473 (Accessed: 18 April 2019).

Roger, J. C. and Vermote, E. F. (1998) 'A Method to Retrieve the Reflectivity Signature at 3.75 μm from AVHRR Data', *Remote Sensing of Environment*, 64(1), pp. 103–114. doi: 10.1016/S0034-4257(97)00173-9.

Roujean, J.-L., Leroy, M. and Deschamps, P.-Y. (1992) 'A bidirectional reflectance model of the Earth's surface for the correction of remote sensing data', *Journal of Geophysical Research: Atmospheres*, 97(D18), pp. 20455–20468. doi: 10.1029/92JD01411.

Roy, D. P. *et al.* (2017) 'Examination of Sentinel-2A multi-spectral instrument (MSI) reflectance anisotropy and the suitability of a general method to normalize MSI reflectance to nadir BRDF adjusted reflectance', *Remote Sensing of Environment*, 199, pp. 25–38. doi: 10.1016/j.rse.2017.06.019.

Sánchez-Zapero, J. (2019) *Product Quality Assessment Report. CDR AVHRR-based Surface Albedo v1.0*. ECMWF Copernicus. Available at: https://datastore.copernicus-climate.eu/documents/satellite-albedo/D2.3.1-v1.0_PQAR_CDR_SA_AVHRR_v1.0_PRODUCTS_v1.0.1.pdf (Accessed: 24 October 2020).

Saunders, R. W. (1990) 'The determination of broad band surface albedo from AVHRR visible and near-infrared radiances', *International Journal of Remote Sensing*, 11(1), pp. 49–67. doi: 10.1080/01431169008955000.

Schaaf, C. B. *et al.* (2002a) 'First operational BRDF, albedo nadir reflectance products from MODIS', *Remote Sensing of Environment*, 83(1–2), pp. 135–148. doi: 10.1016/S0034-4257(02)00091-3.

Schaaf, C. B. *et al.* (2002b) 'First operational BRDF, albedo nadir reflectance products from MODIS', *Remote Sensing of Environment*, 83(1–2), pp. 135–148. doi: 10.1016/S0034-4257(02)00091-3.

Schill, S. R. *et al.* (2004) 'Temporal Modeling of Bidirectional Reflection Distribution Function (BRDF) in Coastal Vegetation', *GIScience & Remote Sensing*, 41(2), pp. 116–135. doi: 10.2747/1548-1603.41.2.116.

Schulz, J. *et al.* (2008) 'Operational climate monitoring from space: The EUMETSAT satellite application facility on climate monitoring (CM-SAF)', *Atmospheric Chemistry and Physics Discussions*, 8(3), pp. 8517–8563.

Sen, P. K. (1968) 'Estimates of the Regression Coefficient Based on Kendall's Tau', *Journal of the American Statistical Association*, 63(324), pp. 1379–1389. doi: 10.1080/01621459.1968.10480934.

Skakun, S. *et al.* (2017) 'Multispectral Misregistration of Sentinel-2A Images: Analysis and Implications for Potential Applications', *IEEE Geoscience and Remote Sensing Letters*, 14(12), pp. 2408–2412. doi: 10.1109/LGRS.2017.2766448.

Skakun, S. *et al.* (2018) 'Transitioning from MODIS to VIIRS: an analysis of inter-consistency of NDVI data sets for agricultural monitoring', *International Journal of Remote Sensing*, 39(4), pp. 971–992. doi: 10.1080/01431161.2017.1395970.

Sobrino, J. A. and Julien, Y. (2016) 'Exploring the Validity of the Long-Term Data Record V4 Database for Land Surface Monitoring', *IEEE Journal of Selected Topics in Applied Earth Observations and Remote Sensing*, 9(8), pp. 3607–3614. doi: 10.1109/JSTARS.2016.2567642.

Song, X.-P. *et al.* (2018) 'Global land change 1982-2016', *Nature*, 560(7720), pp. 639–643. doi: 10.1038/s41586-018-0411-9.

Stengel, M. *et al.* (2017) 'Cloud property datasets retrieved from AVHRR, MODIS, AATSR and MERIS in the framework of the Cloud_cci project', *Earth System Science Data*, 9(2), pp. 881–904. doi: https://doi.org/10.5194/essd-9-881-2017.

Stengel, M. *et al.* (2020) 'Cloud_cci Advanced Very High Resolution Radiometer post meridiem (AVHRR-PM) dataset version 3: 35-year climatology of global cloud and radiation properties', *Earth System Science Data*, 12(1), pp. 41–60. doi: https://doi.org/10.5194/essd-12-41-2020.

Steven, M. D. *et al.* (2003) 'Intercalibration of vegetation indices from different sensor systems', *Remote Sensing of Environment*, 88(4), pp. 412–422. doi: 10.1016/j.rse.2003.08.010.

Stieglitz, M. *et al.* (2003) 'The role of snow cover in the warming of arctic permafrost', *Geophysical Research Letters*, 30(13). doi: 10.1029/2003GL017337.

Stowe, L. L., Davis, P. and McClain, E. P. (1995) 'Evaluating the CLAVR (clouds from AVHRR) phase I-cloud cover experimental product', *Advances in Space Research*, 16(10), pp. 21–24. doi: 10.1016/0273-1177(95)00374-N.

Strahler, A. *et al.* (1999) 'MODIS Land Cover and Land-Cover Change', p. 72.

Strobl, C., Malley, J. and Tutz, G. (2009) 'An introduction to recursive partitioning: Rationale, application, and characteristics of classification and regression trees, bagging, and random forests', *Psychological Methods*, 14(4), pp. 323–348. doi: 10.1037/a0016973.

Stroeve, J. *et al.* (2005) 'Accuracy assessment of the MODIS 16-day albedo product for snow: comparisons with Greenland in situ measurements', *Remote Sensing of Environment*, 94(1), pp. 46–60. doi: 10.1016/j.rse.2004.09.001.

Strugnell, N. C., Lucht, W. and Schaaf, C. (2001) 'A global albedo data set derived from AVHRR data for use in climate simulations', *Geophysical Research Letters*, 28(1), pp. 191–194. doi: 10.1029/2000GL011580.

Taravat, A. *et al.* (2015) 'Neural Networks and Support Vector Machine Algorithms for Automatic Cloud Classification of Whole-Sky Ground-Based Images', *IEEE Geoscience and Remote Sensing Letters*, 12(3), pp. 666–670. doi: 10.1109/LGRS.2014.2356616.

Teillet, P. M. *et al.* (2001) 'Radiometric cross-calibration of the Landsat-7 ETM+ and Landsat-5 TM sensors based on tandem data sets', *Remote Sensing of Environment*, 78(1–2), pp. 39–54. doi: 10.1016/S0034-4257(01)00248-6.

Teillet, P. M. *et al.* (2007) 'Impacts of spectral band difference effects on radiometric cross-calibration between satellite sensors in the solar-reflective spectral domain', *Remote Sensing of Environment*, 110(3), pp. 393–409. doi: 10.1016/j.rse.2007.03.003.

Thackeray, C. W. and Fletcher, C. G. (2016) 'Snow albedo feedback: Current knowledge, importance, outstanding issues and future directions', *Progress in Physical Geography*, 40(3), pp. 392–408. doi: 10.1177/0309133315620999.

Thenkabail*, P. S. (2004) 'Inter-sensor relationships between IKONOS and Landsat-7 ETM+ NDVI data in three ecoregions of Africa', *International Journal of Remote Sensing*, 25(2), pp. 389–408. doi: 10.1080/0143116031000114842.

Toutenburg, H. (1975) 'Hollander, M., D. A. Wolfe: Nonparametric statistical methods. John Wiley & Sons, New York-Sydney-Tokyo-Mexico City 1973. 503 S., $9.50', *Biometrische Zeitschrift*, 17(8), pp. 526–526. doi: 10.1002/bimj.19750170808.

Trenberth, K. E. *et al.* (2006) 'Monitoring and Prediction of the Earth's Climate: A Future Perspective', *Journal of Climate*, 19(20), pp. 5001–5008. doi: 10.1175/JCLI3897.1.

Trishchenko, A. P. (2002) 'Removing Unwanted Fluctuations in the AVHRR Thermal Calibration Data Using Robust Techniques', *Journal of Atmospheric and Oceanic Technology*, 19(12), pp. 1939–1954. doi: 10.1175/1520-0426(2002)019<1939:RUFITA>2.0.CO;2.

Trishchenko, A. P. *et al.* (2002) 'Trends and uncertainties in thermal calibration of AVHRR radiometers onboard NOAA-9 to NOAA-16', *Journal of Geophysical Research: Atmospheres*, 107(D24), p. ACL 17-1-ACL 17-13. doi: 10.1029/2002JD002353.

Trishchenko, A. P. *et al.* (2008a) 'A Method to Derive the Multispectral Surface Albedo Consistent with MODIS from Historical AVHRR and VGT Satellite Data', *Journal of Applied Meteorology and Climatology*, 47(4), pp. 1199–1221. doi: 10.1175/2007JAMC1724.1.

Trishchenko, A. P. *et al.* (2008b) 'A Method to Derive the Multispectral Surface Albedo Consistent with MODIS from Historical AVHRR and VGT Satellite Data',

Journal of Applied Meteorology and Climatology, 47(4), pp. 1199–1221. doi: 10.1175/2007JAMC1724.1.

Trishchenko, A. P., Cihlar, J. and Li, Z. (2002a) 'Effects of spectral response function on surface reflectance and NDVI measured with moderate resolution satellite sensors', *Remote Sensing of Environment*, 81(1), pp. 1–18. doi: 10.1016/S0034-4257(01)00328-5.

Trishchenko, A. P., Cihlar, J. and Li, Z. (2002b) 'Effects of spectral response function on surface reflectance and NDVI measured with moderate resolution satellite sensors', *Remote Sensing of Environment*, 81(1), pp. 1–18. doi: 10.1016/S0034-4257(01)00328-5.

Tzotsos, A. and Argialas, D. (2008) 'Support Vector Machine Classification for Object-Based Image Analysis', in Blaschke, T., Lang, S., and Hay, G. J. (eds) *Object-Based Image Analysis: Spatial Concepts for Knowledge-Driven Remote Sensing Applications*. Berlin, Heidelberg: Springer (Lecture Notes in Geoinformation and Cartography), pp. 663–677. doi: 10.1007/978-3-540-77058-9_36.

Ummenhofer, C. C. *et al.* (2009) 'What causes southeast Australia's worst droughts?', *Geophysical Research Letters*, 36(4). doi: 10.1029/2008GL036801.

Unganai, L. S. and Kogan, F. N. (1998) 'Drought Monitoring and Corn Yield Estimation in Southern Africa from AVHRR Data', *Remote Sensing of Environment*, 63(3), pp. 219–232. doi: 10.1016/S0034-4257(97)00132-6.

US Department of Commerce, N. (no date) *ESRL Global Monitoring Division - GRAD - Surface Radiation Budget Network (SURFRAD)*. Available at: https://www.esrl.noaa.gov/gmd/grad/surfrad/sitepage.html (Accessed: 27 June 2018).

Verger, A. *et al.* (2012) 'Long term consistent global GEOV1 AVHRR biophysical products', in *Proceedings of the 1st EARSeL Workshop on Temporal Analysis of Satellite Images, Mykonos, Greece*, p. 2833. Available at: https://www.researchgate.net/profile/A_Verger/publication/268204095_LONG_TERM_CONSISTENT_GLOBAL_GEOV1_AVHRR_BIOPHYSICAL_PRODUCTS/links/547474780cf29afed60f7dbd.pdf (Accessed: 28 June 2017).

Vermote, E. *et al.* (2016) 'Preliminary analysis of the performance of the Landsat 8/OLI land surface reflectance product', *Remote Sensing of Environment*, 185, pp. 46–56. doi: 10.1016/j.rse.2016.04.008.

Vermote, E. and Claverie, M. (2013) 'Climate Algorithm Theoretical Basis Document (C-ATBD) AVHRR Land Bundle - Surface Reflectance and Normalized Difference Vegetation Index'. Available at: https://www.ncdc.noaa.gov/sites/default/files/cdr-documentation/CDRP_ATBD_045901B-20b.pdf (Accessed: 20 June 2017).

Vermote, E. F. (2015) 'MOD09A1 MODIS Surface Reflectance 8-Day L3 Global 500m SIN Grid V006'. NASA EOSDIS Land Processes DAAC.

Vermote, E. F., El Saleous, N. Z. and Justice, C. O. (2002) 'Atmospheric correction of MODIS data in the visible to middle infrared: first results', *Remote Sensing of Environment*, 83(1–2), pp. 97–111. doi: 10.1016/S0034-4257(02)00089-5.

Vermote, E. F. and Kotchenova, S. (2008a) 'Atmospheric correction for the monitoring of land surfaces', *Journal of Geophysical Research: Atmospheres*, 113(D23), p. D23S90. doi: 10.1029/2007JD009662.

Vermote, E. F. and Kotchenova, S. (2008b) 'Atmospheric correction for the monitoring of land surfaces', *Journal of Geophysical Research: Atmospheres*, 113(D23), p. D23S90. doi: 10.1029/2007JD009662.

Vermote, E., Justice, C. O. and Breon, F. M. (2009a) 'Towards a Generalized Approach for Correction of the BRDF Effect in MODIS Directional Reflectances', *IEEE Transactions on Geoscience and Remote Sensing*, 47(3), pp. 898–908. doi: 10.1109/TGRS.2008.2005977.

Vermote, E., Justice, C. O. and Breon, F. M. (2009b) 'Towards a Generalized Approach for Correction of the BRDF Effect in MODIS Directional Reflectances', *IEEE Transactions on Geoscience and Remote Sensing*, 47(3), pp. 898–908. doi: 10.1109/TGRS.2008.2005977.

Vermote, E. and Vermeulen, A. (no date) 'ATMOSPHERIC CORRECTION ALGORITHM: SPECTRAL REFLECTANCES (MOD09)'. April 1999.

Villaescusa-Nadal, Franch, B., Vermote, E., *et al.* (2019) 'Improving the AVHRR Long Term Data Record BRDF Correction', *Remote Sensing*, 11(5), p. 502. doi: 10.3390/rs11050502.

Villaescusa-Nadal, Franch, B., Roger, J., *et al.* (2019) 'Spectral Adjustment Model's Analysis and Application to Remote Sensing Data', *IEEE Journal of Selected Topics in Applied Earth Observations and Remote Sensing*, pp. 1–12. doi: 10.1109/JSTARS.2018.2890068.

Villaescusa-Nadal, J. L., Franch, B., Roger, J., *et al.* (2019) 'Spectral Adjustment Model's Analysis and Application to Remote Sensing Data', *IEEE Journal of Selected Topics in Applied Earth Observations and Remote Sensing*, pp. 1–12. doi: 10.1109/JSTARS.2018.2890068.

Wan, Z. (2008) 'New refinements and validation of the MODIS Land-Surface Temperature/Emissivity products', *Remote Sensing of Environment*, 112(1), pp. 59–74. doi: 10.1016/j.rse.2006.06.026.

Wang, S. *et al.* (2017) 'Spatiotemporal patterns of snow cover retrieved from NOAA-AVHRR LTDR: a case study in the Tibetan Plateau, China', *International Journal of Digital Earth*, 10(5), pp. 504–521. doi: 10.1080/17538947.2016.1231229.

Wang, Z. *et al.* (2012) 'Evaluation of Moderate-resolution Imaging Spectroradiometer (MODIS) snow albedo product (MCD43A) over tundra', *Remote Sensing of Environment*, 117, pp. 264–280. doi: 10.1016/j.rse.2011.10.002.

Warren, S. G. (1982) 'Optical properties of snow', *Reviews of Geophysics*, 20(1), pp. 67–89. doi: 10.1029/RG020i001p00067.

Warren, S. G. and Wiscombe, W. J. (1980) 'A Model for the Spectral Albedo of Snow. II: Snow Containing Atmospheric Aerosols', *Journal of the Atmospheric Sciences*, 37(12), pp. 2734–2745. doi: 10.1175/1520-0469(1980)037<2734:AMFTSA>2.0.CO;2.

Wilcox, R. R. (2010) *Fundamentals of Modern Statistical Methods: Substantially Improving Power and Accuracy*. Springer.

Xiong, X. *et al.* (2010) 'On-Orbit Calibration and Performance of Aqua MODIS Reflective Solar Bands', *IEEE Transactions on Geoscience and Remote Sensing*, 48(1), pp. 535–546. doi: 10.1109/TGRS.2009.2024307.

Yang, J. *et al.* (2013a) 'The role of satellite remote sensing in climate change studies', *Nature Climate Change*, 3(10), pp. 875–883. doi: 10.1038/nclimate1908.

Yang, J. *et al.* (2013b) 'The role of satellite remote sensing in climate change studies', *Nature Climate Change*, 3(10), pp. 875–883. doi: 10.1038/nclimate1908.

Zhang, H. K. *et al.* (2018) 'Characterization of Sentinel-2A and Landsat-8 top of atmosphere, surface, and nadir BRDF adjusted reflectance and NDVI differences', *Remote Sensing of Environment*. doi: 10.1016/j.rse.2018.04.031.

Zhang, J. *et al.* (2019) 'Cloud Detection in High-Resolution Remote Sensing Images Using Multi-features of Ground Objects', *Journal of Geovisualization and Spatial Analysis*, 3(2), p. 14. doi: 10.1007/s41651-019-0037-y.

Zhang, X. *et al.* (2010) 'Analysis of Global Land Surface Shortwave Broadband Albedo From Multiple Data Sources', *IEEE Journal of Selected Topics in Applied Earth Observations and Remote Sensing*, 3(3), pp. 296–305. doi: 10.1109/JSTARS.2010.2049342.

Zhu, J. and Shi, J. (2018) 'An Algorithm for Subpixel Snow Mapping: Extraction of a Fractional Snow-Covered Area Based on Ten-Day Composited AVHRR\/2 Data of the Qinghai-Tibet Plateau', *IEEE Geoscience and Remote Sensing Magazine*, 6(3), pp. 86–98. doi: 10.1109/MGRS.2018.2850963.

Zhu, Z. and Woodcock, C. E. (2012) 'Object-based cloud and cloud shadow detection in Landsat imagery', *Remote Sensing of Environment*, 118, pp. 83–94. doi: 10.1016/j.rse.2011.10.028.